We would like to thank the reviewer for their valuable comments that could further improve the quality of the paper. Please find below each reviewer comment in black and our response in red. Revisions made to the manuscript are also highlighted in red.

I. Response to RC1

Some general / overall comments:

1. A basic trajectory model is described, and used to simulate the ctrajectories of both surface and drogued drifters with a geostrophic current field + permutations of ekman, Stokes and windage. The analysis is fairly lengthy, just to conclude with what is well known and should be expected: for the surface drifters, all components should be used, whereas for the drifters with drogue at 2m depth, direct wind drag should not be included. As this is all expected, one can question the relevance of all the different combinations used, e.g. using geostrophic current only. It still has some value to confirm what is known, but it could be made much more compact.

Thank you for this constructive comment. We agree that the original presentation was too lengthy and that some qualitative results were physically expected, particularly the importance of wind-related forcing for the undrogued surface drifters and the reduced direct wind response of the drogued drifters. Following the reviewer's suggestion, we substantially shortened and reorganized this part of the manuscript. Specifically, we combined the original Sections 3.5 ("Evaluation of particle trajectories") and 4.1 ("Optimal forcing combinations and ocean models") into a more compact Section 3.5, now titled "Data-driven optimal forcing combinations."

2. What is more of a question, is the calculation of the windage (wind drift factor) which is a critical component. This is calculated as 1.5% and 0.5% for surface and drogued drifters respectively, but without much details of the exact computation. In any case, this important coefficient will be associated with uncertainty, and it might be more relevant to vary (or even tune) this coefficient, than some of the above mentioned variants which are expected to be not good.

Thank you for this important comment. We agree that the original manuscript did not explain the windage coefficient clearly enough. In this study, the windage coefficient, r, was estimated from a first-order balance between aerodynamic drag on the exposed part of the drifter and hydrodynamic drag on the submerged part:

$$r = \left(\frac{\rho_a C_{d,a} A_a}{\rho_w C_{d,w} A_w}\right)^{1/2},$$

where ρ_a and ρ_w are the densities of air and seawater, $C_{d,a}$ and $C_{d,w}$ are the drag coefficients in air and water, and A_a and A_w are the projected areas above and below the sea surface, respectively. Because $C_{d,a}$ and $C_{d,w}$ were not measured directly for our custom drifters, we used $C_{d,a}/C_{d,w} \approx 1$ as a first-order approximation, consistent with previous studies (de Dominicis et al., 2016; van der Mheen et al., 2020).

This assumption ($C_{d,a}/C_{d,w} \approx 1$) is appropriate for the DX drifters because the exposed and submerged parts are both cylindrical, so the air-side and water-side drag coefficients are expected to be of comparable order. The cylindrical body has a diameter of 0.09 m and a height of 0.30 m, with approximately 0.03–0.05 m protruding above the water surface. Therefore, the projected area exposed to air is $A_a \approx 0.09 \times (0.03\text{–}0.05) = 0.0027\text{–}0.0045\ \mathrm{m}^2$, whereas the submerged projected area is $A_w \approx 0.09 \times (0.25\text{–}0.27) = 0.0225\text{–}0.0243\ \mathrm{m}^2$. Using $\rho_a/\rho_w \approx 1.2 \times 10^{-3}$ and $C_{d,a}/C_{d,w} \approx 1$, the estimated windage coefficient is $r_{DX} \approx 0.012\text{–}0.016$. Accordingly, $r = 0.015$ was adopted for the DX drifters.

For the DO drifters, the submerged flat drogue plate likely has a larger drag coefficient than the cylindrical float; therefore, assuming $C_{d,a}/C_{d,w} \approx 1$ gives a conservative upper-bound estimate of windage rather than an exact calibrated value. For the drogued DO drifters, the exposed area above the sea surface is similar to that of the DX drifters, but the submerged drag area is much larger because of the drogue positioned near 2 m depth. To avoid double-counting the two perpendicular plates, we used one effective projected drogue plate area: $A_{w,\mathrm{drogue}} = 0.30 \times 0.30 = 0.09\ \mathrm{m}^2$. The submerged cylindrical body contributes $A_{w,\mathrm{body}} \approx 0.09 \times 0.26 = 0.0234\ \mathrm{m}^2$. Thus, the total effective submerged projected area is approximately $A_w \approx 0.0234 + 0.09 = 0.1134\ \mathrm{m}^2$. Using $C_{d,a}/C_{d,w} \approx 1$, this gives $r_{DO} \approx 0.0053\text{–}0.0069$. The adopted value $r = 0.005$ is therefore a conservative geometry-based estimate for the DO drifters.

We also considered published drag-coefficient values for drifter drag-area calculations. McCaffrey and Koeberle (2024) used $C_D = 0.74$ for cylindrical float elements and $C_D = 1.98$ for flat-plate drogue elements. Applying these values to the DO geometry gives $r_{DO} = \left[\rho_a(0.74A_a)/\rho_w\left(0.74A_{w,\mathrm{body}} + 1.98A_{w,\mathrm{drogue}}\right)\right]^{1/2}$, which yields $r_{DO} \approx 0.0035\text{–}0.0045$. This value is slightly lower than, but close to, the adopted $r = 0.005$. Therefore, $r = 0.005$ does not underestimate the direct wind effect on the DO drifters; rather, it is a physically reasonable and slightly conservative estimate. We have added the discussion about r coefficient in Lines 148-176.

We agree that the windage coefficient is associated with uncertainty. However, we did not tune r to minimize trajectory error, because doing so would mix two different objectives: estimating a drifter-specific windage coefficient and evaluating the relative contributions of geostrophic current, Ekman current, Stokes drift, and windage. Instead, we used *a priori* geometry-based values of r and kept them fixed across the forcing-combination experiments. In response to the reviewer's comment, we added a sensitivity test for the undrogued DX drifter, which is more directly exposed to wind forcing. The geometry-based windage coefficient used for DX in the manuscript was $r = 0.015$. To examine the sensitivity of the results to this parameter, we repeated the DX simulations using a smaller value, $r = 0.005$, representing an underestimated windage effect, and a larger value, $r = 0.030$, representing an overestimated windage effect. The sensitivity test showed that the optimal forcing combination changed when r was substantially modified. For $r = 0.005$, the lowest average MAE was obtained for C8, $u_g + u_e + u_s + u_w$, with $\overline{\text{MAE}} = 117.3$ km. For the geometry-based value, $r = 0.015$, the lowest average MAE was obtained for C7, $u_g + u_s + u_w$, with $\overline{\text{MAE}} = 42.9$ km. For $r = 0.030$, the lowest average MAE was obtained for C4, $u_g + u_w$, with $\overline{\text{MAE}} = 88.2$ km. Although different values of r produced different optimal forcing combinations, the geometry-based value $r = 0.015$ produced the smallest overall error among the tested cases. Specifically, the optimal MAE values for $r = 0.005$ and $r = 0.030$ were 117.3 km and 88.2 km, respectively, both of which were larger than the optimal MAE of 42.9 km obtained using $r = 0.015$. These results indicate that model performance is sensitive to the windage coefficient, but they also support the use of the geometry-based value $r = 0.015$ for the DX drifter. We therefore used the geometry-based coefficient as the primary estimate and used the additional simulations only to evaluate sensitivity, rather than tuning r freely to obtain the best trajectory fit. This clarification and the sensitivity-test results have been added to the revised manuscript in Lines 473-479.

Table R1. MAE values for PTM-DX sensitivity test using $r = 0.005$. The maximum MAE value for each day is shown in bold.

Day	C1	C2	C3	C4	C5	C6	C7	C8
5	130.2	128.2	123.1	129.8	106.3	117.1	90.0	**29.2**
10	252.4	243.2	223.7	237.2	207.1	220.9	166.0	**138.2**
30	473.4	449.3	300.2	423.5	260.2	348.0	209.0	**161.1**
75	550.2	541.3	290.9	459.2	219.8	369.3	145.0	**140.7**
Avg.	351.6	340.5	234.5	249.9	198.4	211.1	122.0	**117.3**

Table R2. MAE values for PTM-DX sensitivity test using the geometry-based value $r = 0.015$. The maximum MAE value for each day is shown in bold.

Day	C1	C2	C3	C4	C5	C6	C7	C8
5	130.2	128.2	123.1	89.0	106.3	60.9	25.3	**20.4**
10	252.4	243.2	223.7	162.3	207.1	104.5	**29.5**	43.9
30	473.4	449.3	300.2	216.4	260.2	104.6	**55.6**	114.0
75	550.2	541.3	290.9	164.6	219.8	98.3	**61.2**	105.4
Avg.	351.6	340.5	234.5	158.1	198.4	92.1	**42.9**	70.9

Table R3. MAE values for PTM-DX sensitivity test using $r = 0.030$. The maximum MAE value for each day is shown in bold.

Day	C1	C2	C3	C4	C5	C6	C7	C8
5	130.2	128.2	123.1	**25.6**	106.3	31.8	48.4	58.6
10	252.4	243.2	223.7	**69.8**	207.1	87.2	117.7	109.7
30	473.4	449.3	300.2	**131.9**	260.2	165.9	207.7	198.8
75	550.2	541.3	290.9	**125.5**	219.8	173.7	207.7	198.8

Day	C1	C2	C3	C4	C5	C6	C7	C8
Avg.	351.6	340.5	234.5	**88.2**	198.4	91.7	116.3	113.2

3. The Stokes drift is calculated directly from a wave model, and apparently given by Eq 1, but this equation is missing the left side, presumably being the Stokes drift itself. Despite only about 10% of the drifter sticking out of water (~3 of 30 cm), Stokes drift is evaluated at z=0 (surface) and 1.5m ("weighted mean" of surface and drogue at 2m). For the undrogued drifter, a depth of ~15 cm should be more relevant. Difference might not be huge, but (along with uncertain/postulated wind drift factor) might be enough to give wrong conclusions about the optimal configuration, e.g. to support the claim/finding that the above model is better than using CMEMS and HYCOM models.

Thank you for this comment. We agree that Eq. (1) was incomplete in the original manuscript. We have corrected the equation by adding the missing left-hand side and explicitly defining it as the Stokes drift velocity.

We also agree that the depth at which Stokes drift is applied should be consistent with the submerged geometry of each drifter type. In the original manuscript, the DX simulation was described as using surface forcing at z=0 m. However, the Stokes drift used in the actual calculation was taken from the shallowest subsurface level of the wave-model output, z=−0.1 m (Line 223), rather than exactly at the air–sea interface. The DX drifter is 0.30 m high, with only about 0.03–0.05 m protruding above the water surface. Therefore, most of the drifter body is submerged within the upper 0.25–0.27 m of the water column, giving an effective submerged center of approximately 0.12–0.14 m below the surface. Thus, the use of z=−0.1 m provides a physically representative estimate of the Stokes drift acting on the DX drifter and is close to the reviewer's suggested depth of approximately 0.15 m.

4. The end of the paper performs simulations also with "CMEMS and HYCOM" models, as an alternative to the above "data driven" approach (according to title). However, this "CMEMS model" is the GLORYS reanalysis, and "HYCOM" is here the GOFS analysis. These more descriptive names should be given in the manuscript, and also show that these "models" are in fact analyses which should also be based on geostrophic currents and Ekman currents, just as the "data" that is here used as an alternative to the "models". In other words, the distinction between "data" and "model" is unclear and partly un-real. The discussion would then be why the "analysis" constructed in this paper (geostrophic+ekman+stokes+wind) is better than these other analyses. It should also be noted that the used geostrophic current has hourly time step, whereas the GLORYS CMEMS has only daily data (as far as I can tell) - which can also partly explain the poorer performance.

Thank you for this helpful comment. We agree that the terms "data-driven" and "model" were not sufficiently clear in the original manuscript. We have revised the manuscript to avoid this ambiguity. Specifically, the simulation previously referred to as "CMEMS" is now described as the GLORYS12V1 global ocean reanalysis distributed by Copernicus Marine, and the simulation previously referred to as "HYCOM" is now described as the GOFS analysis based on HYCOM and NCODA. GLORYS12V1 is a global eddy-resolving ocean reanalysis product, while GOFS/HYCOM is an operational analysis/forecast system based on HYCOM with data assimilation. Therefore, we replaced the general expression "global ocean models" with more accurate terms such as "ocean analysis/reanalysis products" and "model-derived velocity products" throughout the revised manuscript.

We also agree that the distinction between our "data-driven" approach and these analysis/reanalysis products should be stated more carefully. GLORYS and GOFS/HYCOM are not free-running models; they assimilate observations and provide dynamically consistent ocean circulation fields. Therefore, the revised manuscript no longer presents the comparison as a simple contrast between "data" and "models." Instead, we describe our approach as an observation-constrained surface-forcing reconstruction, in which geostrophic current, Ekman current, Stokes drift, and windage are explicitly combined and evaluated against observed drifter trajectories.

The reason why the reconstructed forcing combination can outperform GLORYS and GOFS/HYCOM in this specific case is not that GLORYS and GOFS/HYCOM lack observational information. Rather, the difference arises because the reanalysis/analysis velocity fields are dynamically adjusted by the model physics, data-assimilation procedure, vertical mixing, spatial resolution, and temporal averaging. Even when sea-surface height is assimilated, the resulting near-surface velocity gradients and finite-time Lagrangian transport structures can differ from those obtained from the explicitly reconstructed forcing field. We therefore added a direct FTLE-based comparison of the data-driven velocity combinations and the GLORYS/GOFS velocity products. This comparison shows that the data-driven fields better reproduce the hyperbolic-type Lagrangian structure associated with the early drifter bifurcation, whereas the corresponding FTLE ridges in GLORYS and GOFS/HYCOM are weaker, displaced, or less coherent in the bifurcation region (Lines ??).

We also clarified the temporal resolution of the products. The GLORYS12V1 reanalysis used for PTM-CMS provides daily fields, whereas the data-driven reconstruction includes wind-related components derived from hourly ERA5 wind forcing. Thus, differences in temporal resolution and in the representation of high-frequency near-surface wind-driven transport may partly contribute to the lower trajectory skill of the GLORYS-based simulation (Lines 517-520).

5. To evaluate the performance of the various simulations, mean absolute separation and a skill score is used. However, these are apparently calculated only as a single number from the beginning of each the trajectory, albeit also given at some discrete "time steps" (rather "end times"). As a bifurcation point is seen very early (apparently better in geostrophic current field than in "models", the simulated and observed drifters will quickly be far apart. And when these are separated, continued calculation of skillscore (or MAE) is less relevant, as you are comparing a drifter in one place, to a drift calculation using currents from a very different place

- i.e. data becomes uncorrelated. Much more robust to evaluate the optimal forcing, would be to chunk the trajectories in segments of a couple of days. For this reason - and especially due to the early bifurcation “incident” - and also considering the above points about windage and Stokes drift - the conclusion that given “data-driven analysis” is better than the “models” becomes questionable.

Thank you for this important comment. We agree that cumulative trajectory metrics such as MAE and skill score should be interpreted with caution when an early bifurcation occurs. Once the observed and simulated drifters enter different dynamical branches, the subsequent separation may partly reflect pathway divergence rather than only local velocity error. Therefore, we agree that a segment-based evaluation provides a more robust diagnostic of short-term trajectory skill.

Following the reviewer’s suggestion, we performed an additional segment-based MAE analysis for the DX drifters. The observed and simulated trajectories were divided into 3-day segments, and the MAE was calculated independently for each segment. This test was added as a sensitivity analysis to reduce the dominance of accumulated downstream errors after the early bifurcation.

The new results are summarized in Table R4. The segment-based MAE confirms that the simulations including geostrophic current, Stokes drift, windage, and Ekman current performed best overall. The GSWE case produced the lowest average segment-based MAE, 28.7 km, and also the smallest standard deviation, 3.7 km. The GSW case was the second-best case, with an average MAE of 31.3 km and a standard deviation of 8.3 km. In contrast, the G-only and GE cases showed much larger average MAE values, 53.5 km and 51.9 km, respectively. The improvement is especially clear during the first 0–3 day segment, when the early bifurcation occurs: the MAE decreased from 120.0 km for G and 113.1 km for GE to 46.4 km for GSW and 33.6 km for GSWE. This indicates that the improved performance is not only a result of long-term accumulated separation, but is already evident during the early bifurcation period.

This additional analysis slightly refines our original interpretation. In the cumulative MAE analysis, GSW showed the best DX performance, whereas the segment-based MAE analysis identifies GSWE as the best and most stable case. This difference indicates that the two metrics emphasize different aspects of trajectory prediction: cumulative MAE evaluates the integrated pathway prediction, including whether the simulation follows the correct transport branch after bifurcation, whereas segment-based MAE evaluates short-term local trajectory skill.

We have therefore revised the manuscript to clarify that the cumulative metrics are not interpreted as purely local velocity-error measures. We also softened the conclusion by describing the comparison with model-derived velocity products as a benchmark comparison rather than an absolute demonstration that the data-driven analysis is always superior. The revised interpretation is that the data-driven forcing combinations, particularly GSW and GSWE, better reproduce the early bifurcation and short-term DX trajectory evolution, while the cumulative metrics remain useful for evaluating the integrated transport pathway.

This discussion has been added in Lines 487-495.

Table R4. Segment-based mean absolute error (MAE) for the DX drifter simulations. The observed and simulated DX trajectories were divided into 3-day segments, and the MAE was calculated independently for each segment to evaluate short-term local trajectory skill. G, E, S, and W denote geostrophic current, Ekman current, Stokes drift, and windage, respectively. AVG and STD indicate the mean and standard deviation of the segment-based MAE across the listed time intervals. Lower MAE values indicate better agreement between the simulated particles and observed DX drifters.

duration(day)	0-3	3-6	6-9	27-30	72-75	AVG	STD
G	120.0	37.0	31.5	41.8	37.4	53.5	33.4
GE	113.1	38.1	29.9	37.1	41.3	51.9	30.8
GS	103.0	32.2	30.6	27.5	27.3	44.1	29.5
GW	83.4	27.4	31.6	31.9	53.4	45.5	21.0
GSE	91.6	33.1	29.4	25.8	28.9	41.8	25.0
GEW	67.6	27.9	30.1	28.6	57.2	42.3	16.8
GSW	46.4	22.4	33.3	27.4	27.1	31.3	8.3
GSWE	33.6	23.7	31.9	25.4	29.0	**28.7**	**3.7**

6. When using CMEMS and HYCOM models, the Stokes drift is varied as 1.5 and 3.0% Why not use the same variations as for the "data-driven" approach with geostrophic current?

Thank you for pointing this out. We apologize for the confusion caused by the wording in the original manuscript. The values of 1.5% and 3.0% refer to windage coefficients, not to variations of Stokes drift.

7. Mean current and wind fields are shown in both Figure 1 and Figure 2, apparently redundant. Figure 2 shows average wind and current for November along with surface drifters and December along with drogued drifters. This is confusing, as both sets of drifters were active the whole/same period. Also the value of showing monthly average to support discussion of specific events such as a bifurcation point and sudden wind change is questionable.

Thank you for this constructive comment. We agree that the original presentation of the mean current and wind fields was partly redundant and potentially confusing. In the revised manuscript, we reorganized Figures 1 and 2 to separate their purposes more clearly. Figure 1 now focuses on the deployment region and the environmental conditions during the initial release and early bifurcation period, using one-week-averaged geostrophic current, wind, SST, and SSH fields after drifter release. Figure 2 was revised to focus only on the observed drifter trajectories and the Lagrangian structure associated with the early bifurcation, without repeating monthly mean current and wind fields.

Some specific comments:

1. Line 48: Unclear sentence: "Stokes drift influences the direction and speed of surface currents". Stokes drift is a lagrangian current adding to the Eulerian current, not to be confused with Coriolis-Stokes which can modify the Eulerian current.

Thank you for your comment. The sentence has been revised to 'The wave-induced current known as Stokes drift adds to the Eulerian surface current, thereby contributing to the transport of floating objects' (Line 52).

2. Line 90: Drogued drifters are throughout paper referred to as "DO" and undrogued as "DX". However, the naming logic is not clear, and thus the reader can easily forget which is which. More descriptive terms should be used, or instead the user should be reminded regularly (e.g. in figure texts) which is which.

Thank you for your constructive comment. We agree and have clarified the terminology. We now consistently refer to them as undrouged (DX) and 'drogued (DO)' throught the manuscript.

3. Line 137: What exactly is the SST used for?

Thank you for your question. The SST was not used as an input forcing in the particle tracking model. It was only used as a background field in Figure. 1 to describe the surface thermal structure near the deployment region. In particular, the SST helps show the location of thermal fronts around the EKWC, which are useful for interpreting the local current structure and the early drifter bifurcation.

4. Line 145: diffusion term is added - but is this used for the simulation with just a single "particle" per trajectory? If so, the random numbers will degrade the simulation, which is then not deterministic. Diffusion (or random numbers in general) only makes sense when using many particles.

Thank you for this important comment. We agree that using a stochastic diffusion term with only one numerical particle per drifter initial location can make the trajectory comparison sensitive to a single random realization. In the main simulations, one numerical particle was released from each observed drifter initial position so that the simulated particle set corresponded directly to the observed drifter set. However, because the random-walk diffusion term includes Gaussian random numbers, the exact trajectory and MAE values may be affected by stochastic variability.

To examine whether this stochastic variability influenced the main conclusions, we performed an additional ensemble-sensitivity test using 10 numerical particles for each drifter initial location. In this test, the deterministic velocity fields were kept identical to those used in the original simulations, while only the Gaussian random sequences in the diffusion term were varied. The trajectory error was then recalculated using the ensemble-mean MAE.

The comparison between the original single-particle results and the 10-particle ensemble-sensitivity results showed that the absolute MAE values changed slightly, but the main optimal forcing combinations did not change. For PTM-DX, C8 produced the lowest MAE at the early time of 5 days, whereas C7 produced the lowest MAE at later times and also had the lowest average MAE. Thus, except for the very early stage, C7 remained the optimal forcing combination for DX. For PTM-DO, C8 consistently produced the lowest MAE in both the original single-particle simulation and the 10-particle ensemble-sensitivity test.

These results indicate that the stochastic diffusion term affects the exact MAE values but does not control the main conclusion regarding the optimal forcing combinations. We have clarified this point in the revised manuscript by adding the ensemble-sensitivity test in Section 3.5 (Lines 508-515).

Table R5. Original MAE table using one numerical particle per drifter initial location.

	Day	C1	C2	C3	C4	C5	C6	C7	C8
PTM-DX	5	134.5	107.3	122.7	90	106.1	57	22	**19.3**
	10	251.4	242.6	221.1	166	209.6	92.6	**24.1**	35.8
	30	475.8	460.7	308.6	209	265.6	92	**54**	91
	75	562.5	606.1	347	145	243.9	90.8	**73.8**	83.2
PTM-DO	5	75.7	64.1	79.3	68.7	68.8	59.2	68.7	**55.3**
	10	146.5	135.6	140.2	123.1	129.4	113.8	120.1	**107**
	30	318	286.5	304.9	235.6	216.9	175.5	201.4	**110.7**
	75	537	487.9	487.9	377.1	459.6	322.6	410.3	**185.2**

Table R6. Revised MAE table using a 10-particle ensemble and ensemble-mean MAE.

	Day	C1	C2	C3	C4	C5	C6	C7	C8
PTM-DX	5	130.2	128.2	123.1	89	106.3	60.9	25.3	**20.4**
	10	252.4	243.2	223.7	162.3	207.1	104.5	**29.5**	43.9
	30	473.4	449.3	300.2	216.4	260.2	104.6	**55.6**	114
	75	550.2	541.3	290.9	164.6	219.8	98.3	**61.2**	105.4
PTM-DO	5	70.5	64.8	77.4	67	67.5	57.8	67.5	**53**
	10	142.9	133.5	143.1	125.7	129.4	114.3	120.1	**106**
	30	315.6	273.7	296.2	276	211	166.6	194.9	**117.7**
	75	528.1	488.7	477	472.9	359.2	285	330.9	**182.6**

5. Line 147: “each step ormal distribution”

Thank you for pointing this out. We have corrected it.

6. Line 148-150: Windage is here said to be part of “total current velocity” - this should probably instead be “total drift velocity”.

Thank you for pointing this out. We have corrected it.

7. Line 153-158: Some more details about calculation of r would be welcome, e.g. what values are used for Cd,a and Cd,w.

Please see the answer to Q2.

8. Line 162: Reference to Table 1 - but both this and Table 2 are missing!

Thank you for pointing this out. We apologize for the missing information about Tables 1 and 2.

9. Line 174: the distance of a degree of longitude is different from a degree of latitude. Thus, the given MAE will "punish" longitudinal errors more than the same latitudinal errors.
Thank you for this comment. We agree that one degree of longitude and one degree of latitude do not correspond to the same physical distance. Although the MAE equation is written in terms of longitude and latitude differences, the calculation was not performed directly in angular units. Before computing the MAE, both ΔLon and ΔLat were converted to physical distances in kilometers, accounting for the latitude-dependent length of a degree of longitude. The MAE therefore represents the trajectory separation in physical distance space and is not biased by the different spatial scales of longitude and latitude. We have clarified this (Lines 240-241).

10. Line 195: Please explain what is the "radially symmetrical variance"

Thank you for pointing this out. The term "radially symmetrical variance" was unclear, and we have revised the manuscript to define it more explicitly. Following Okubo (1971) and LaCasce (2008), σ_r^2 represents the horizontal radial variance of a particle or drifter distribution, defined as the mean squared distance of particles from the center of mass of the distribution. In other words, an irregular particle cloud is represented by an equivalent radially symmetric spreading measure, and σ_r^2 quantifies the radial spread of that cloud. It was used to estimate the horizontal dispersion coefficient from the temporal growth rate of the particle-cloud variance (Lines 261-264).

11. Line 202: For FSLE-figures below, I assume L/delta equals delta_0, but what is the value of delta_f ?

Thank you for pointing this out. We agree that the definition of the final separation distance was not sufficiently clear. In the FSLE calculation, δ_0 denotes the initial separation scale, and δ_f is the threshold separation distance used to define the growth time. In this study, δ_f was not prescribed as a fixed absolute distance; instead, it was defined relative to each initial separation scale as $\delta_f = 2\delta_0$. Thus, the FSLE was calculated as $\lambda(\delta_0) = \ln(2)/\langle\tau(\delta_0, 2\delta_0)\rangle$, where $\tau(\delta_0, 2\delta_0)$ is the time required for a particle pair separation to grow from δ_0 to $2\delta_0$. We have revised the manuscript to explicitly state this definition and to avoid ambiguity in the FSLE formulation (Lines 269-273).

12. Line 208: Heading "Results, or a descriptive heading about the results"

Thank you for your comment. We changed the section heading to "3. Results".

Section 3.1: The bifurcation is discussed, but as mentioned above, it is not easy to assess this without seeing the actual currents (including CMEMS and HYCOM) zoomed at the time and location of the passing of this point.

Thank you for this insightful comment. We agree that, because GLORYS and GOFS/HYCOM assimilate satellite altimetry, their sea-surface-height fields may contain information similar to that used to derive the altimetric geostrophic velocity. However, assimilation of sea-surface height does not necessarily ensure that the resulting near-surface velocity gradients, finite-time transport barriers, and hyperbolic-type Lagrangian structures are reproduced in the same way.

To examine this point, we added a direct comparison of FTLE structures computed from the data-driven velocity fields and the model-derived velocity products (Figure 10). In the data-driven cases, particularly for G, GES, and GESW (Figure 10a1–a3), the FTLE fields show a clear hyperbolic-type structure near the region where the observed drifters bifurcated. The attracting and repelling FTLE ridges form a coherent transport-separating structure, consistent with the observed early separation of the drifter pathways.

In contrast, the corresponding FTLE structures obtained from CMS/GLORYS and HYC/GOFS are weaker, displaced, or less coherent in the bifurcation region (Figure 10b1–c3). Adding windage and Stokes drift to the model-derived velocities modifies the FTLE ridge patterns, but it does not fully recover the same transport-separating structure shown by the data-driven velocity fields. This indicates that the poorer performance of the model-derived simulations is related not only to differences in velocity magnitude, but also to differences in the finite-time Lagrangian structure controlling the early trajectory separation.

Therefore, although GLORYS and GOFS/HYCOM assimilate sea-surface height, the model-derived surface velocities do not necessarily reproduce the same geostrophic velocity gradients and hyperbolic-type transport structure as the altimetry-derived geostrophic product. We have clarified this point in the revised manuscript and added Figure 10 to support the interpretation (Lines 565-591).

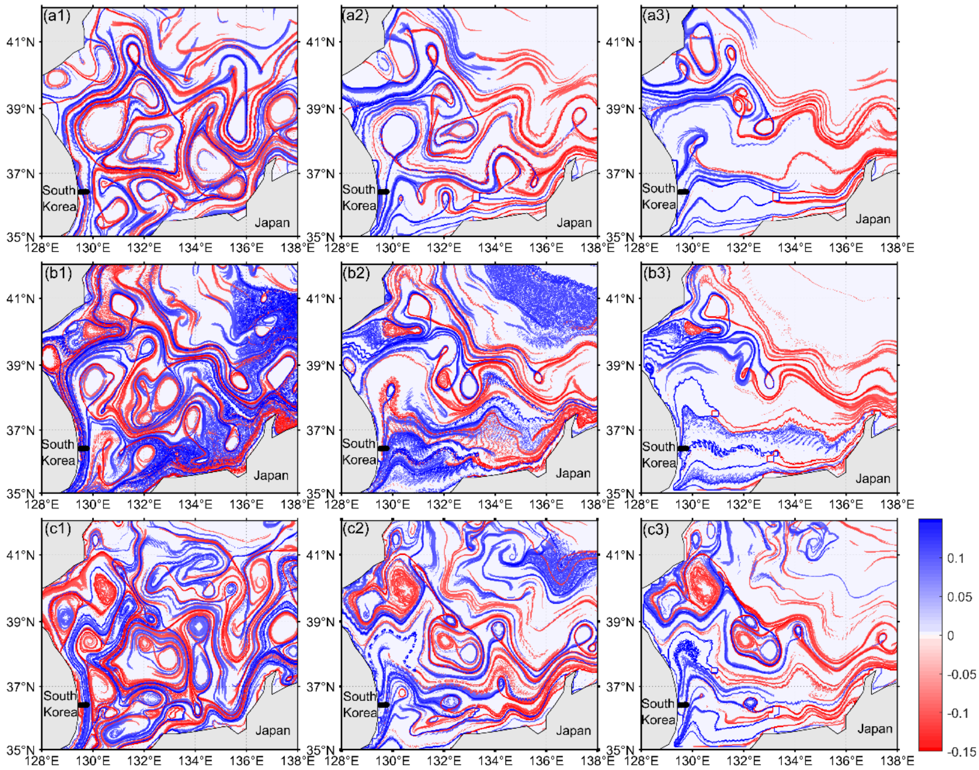

Figure 10. Finite-time Lyapunov exponent (FTLE) structures computed from one-week-averaged velocity fields. The panels show FTLE fields for (**a1**) u_g, (**a2**) $u_g + u_e + u_s$, (**a3**) $u_g + u_e + u_s + u_w$, (**b1**) CMS, (**b2**) CMS-w1, (**b3**) CMS-w1-st, (**c1**) HYC, (**c2**) HYC-w1, and (**c3**) HYC-w1-st. Here, u_g, u_e, u_s, and u_w denote geostrophic current, Ekman current, Stokes drift, and windage, respectively. CMS denotes the GLORYS reanalysis distributed by Copernicus Marine, and HYC denotes the GOFS analysis based on HYCOM.

13. Line 224: current are white vectors, not black.

Thank you for your comment. We have corrected the Figure 2.

14. Line 318: A model grid resolution of 25 km is mentioned. Which model does this refer to? The geostrophic current used has a grid spacing of 0.125 degrees.

Thank you for pointing this out. The "25 km grid resolution" mentioned in the manuscript refers to the nominal grid spacing of the gridded geostrophic velocity field used in the PTM calculations, not to the effective physical resolution of the altimetry product. At the time the trajectory calculations were performed, the geostrophic velocity field used in the PTM was on a 0.25° grid, which corresponds to approximately 25 km in the East/Japan Sea. We agree that this wording was unclear, particularly because the current Copernicus Marine SEALEVEL_GLO_PHY_L4_MY_008_047 product is now distributed on a 0.125° grid. We have therefore revised the manuscript to distinguish the nominal grid spacing used in the PTM calculations from the current product grid description (Lines 141-143, Lines 418-419, Lines 425-429).

15. 'Figure 11 text: "The raletive"

Thank you for pointing this out. We have corrected the typo.

References

de Dominicis, M., Bruciaferri, D., Gerin, R., Pinardi, N., Poulain, P.-M., Garreau, P., Zodiatis, G., Perivoliotis, L., Fazioli, L., Sorgente, R., and Manganiello, C.: A multi-model assessment of the impact of currents, waves and wind in modelling surface drifters and oil spill, Deep Sea Research Part II, 133, 21–38, 2016.

van der Mheen, M., Pattiaratchi, C., Cosoli, S., and Wandres, M.: Depth-dependent correction for wind-driven drift current in particle tracking applications, Frontiers in Marine Science, 7, 305, 2020.

McCaffrey, L. and Koeberle, A. L.: An economical open-source Lagrangian drifter design to measure deep currents in lakes, Water Resources Research, 60, e2024WR037429, 2024.

II. Response to RC2

The manuscript investigates the role played by various data derived surface forcings in a Particle Tracking Model (PTM). The results are potentially interesting, but the paper needs major revision before publication. The main issues are indicated below, followed by more specific points.

Main Issues

1. The paper deals with a specific PTM, aimed at reproducing particles moving at the ocean surface and at 2 m depth. While this is a perfectly valid approach, I think the authors should clarify that this is not directly applicable to the transport of macro or micro plastic. Indeed, specific terms should be added to the PTM to simulate the behaviour of plastic debris, depending on their size and characteristics. Such processes include fragmentation, buoyancy changes due to colonization, aggregation and several others. The authors should explain this point up front in the Introduction and Conclusions, i.e. that they focus only on the fluid dynamical part of plastic transport, while for actual applications a number of other processes should included.

Thank you for this important comment. We agree that the scope of the PTM should be clearly distinguished from a complete macroplastic or microplastic fate model. In the revised manuscript, we have clarified this point in the Introduction, Methods, and Conclusions. Specifically, we now state in the Introduction that "floating debris transport" in this study refers to the fluid-dynamical transport component represented by passive particles moving near the ocean surface, rather than the complete fate of specific macroplastic or microplastic particles. We also explicitly state that particle-specific processes such as fragmentation, biofouling-induced buoyancy change, aggregation, settling, and resuspension were not included in the present framework (Lines 78-81, Lines 85-89, Lines 717-723).

2. I am worried about the drifters used in the experiment. No details on drifter testing is provided in Section 2.1, and it is well known that drifters with different properties can move very differently, especially in the very upper part of the ocean. In particular, windage and Stokes drift can be very sensitive to the surface expression. It is important that the authors provide information on the fluid dynamical properties of drifter motion, either using lab experiments or at least quantitatively comparing their motion with that of other drifters with tested properties (such as for instance CODE or CARTHE for the 2m case).

Thank you for this important comment. We agree that the fluid-dynamical properties of the drifters should be described more clearly, because near-surface drifter motion can be sensitive to drifter geometry, surface expression, windage, and Stokes drift. We have therefore revised Section 2.1 and the related Methods sections to provide a more quantitative description of the drifter geometry, effective sampling depth, and windage coefficients. We did not perform laboratory calibration experiments for these custom-made drifters, and we now state this limitation explicitly in the manuscript. Instead, we added a quantitative geometry-based comparison with tested near-surface drifter designs, including previous conventional design including CODE and CARTHE drifters.

DX drifter was 0.30 m high and 0.09 m in diameter, with 0.03–0.05 m protruding above the sea surface, and the DO drifter additionally included two 0.30 × 0.30 m perpendicular drogue plates positioned near 2 m depth. the effective sampling depth for the DO drifter was estimated from the area-weighted hydrodynamic centroid of the submerged cylindrical body and the drogue. The submerged cylindrical body has a projected area of approximately $0.09 \times 0.26 = 0.0234\ \mathrm{m}^2$, with its centroid near 0.13 m depth, whereas one effective 0.30×0.30 m drogue plate has a projected area of $0.09\ \mathrm{m}^2$, centered near 2 m depth. Therefore, $z_c = [(0.0234)(0.13) + (0.09)(2.0)]/(0.0234 + 0.09) \approx 1.6$ m. Thus, the adopted effective depth of $z = -1.5$ m for the DO Stokes drift and Ekman current provides a reasonable representation of the combined hydrodynamic response of the surface float and submerged drogue.

The CARTHE drifter follows currents in the upper 0.60 m of the water column, with a representative drogue depth of approximately 0.40 m and wind-induced slip less than 0.5% of the 10 m wind speed (Novelli et al., 2017; Poulain et al., 2022). The CARTHE drogue dimension of 0.38 × 0.38 m was taken from the drifter drag-area comparison reported by McCaffrey and Koeberle (2024). The CODE drifter is a standard upper-ocean surface drifter designed to measure currents in the upper meter of the water column using four drag-producing sails attached to a vertical body (Davis, 1985; Poulain et al., 2022). The effective depth of the CODE drifter was set to approximately 0.5 m, and its mean downwind slip has been reported to be about 0.1% of the wind speed (Poulain and Gerin, 2019). We have added this in Lines 104-113.

Table R1. Comparison of the custom DX/DO drifters with tested near-surface drifter designs.

Drifter type	Shape	Dimensions	Effective depth	Windage coefficient
DX, this study	Cylinder	0.30 m high; 0.09 m diameter	~0.135 m	0.015
DO, this study	Cylinder + drogue plate	DX body + two 0.30 × 0.30 m plates near 2 m depth	~1.6 m	0.005
CARTHE	Toroid + drogue plate	0.38 × 0.38 m drogue	~0.4 m	< 0.005
CODE	Sails	1 m-long tube; sail top ~0.30 m below surface	~0.5 m	~0.001

3. The explanation of the datasets and schemes used in the analysis (Section 2.2-2.3) is incomplete and not very clear.

Please explain further the characteristic of the SEALEVEL product, in particular from which satellite observations is obtained and what is the expected physical resolution (aside from the nominal one).

The Ekman layer depth does not seem to have the correct units

The discussion on how windage is computed should be introduced for consistency in Section 2.2 (before eq 5). How are the two r parameter values used in the paper (0.01.5, 0.005) obtained? The authors mention a quite extensive range from the literature; how did they select the two values and did they do some sensitivity tests?

How is the Smagorinsky diffusion coefficient computed? from the geostrophic velocity?

Thank you for these helpful comments. We agree that the original explanations of the datasets and numerical schemes in Sections 2.2 and 2.3 were incomplete. We have revised these sections to provide clearer descriptions of the SEALEVEL product, Ekman layer depth, windage parameterization, and Smagorinsky diffusion coefficient.

(1) SEALEVEL product

We have added more details on the SEALEVEL product in Section 2.2. The geostrophic current used in this study was derived from the Copernicus Marine SEALEVEL Level-4 altimeter product processed by the CNES/CLS DUACS multimission altimeter data processing system. This product is based on merged satellite altimeter observations and provides sea level anomaly, absolute dynamic topography, and derived geostrophic currents. We now explicitly state that the product combines observations from multiple satellite altimeter missions, including Sentinel-6A, Sentinel-3A/B, Jason-3, SARAL/AltiKa, CryoSat-2, OSTM/Jason-2, Jason-1, TOPEX/Poseidon, Envisat, GFO, ERS-1/2, and Haiyang-2A/B. The current Copernicus Marine SEALEVEL global Level-4 product is distributed on a nominal grid of 0.125° × 0.125° with daily temporal resolution, whereas the product version used at the time of our processing had a nominal grid of 0.25° × 0.25°. We also clarified that the nominal grid spacing should not be interpreted as the true physical resolution of the mapped altimetry field. Following the Copernicus Marine quality documentation, the effective resolution of the global Level-4 DUACS product is of mesoscale order, approximately 180 km and 33 days at mid-latitudes.

(2) Ekman layer depth

We thank the reviewer for pointing out the dimensional inconsistency. The Ekman layer depth formulation was adopted from Rypina et al. (2021), but the units of the empirical coefficient were not stated clearly in the original manuscript. The Ekman layer depth $d = \alpha \times |\vec{u}_{10}|/(sin\ (\phi))^{0.5}$, ρ is the water density, ϕ is the latitude, $\alpha = 3.2(s)$ is an empirical scaling coefficient, and z is water depth. We have revised the manuscript in Line 189.

(3) Windage coefficient

We have moved the windage discussion to Section 2.2 (Lines 148-176), before the total velocity formulation in Section 2.3, so that all forcing components are introduced consistently before they are combined in the particle tracking model. We also expanded the explanation of how the two windage coefficients were obtained.

For the undrogued DX drifter, the cylindrical body had a diameter of 0.09 m and a height of 0.30 m, with approximately 0.03–0.05 m protruding above the water surface. Thus, the projected area exposed to air was $A_a \approx 0.09 \times (0.03\text{–}0.05) = 0.0027\text{–}0.0045\ m^2$, whereas the submerged projected area was $A_w \approx 0.09 \times (0.25\text{–}0.27) = 0.0225\text{–}0.0243\ m^2$. Using standard air and seawater densities and $C_{d,a}/C_{d,w} \approx 1$, the estimated windage coefficient is $r_{DX} \approx 0.012\text{–}0.016$. Therefore, $r = 0.015$ was adopted for the DX drifters.

For the drogued DO drifters, the exposed area above the water surface was similar to that of the DX drifters, but the submerged drag area was much larger because of the drogue plate positioned near 2 m depth. To avoid double-counting the two perpendicular plates, we used one effective projected drogue plate area: $A_{w,drogue} = 0.30 \times 0.30 = 0.09\ m^2$. The submerged cylindrical body contributed $A_{w,body} \approx 0.09 \times 0.26 = 0.0234\ m^2$. Thus, the total effective submerged projected area was $A_w \approx 0.0234 + 0.09 = 0.1134\ m^2$. This gives $r_{DO} \approx 0.0053\text{–}0.0069$ when $C_{d,a}/C_{d,w} \approx 1$ is used. Accordingly, $r = 0.005$ was adopted as a conservative geometry-based estimate for the DO drifters.

We also checked this estimate against published drag coefficients for drifter drag-area calculations. McCaffrey and Koeberle (2024) used $C_D = 0.74$ for cylindrical float elements and $C_D = 1.98$ for flat-plate drogue elements in their drifter drag-area analysis. Applying these values to the DO geometry gives $r_{DO} = \left[\rho_a(0.74A_a)/\rho_w\left(0.74A_{w,body} + 1.98A_{w,drogue}\right)\right]^{1/2}$, which yields $r_{DO} \approx 0.0035\text{–}0.0045$. This is slightly lower than, but close to, the adopted value of $r = 0.005$. Therefore, $r = 0.005$ does not underestimate the direct wind effect on the DO drifters; rather, it provides a physically reasonable and slightly conservative estimate.

We agree that the windage coefficient is associated with uncertainty. However, we did not tune r to minimize trajectory error, because doing so would mix two different objectives: estimating a drifter-specific windage coefficient and evaluating the relative contributions of geostrophic current, Ekman current, Stokes drift, and windage. Instead, we used *a priori* geometry-based values of r and kept them fixed across the forcing-combination experiments. In response to the reviewer's comment, we added a sensitivity test for the undrogued DX drifter, which is more directly exposed to wind forcing. The geometry-based windage coefficient used for DX in the manuscript was $r = 0.015$. To examine the sensitivity of the results to this parameter, we repeated the DX simulations using a smaller value, $r = 0.005$, representing an underestimated windage effect, and a larger value, $r = 0.030$, representing an overestimated windage effect. The sensitivity test showed that the optimal forcing combination changed when r was substantially modified. For $r = 0.005$, the lowest average MAE was obtained for C8, $u_g + u_e + u_s + u_w$, with $\overline{\text{MAE}} = 117.3$ km. For the geometry-based value, $r = 0.015$, the lowest average MAE was obtained for C7, $u_g + u_s + u_w$, with $\overline{\text{MAE}} = 42.9$ km. For $r = 0.030$, the lowest average MAE was obtained for C4, $u_g + u_w$, with $\overline{\text{MAE}} = 88.2$ km. Although different values of r produced different optimal forcing combinations, the geometry-based value $r = 0.015$ produced the smallest overall error among the tested cases. Specifically, the optimal MAE values for $r = 0.005$ and $r = 0.030$ were 117.3 km and 88.2 km, respectively, both of which were larger than the optimal MAE of 42.9 km obtained using $r = 0.015$. These results indicate that model performance is sensitive to the windage coefficient, but they also support the use of the geometry-based value $r = 0.015$ for the DX drifter. We therefore used the geometry-based coefficient as the primary estimate and used the additional simulations only to evaluate sensitivity, rather than tuning r freely to obtain the best trajectory fit. This clarification have been added to the revised manuscript in Lines 477-479.

Table R1. MAE values for PTM-DX sensitivity test using $r = 0.005$.

Day	C1	C2	C3	C4	C5	C6	C7	C8
5	130.2	128.2	123.1	129.8	106.3	117.1	90.0	29.2
10	252.4	243.2	223.7	237.2	207.1	220.9	166.0	138.2
30	473.4	449.3	300.2	423.5	260.2	348.0	209.0	161.1
75	550.2	541.3	290.9	459.2	219.8	369.3	145.0	140.7
Avg.	351.6	340.5	234.5	249.9	198.4	211.1	122.0	117.3

Table R2. MAE values for PTM-DX sensitivity test using the geometry-based value $r = 0.015$.

Day	C1	C2	C3	C4	C5	C6	C7	C8
5	130.2	128.2	123.1	89.0	106.3	60.9	25.3	20.4
10	252.4	243.2	223.7	162.3	207.1	104.5	29.5	43.9
30	473.4	449.3	300.2	216.4	260.2	104.6	55.6	114.0
75	550.2	541.3	290.9	164.6	219.8	98.3	61.2	105.4
Avg.	351.6	340.5	234.5	158.1	198.4	92.1	42.9	70.9

Table R3. MAE values for PTM-DX sensitivity test using $r = 0.030$.

Day	C1	C2	C3	C4	C5	C6	C7	C8
5	130.2	128.2	123.1	**25.6**	106.3	31.8	48.4	58.6
10	252.4	243.2	223.7	**69.8**	207.1	87.2	117.7	109.7
30	473.4	449.3	300.2	**131.9**	260.2	165.9	207.7	198.8
75	550.2	541.3	290.9	**125.5**	219.8	173.7	207.7	198.8
Avg.	351.6	340.5	234.5	**88.2**	198.4	91.7	116.3	113.2

(4) Smagorinsky diffusion

We have clarified how the Smagorinsky diffusion coefficient was computed. The horizontal diffusivity was calculated from the same velocity field used in each PTM experiment, not only from the geostrophic current. Thus, for the geostrophic-only case, the Smagorinsky coefficient was computed from the geostrophic velocity field, whereas for combined forcing cases it was computed from the corresponding total velocity field (Lines 218-219).

4. The authors mention (line 169 pg 6) that in order to evaluate the PTM versus drifter motion they compute one numerical particle for each drifter initial location. They should clarify whether they actually use an ensemble of particles obtained varying the gaussian random number. Using only one particle, corresponding to a single random realization, would not make sense, and they should repeat the tests using an appropriate ensemble

Thank you for this important comment. We agree that using only one numerical particle for each drifter initial location may make the comparison sensitive to a single stochastic realization of the random-walk diffusion term. We therefore repeated the PTM simulations using an ensemble of 10 numerical particles for each drifter initial location. The model–drifter comparison was then recalculated using the ensemble-mean MAE.

We show the original single-particle MAE table (Table R2) and the revised 10-particle ensemble-mean MAE table (Table R3). The absolute MAE values changed slightly because of the stochastic diffusion term, but the main optimal forcing combinations remained unchanged. For PTM-DX, C8 produced the lowest MAE at the early time of 5 days, whereas C7 produced the lowest MAE at later times and also had the lowest average MAE. Thus, except for the very early stage (~5 days), C7 remained the optimal forcing combination for DX. For PTM-DO, C8 consistently produced the lowest MAE in both the original single-particle case and the 10-particle ensemble case. We mentioned this in lines 508-514.

We also found a formatting error in the original manuscript table: for PTM-DX at 5 days, C7 had been incorrectly marked in bold as the best-performing case, although C8 actually had the lowest MAE at that time. This error has been corrected in the revised manuscript.

Table R2. Original MAE table using one numerical particle per drifter initial location.

	Day	C1	C2	C3	C4	C5	C6	C7	C8
PTM-DX	5	134.5	107.3	122.7	90	106.1	57	22	**19.3**
	10	251.4	242.6	221.1	166	209.6	92.6	**24.1**	35.8
	30	475.8	460.7	308.6	209	265.6	92	**54**	91
	75	562.5	606.1	347	145	243.9	90.8	**73.8**	83.2
PTM-DO	5	75.7	64.1	79.3	68.7	68.8	59.2	68.7	**55.3**
	10	146.5	135.6	140.2	123.1	129.4	113.8	120.1	**107**
	30	318	286.5	304.9	235.6	216.9	175.5	201.4	**110.7**
	75	537	487.9	487.9	377.1	459.6	322.6	410.3	**185.2**

Table R3. Revised MAE table using a 10-particle ensemble and ensemble-mean MAE.

	Day	C1	C2	C3	C4	C5	C6	C7	C8
	5	130.2	128.2	123.1	89	106.3	60.9	25.3	**20.4**

PTM-DX	10	252.4	243.2	223.7	162.3	207.1	104.5	**29.5**	43.9
	30	473.4	449.3	300.2	216.4	260.2	104.6	**55.6**	114
	75	550.2	541.3	290.9	164.6	219.8	98.3	**61.2**	105.4
PTM-DO	5	70.5	64.8	77.4	67	67.5	57.8	67.5	**53**
	10	142.9	133.5	143.1	125.7	129.4	114.3	120.1	**106**
	30	315.6	273.7	296.2	276	211	166.6	194.9	**117.7**
	75	528.1	488.7	477	472.9	359.2	285	330.9	**182.6**

5. How is the 'cluster' used in section 2.5 to compute relative dispersion defined? Is it given by the total set of drifters released, i.e. using six distinct deployment locations as a single point? Or is it an average of the six individual clusters? The behaviour at initial times seems strange to me

Thank you for pointing this out. We agree that the term “cluster” in Section 2.5 was not clearly defined and could therefore be misleading. Pairwise squared separation distances were first calculated among the available drifter trajectories, and only initially close drifter pairs with an initial separation distance of less than 200 m were retained. The relative dispersion and dispersion coefficient were then computed from this ensemble of initially close drifter pairs. This clarification has been added to Section 2.5 of the revised manuscript in Line 267.

6. The authors state that there is a Hyperbolic Point in the geostrophic velocity, causing the observed bifurcation. I think they should be more precise in their definition; they should look at the FSLE structure from the geostrophic velocity field to verify whether or not the bifurcation is indeed a HP.

Thank you for this important comment. In the revised manuscript, we clarified that the identification of the bifurcation region was not based solely on the instantaneous geostrophic velocity field. Instead, we examined the FTLE field derived from the geostrophic velocity and identified the spatial structure of the hyperbolic region using the red and blue FTLE ridges, which represent attracting and repelling manifolds, respectively (Shadden et al., 2005; Wiggins, 2005; Haller, 2015). Near the bifurcation region, the FTLE contours show a clear configuration of attracting and repelling ridges that is consistent with a hyperbolic Lagrangian structure. This ridge pattern supports our interpretation that the observed bifurcation was associated with a hyperbolic-point-like structure in the geostrophic flow field (Lines 296-301).

7. Also, the reason why the data driven combination outperform the one based on model velocity (Section 4) seems to be that the velocity bifurcation is not present in the model outputs. I find this strange, since the models should assimilate surface height and therefore induce a similar geostrophic velocity with respect to the altimetry products. Can the authors explain this point? And possibly compare the model velocities with the geostrophic one?

Thank you for this insightful comment. We agree that, because GLORYS and GOFS/HYCOM assimilate satellite altimetry, their large-scale sea-surface-height fields may contain information similar to that used to derive the altimetric geostrophic velocity. However, we found that the assimilated model products do not necessarily reproduce the same near-surface Lagrangian transport structure as the altimetry-derived geostrophic velocity. Therefore, even if the large-scale sea-surface-height signal is assimilated, the resulting large scale surface velocity gradients and finite-time transport barriers can differ from those obtained directly from the altimetry-derived geostrophic velocity.

We performed a direct comparison of the Lagrangian structures computed from the data-driven velocity combinations and from the model-derived velocity products using FTLE fields. The new figure shows that the data-driven velocity fields, especially G, GES, and GESW, contain a clear hyperbolic-type Lagrangian structure near the region where the observed drifter trajectories bifurcated. In contrast, the corresponding FTLE structures obtained from CMS and HYC are weaker, displaced, or less coherent in this region. Adding windage and Stokes drift to CMS and HYC modifies the FTLE ridges, but it does not fully recover the same transport-separating structure seen in the data-driven velocity fields.

Thus, the better performance of the data-driven combinations is not simply because they contain an additional velocity component, but because they better reproduce the finite-time Lagrangian structure controlling the early separation of the drifter pathways. The comparison also indicates that assimilation of sea-surface height in GLORYS and GOFS/HYCOM does not guarantee that the model-derived surface velocity will reproduce the same geostrophic velocity gradients and hyperbolic-type transport structure as the altimetry-derived geostrophic product. We have clarified this point in the revised manuscript and added the FTLE comparison figure to support the interpretation (Lines 565-591).

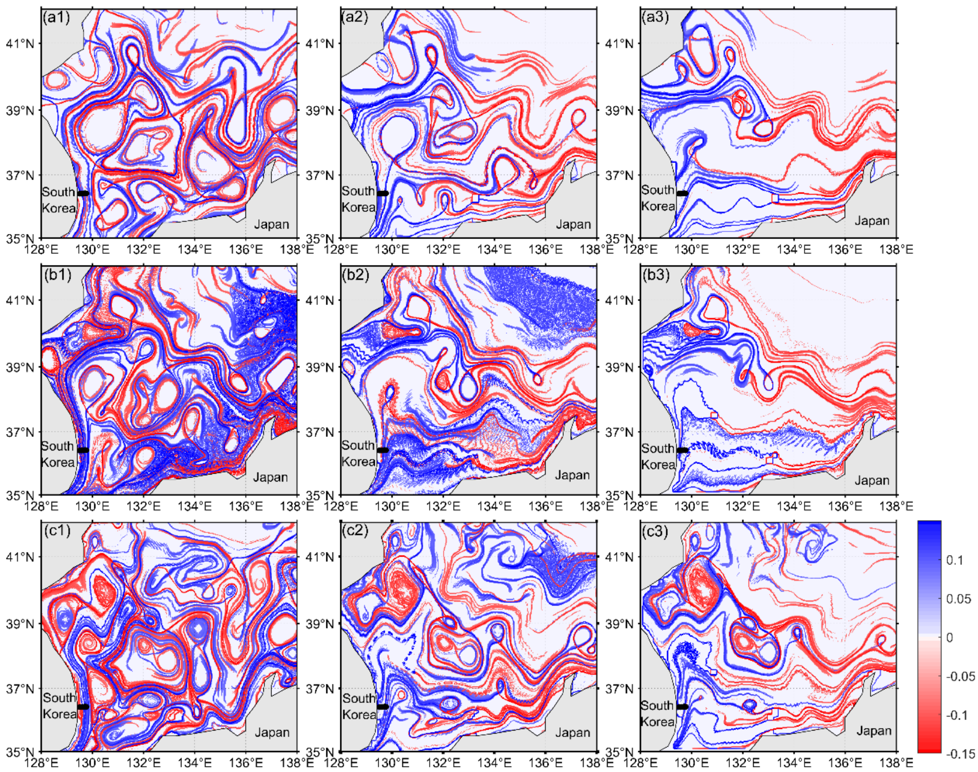

Figure 10. Finite-time Lyapunov exponent (FTLE) structures computed from one-week-averaged velocity fields. The panels show FTLE fields for (**a1**) u_g, (**a2**) $u_g + u_e + u_s$, (**a3**) $u_g + u_e + u_s + u_w$, (**b1**) CMS, (**b2**) CMS-w1, (**b3**) CMS-w1-st, (**c1**) HYC, (**c2**) HYC-w1, and (**c3**) HYC-w1-st. Here, u_g, u_e, u_s, and u_w denote geostrophic current, Ekman current, Stokes drift, and windage, respectively. CMS denotes the GLORYS reanalysis distributed by Copernicus Marine, and HYC denotes the GOFS analysis based on HYCOM.

8. Results from Ekman and windage (Section 3) are likely to strongly depend on parameterization and parameter values that are very difficult to evaluate. Did they do any sensitivity test? How robust are their conclusions?

Thank you for this important comment. We agree that the windage contribution can depend on the selected windage coefficient, r, and that this uncertainty should be discussed explicitly.

We clarify that the Ekman current in this study was not treated as an empirical tuning parameter. It was calculated directly from the wind-stress-based Ekman formulation using the prescribed wind field, latitude, and sampling depth. No additional adjustable coefficient was introduced for the Ekman current in the PTM simulations. Therefore, we did not perform a separate parameter sensitivity test for the Ekman component.

In contrast, windage was parameterized using the windage coefficient, r. In the main simulations, we used geometry-based estimates of $r = 0.015$ for the undrogued DX drifters and $r = 0.005$ for the drogued DO drifters. These values were derived from the exposed and submerged projected areas of each drifter type, rather than tuned to improve trajectory skill.

We also note that broadly tuning r is not straightforward in this study because DX and DO represent two physically different drifter types. The DX drifter is more surface-exposed and is therefore expected to have stronger direct windage, whereas the DO drifter has a larger submerged drogue area and is expected to have weaker direct windage. If r is varied too broadly for both drifter types, the parameter range of one drifter type can overlap with that of the other. Such tuning would blur the physical distinction between the DX and DO datasets and would mix two different objectives: calibrating a drifter-specific windage coefficient and evaluating the relative roles of geostrophic current, Ekman current, Stokes drift, and windage.

To evaluate the robustness of the DX results without treating r as a free tuning parameter, we conducted a limited windage sensitivity test for the DX case using three representative values: $r = 0.005$ as a lower-bound windage case, $r = 0.015$ as the geometry-based DX estimate, and $r = 0.030$ as an upper-bound windage case. The sensitivity test showed that the absolute trajectory errors varied with r, as expected. The use of $r = 0.015$, estimated from the DX drifter geometry, gave C7 ($u_G + u_S + u_W$) as the optimal forcing combination. When windage was underestimated using $r = 0.005$, the optimal combination shifted to C8 ($u_G + u_E + u_S + u_W$), suggesting that the weakened direct windage term was partly compensated by the inclusion of Ekman current. In contrast, when windage was overestimated using $r = 0.030$, the optimal combination shifted to C3 ($u_G + u_S$), indicating that excessive direct windage degraded the trajectory simulation and that the model favored a windage-free configuration. This indicates that the exact ranking of forcing combinations is sensitive to unrealistic underestimation or overestimation of r, but the geometry-based value $r = 0.015$ provides the most physically consistent representation of the DX drifter. More importantly, the sensitivity test supports the main conclusion that direct windage is an essential component for the surface-exposed DX drifters, but it should be constrained by drifter geometry rather than freely tuned to optimize trajectory skill.

We have added this to the revised manuscript in Lines 472-479.

9. I cannot see Tab 1-2 in the text

We apologize for this oversight. Tables 1 and 2 were inadvertently omitted from the original manuscript text. We have now added both tables to the revised manuscript and ensured that they are properly cited in the relevant sections.

More specific points

1. The definition of PTM should be better clarified when introduced in pg 2. There is a great variety of particle models; often they are based on Eulerian velocity from models outputs, and various types of stochastic terms are considered. In some cases stochastic terms are actually not used at all, if the velocity is assumed to be known with sufficient accuracy, for instance with high resolution models or HF Radars. I think the authors should clarify first of all that they do not include plastic behaviour (see point 1)), and that they use a simple random walk

model (eq 4), and focus on Eulerian velocities based on various data sets, each capturing a specific transport processes (geostrophic, Ekman, windage, Stokes drift). Only as a second step they also test model results.

Thank you for this helpful comment. We agree that the definition and scope of the PTM used in this study should be clarified. In the revised manuscript, we have added a clearer explanation when PTM is first introduced. Specifically, we now state that PTMs can be based on Eulerian velocity fields from observations or numerical models, and that stochastic terms may or may not be included depending on the application and the accuracy of the velocity fields. We also clarified that our study does not include plastic-specific behaviors such as sinking, fragmentation, buoyancy changes, or beaching. Instead, the simulated particles are treated as passive floating drifters.

In addition, we revised the description of Eq. (4) to state that our model uses a simple random walk scheme to represent unresolved subgrid-scale diffusion. We also clarified that the main focus of the study is the use of data-driven Eulerian velocity components, including geostrophic current, Ekman current, windage, and Stokes drift. The model-derived velocity products are then tested as an additional comparison, rather than being the main focus of the study (Lines 699-700, 717-720).

2. Figures should be improved. In Fig.1 it would be useful to have an insert that locates the geographic area. Also, the names of the various lands should be indicated in all the figures, and consistency should be maintained between Fig.1, 2,5, 6 (in terms of area, schematic, data sources, coordinates, names etc..) Also, the arrows in Fig.1b,c are not well visible.

Thank you for these helpful comments. We agree that the figures should be improved for clarity and consistency. In the revised manuscript, we have updated Figures 1 and 2. We apologize that Figures 5 and 6 have not yet been fully revised, but we will update them.

3. Please check for typos. Some examples are:

line 75, (pg 3,) TO validate

line 101(pg 4) THE drifters (instead of these).

title of Section 3 (line 208, pg 8)

Thank you for your detailed comment. We have carefully reviewed the manuscript and corrected the typographical and grammatical errors.

References

Davis, R. E.: Drifter observations of coastal surface currents during CODE: The method and descriptive view, Journal of Geophysical Research: Oceans, 90(C3), 4741–4755, 1985. https://doi.org/10.1029/JC090iC03p04741

Haller, G. (2015). Lagrangian coherent structures. *Annual Review of Fluid Mechanics*, 47, 137–162.

Novelli, G., Guigand, C., Cousin, C., Ryan, E. H., Laxague, N. J. M., Dai, H., Haus, B. K., and Özgökmen, T. M.: A biodegradable surface drifter for ocean sampling on a massive scale, Journal of Atmospheric and Oceanic Technology, 34(11), 2509–2532, 2017. https://doi.org/10.1175/JTECH-D-17-0055.1

Poulain, P.-M. and Gerin, R.: Assessment of the water-following capabilities of CODE drifters based on direct relative flow measurements, Journal of Atmospheric and Oceanic Technology, 36, 621–633, 2019. https://doi.org/10.1175/JTECH-D-18-0097.1

Poulain, P.-M., Centurioni, L. R., and Özgökmen, T. M.: Comparing the currents measured by CARTHE, CODE and SVP drifters as a function of wind and wave conditions in the southwestern Mediterranean Sea, Sensors, 22, 353, 2022. https://doi.org/10.3390/s22010353

Shadden, S. C., Lekien, F., and Marsden, J. E. (2005). Definition and properties of Lagrangian coherent structures from finite-time Lyapunov exponents in two-dimensional aperiodic flows. *Physica D: Nonlinear Phenomena*, 212, 271–304.

Wiggins, S. (2005). The dynamical systems approach to Lagrangian transport in oceanic flows. *Annual Review of Fluid Mechanics*, 37, 295–328.

III. Revised Manuscript with the changes highlighted in red

Data-Driven Enhancement of Ocean Surface Forcing for Accurate Floating Debris Transport Modelling in the East/Japan Sea

Hong T. M. Tran[1], Young G. Park[2], Jun M. Choi[3*]

[1]Fluid Mechanics Department, Faculty of Civil Engineering, Ho Chi Minh City University of Technology, Vietnam National University Ho Chi Minh City, Ho Chi Minh City, 700000, Vietnam
[2]Ocean Circulation and Climate Research Center, Korea Institute of Ocean Science and Technology, Busan, 49111, Republic of Korea
[3]Department of Ocean Engineering, College of Environment and Marine Sciences and Technology, Pukyong National University, Busan, 48513, Republic of Korea

Correspondence to: Jun M. Choi (jmchoi@pknu.ac.kr)

Abstract. Floating debris transport in marginal seas is controlled by a combination of geostrophic currents, wind-driven currents, wave-induced drift, and direct wind forcing, but the relative importance of these processes remains difficult to quantify without in-situ trajectory observations. This study evaluates near-surface forcing combinations for particle tracking in the East/Japan Sea using 33 GPS-tracked surface drifters deployed off the Korean coast in November 2021. The drifters revealed a clear cross-basin transport pathway toward the Japanese coastline and an early bifurcation near a hyperbolic-type Lagrangian structure. We used a particle tracking model to test combinations of geostrophic current, Ekman current, Stokes drift, and windage against the observed drifter trajectories using MAE and NCLS metrics. For undrogued DX drifters, the best performance was obtained by combining geostrophic current, Stokes drift, and windage. For drogued DO drifters, which sampled a deeper effective depth, the inclusion of all four forcing components provided the best agreement with observations. The optimized forcing combinations outperformed benchmark simulations driven by the GOFS analysis and GLORYS reanalysis in this specific event, primarily because they better reproduced the Lagrangian structure associated with the early trajectory bifurcation. Seasonal simulations showed that winter winds enhance eastward transport and beaching along Japan, whereas weaker summer winds allow mesoscale eddies to broaden particle dispersion. The present framework represents the fluid-dynamical component of near-surface particle transport and does not explicitly include plastic-specific fate processes such as fragmentation, biofouling-induced buoyancy changes, aggregation, settling, or resuspension.

1 Introduction

Millions of tons of plastic debris enter the ocean annually, posing a significant threat to marine ecosystems and human health. This debris accumulates in eddies and gyres (Lebreton, 2022; Maximenko et al., 2012; Thiel et al., 2018), washes ashore on coastlines (Chenillat et al., 2021; Cole et al., 2011; Cózar et al., 2014; Dobler et al., 2022; Nakakuni et al., 2024), and fragments into smaller pieces that disperse widely over time. These fragments pose serious risks to marine life through ingestion, particularly for species with vast foraging and migration ranges (Clark et al., 2023; Santos de Moura et al., 2020). Because plastic debris can facilitate disease transmission, damage critical habitats like coral reefs (Pinheiro et al., 2023), impact human health (Paul et al., 2024), disrupt food chains (Saeedi, 2024), and alter ecosystem dynamics (Tekman et al., 2022), accurate modeling to track the trajectories, distributions, and accumulation of floating plastic debris is urgently needed.

Particle Tracking Models (PTMs) have been widely implemented to model the transport and fate of floating materials (Lebreton et al., 2012; Onink et al., 2019). Such models have also been extended to study plastic debris dispersion in rivers discharging into the Indian Ocean (Irfan et al., 2024). Within marginal seas, PTM applications include tracking floating particle trajectories influenced by subsurface currents in the Gulf of Mexico (Liang et al., 2021), modeling oil particle pathways following the Deepwater Horizon oil spill (Mariano et al., 2011), tracking plastics in the Mediterranean Sea using surface currents and Stokes drift (Liubartseva et al., 2018), predicting particle trajectories in the Adriatic Sea (Castellari et al., 2001), simulating oil spill diffusion in the Sea of Okhotsk (Ono et al., 2013), and predicting surface debris movement in the East/Japan Sea (EJS) (Iwasaki et al., 2017).

PTMs are typically driven by Eulerian surface currents, which are heavily influenced by a combination of geostrophic currents, Ekman transport, Stokes drift, and windage (Röhrs et al., 2023; Sebille et al., 2020). Geostrophic currents, resulting from the balance between the Coriolis force and horizontal pressure gradients (Sudre et al., 2013), play a fundamental role in long-term ocean circulation and influence both surface and subsurface flows globally. Wind directly affects floating objects by exerting force on their exposed surface area, known as windage, often quantified by wind drift factors ranging from 0 to 5% of the wind speed (Gu et al., 2024; Tamtare et al., 2022). Ekman transport, driven by wind stress and the Coriolis effect, generates a vertical current profile within the upper ocean layers (Bressan, 2019) and has been linked to microplastic accumulation in subtropical regions (Onink et al., 2019). Stokes drift is a wave-induced Lagrangian drift that adds to the Eulerian surface current and therefore contributes directly to the transport of floating objects (Mao and Heron, 2008; Tamtare et al., 2022). Consequently, a systematic study determining which physical processes dominate particle movement is crucial for model accuracy.

Drifter experiments are an essential tool for evaluating PTM results that simulate the transport and dispersion of floating plastic debris and the corresponding physical processes on the ocean surface. In open oceans, validation is often supported by massive datasets such as the Global Drifter Program, which maintains thousands of drifters globally (Lumpkin et al., 2017; Maximenko et al., 2012). With the exception of the massive CODE-type drifter experiment in the Gulf of Mexico (Poje et al., 2014; D'Asaro et al., 2018), drifter experiments in marginal seas are typically constrained in scale, often relying on a small number of drifters to investigate local transport features. For instance, recent studies in the North Sea used only 6 to 12 drifters to validate surface transport models (Callies et al., 2017; Medina-Rubio et al., 2026), and similar process-oriented studies in the East China Sea were conducted with as few as 4 to 29 SVP-type drifters (Hsu et al., 2021; Sun et al., 2022). Sotillo et al. (2016) compiled a CODE-type drifter dataset in the Strait of Gibraltar to validate ocean models and track contaminants. The primary role of these experiments is to validate the surface currents that directly affect the accuracy of the debris tracking model. However, many tracking model studies in marginal seas still lack validation with in-situ drift data, or employ drifter types that are not suitable for tracking floating debris. Here, we utilized 33 surface drifters deployed simultaneously, tracking currents at a depth of 0.3 m. Although this number is smaller than open-ocean campaigns, it represents one of the largest synoptic datasets conducted in a marginal sea and constitutes the largest surface drifter experiment conducted in the EJS.

We investigate transport and dispersion in the EJS using PTMs validated with drifter experiments. The EJS, a marginal sea approximately 1,000 km wide, is a recognized "hot spot" for microplastic accumulation (Isobe et al., 2015; Kuroda et al., 2024) and is often described as a "miniature ocean" due to its encapsulation of major global oceanic processes, such as deep water formation, thermohaline circulation, and mesoscale eddy activity, within a relatively small and semi-enclosed basin (e.g., Ichiye, 1984; Kim et al., 2001; Talley et al., 2006). Bordered by the Korean Peninsula, Japan, and the Russian Far East, the EJS receives a mix of natural and anthropogenic materials, including plastic debris, transported by ocean currents such as the Tsushima Warm Current, a branch of the Kuroshio Current flowing from the East China Sea, as well as by wind (Park et al., 2021). Although the transport and distribution of plastic debris in the EJS have been studied (Iwasaki et al., 2017; Kim et al., 2021; Takeda and Isobe, 2024), there remains a lack of observational data in this marginal sea to validate particle trajectories and the specific physical processes influencing near-surface particle movement in the region.

In this study, we aimed to optimize the near-surface forcings that govern floating debris transport using a PTM validated with in-situ surface drifter observations. Here, "floating debris transport" refers to the fluid-dynamical transport component represented by passive particles moving near the ocean surface rather than the complete fate of specific macroplastic or microplastic particles. A drifter experiment was conducted to trace near-surface transport and assess the accuracy of simulated particle trajectories. In the results section, we identify the optimal combinations of key surface forcing components - geostrophic currents, Stokes drift, Ekman currents, and windage - for accurately modeling floating debris transport. By incorporating these forcings into the PTM, we simulated particle trajectories and compared them with observed drifter paths. Particle-specific processes such as fragmentation, biofouling-induced buoyancy change, aggregation, settling, and resuspension were not included in the present framework. This simplification is appropriate for the present objective because the simulated transport time scale is less than three months, whereas fragmentation has been reported to act on much longer, decadal time scales and to have little influence on large-scale microplastic transport over periods shorter than three years (Onink et al., 2022). In the discussion section, we evaluate the performance of the optimized forcing combinations relative to ocean analysis/reanalysis velocity products and further apply these combinations to estimate the seasonal variability of surface transport and beaching patterns of floating debris in the EJS.

2 Materials and Methods

2.1 Drifter experiment

Custom-made cylindrical drifters (Fig. 1a) were used to observe near-surface currents by tracking their movements in the EJS. The drifters, equipped with GPS trackers, were designed to collect location data at 5-minute intervals over several months. Each drifter measured 30 cm in height and 9 cm in diameter, with the top 3–5 cm protruding above the water surface when deployed. A total of 33 drifters were deployed, consisting of 23 undrogued drifters (hereafter referred to as DX drifters) and 10 drogued drifters (hereafter referred to as DO drifters). The drogue for the DO drifters consisted of two 30 cm × 30 cm plastic plates arranged perpendicularly and positioned at a depth of 2 m. By using surface drifters with slightly different depths, we aimed to investigate near-surface transport processes relevant to floating marine debris. Drifter positions were tracked from deployment until either beaching occurred or the signal was lost. The mean, minimum, maximum, and standard deviation of drifter lifetimes were 48.05, 12.2, 79.7, and 22.4 days, respectively. The location data were interpolated at 15-minute intervals and used for subsequent analysis. The DX and DO drifters were used to sample near-surface transport, but they were expected to respond differently to wind forcing. The DX drifter had a small part exposed above the sea surface, so it could be more affected by direct wind forcing and Stokes drift (Niiler et al., 1996; Röhrs et al., 2012).

In contrast, the DO drifter included a 30 × 30 cm drogue centered near 2 m depth to increase submerged drag and reduce direct wind slippage, following the general water-following principle of drogued surface drifters such as CODE and CARTHE drifters (Davis, 1985; Novelli et al., 2017). CARTHE drifters sample the upper approximately 0.6 m with wind-induced slip less than 0.5% of the 10 m wind speed, whereas CODE drifters sample the upper meter with reported downwind slip of about 0.1% of the wind speed (Poulain and Gerin, 2019; Poulain et al., 2022). Thus, the DX and DO drifters are treated here as custom observational benchmarks with different effective depths and windage sensitivities, rather than as exact equivalents of CODE or CARTHE drifters.

We deployed the drifters across the East Korea Warm Current (EKWC) region in the EJS (Fig. 1). The circulation along the eastern Korean Peninsula is primarily influenced by the northward-flowing EKWC and the southward-flowing North Korean Cold Current (NKCC), both of which are modulated by coastal currents, mesoscale eddies, and frontal structures (Lee et al., 2010). These flow systems generate complex near-surface transport pathways as drifters interact with regional oceanographic features (Prants et al., 2011; Onink et al., 2019). The drifters were released at six deployment locations near the Korean coast, with four DX drifters and either one or two DO drifters released at each location. The deployment started on 10 November 2021 at 01:40 UTC, and the subsequent groups were released at intervals over approximately 3 h. The one-week-averaged geostrophic current and 10-m wind velocity fields after drifter release are shown in Fig. 1c, together with the initial drifter location (black line). During this period, a strong northward geostrophic current was present along the Korean coast, while the 10-m wind field was predominantly eastward to northeastward over the deployment region. The corresponding one-week-averaged sea surface temperature (SST) and sea surface height (SSH) fields are shown in Fig. 1d, indicating mesoscale variability and frontal structures in the EJS. In particular, the mesoscale eddy evident near the drifter release locations likely influenced the subsequent pathways and final fates of the drifters.

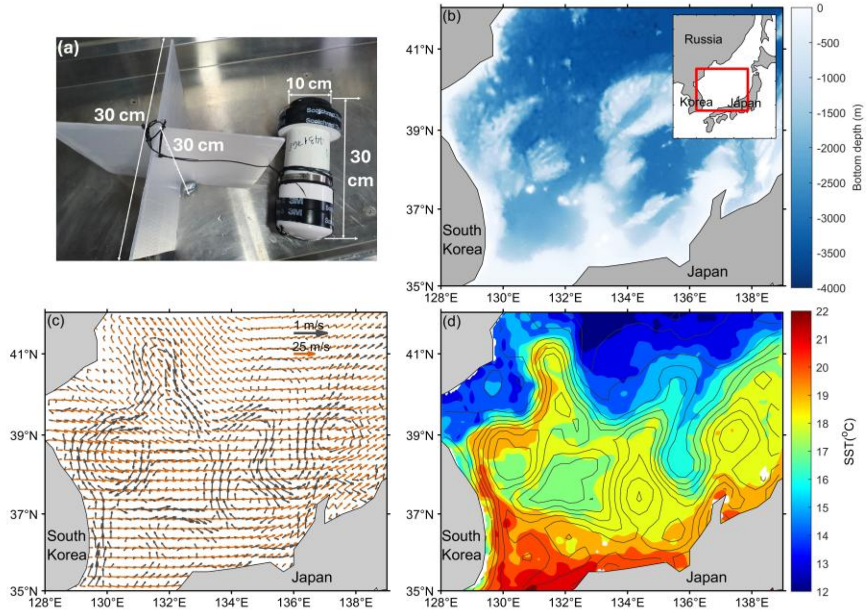

Figure 1. (a) Photograph and dimensions of the undrogued DX and drogued DO drifters. (b) Bathymetry of the East/Japan Sea, with the inset showing the surrounding geographic region. (c) Geostrophic current vectors (black) and 10-m wind velocity vectors (orange), both averaged over the first week after drifter release. The East Korea Warm Current (EKWC) is indicated in blue, and the reference vectors are shown in the upper-right corner. (d) Sea surface temperature (SST; color shading) and sea surface height (SSH; contour lines), both averaged over the first week after drifter release. Thick black lines indicate the initial drifter deployment locations.

2.2 Current data sets

Four current components were considered to be associated with the movement of drifters: geostrophic current (Sudre et al., 2013; Tamtare et al., 2022), Ekman current (Sudre et al., 2013; Huang et al., 2021), Stokes drift (Curcic et al. 2016; Iwasaki et al. 2017; Pärn et al. 2023), and windage (Gu et al., 2024). Geostrophic current ($\vec{u}_G$ or G), representing the background horizontal velocities, was obtained from the SEALEVEL_GLO_PHY_L4_MY_008_047 dataset. This dataset is a Copernicus Marine SEALEVEL Level-4 altimeter product processed by the CNES/CLS DUACS system. It combines multi-mission satellite altimeter observations, including Sentinel-6A, Sentinel-3A/B, Jason-3, SARAL/AltiKa, CryoSat-2, OSTM/Jason-2, Jason-1, TOPEX/Poseidon, Envisat, GFO, ERS-1/2, and Haiyang-2A/B. The current version of the product provides daily global ocean observations at a nominal spatial resolution of 0.125° and a temporal resolution of 1 day. For the particle-tracking calculations, the velocity fields were processed on the originally prepared computational grid with a grid spacing of approximately 0.25°, corresponding to about 25 km in the EJS. Wind velocity at 10 m above the sea surface ($\vec{u}_{10}$) was obtained from the ECMWF Reanalysis v5 (ERA5) dataset, with a spatial resolution of 1/4° and a temporal resolution of 1 hour. The wind data were converted to wind stress using the bulk formula ($\vec{\tau} = \rho_a C_d \vec{u}_{10} |\vec{u}_{10}|$), where ρ_a is the air density, and $C_d(=$

$10^{-3}(0.8 + 0.065|\vec{u}_{10}|)$) is the drag coefficient (Chen et al., 2020; Wu, 1982; Cushman-Roisin et al., 2011; Rypina et al., 2021).

The windage velocity, $\vec{u}_W$, was parameterized as $\vec{u}_W = r\vec{u}_{10}$, where r is the windage coefficient and $\mathbf{u}_{10}$ is the wind velocity at 10 m height. The coefficient r was estimated using a first-order balance between aerodynamic drag on the exposed part of the drifter and hydrodynamic drag on the submerged part:

$$r = \sqrt{\rho_a C_{d,a} A_a / \rho_w C_{d,w} A_w}, \tag{1}$$

where ρ_a and ρ_w are the densities of air and seawater, $C_{d,a}$ and $C_{d,w}$ are the drag coefficients in air and water, and A_a and A_w are the projected areas above and below the sea surface, respectively (Isobe et al., 2011). Because $C_{d,a}$ and $C_{d,w}$ were not measured directly for the custom drifters, we first assumed $C_{d,a}/C_{d,w} \approx 1$ as a geometry-based first-order approximation, consistent with previous studies (de Dominicis et al., 2016; van der Mheen et al., 2020). This assumption is appropriate for the DX drifters because the exposed and submerged parts are both cylindrical. For the DO drifters, however, the submerged flat drogue plate likely has a larger drag coefficient than the cylindrical float. Therefore, the assumption $C_{d,a}/C_{d,w} \approx 1$ should be interpreted as a conservative upper-bound estimate of windage rather than as a calibrated drag-coefficient ratio.

For the DX drifter, the cylindrical body had a diameter of 0.09 m and a height of 0.30 m, with approximately 0.03–0.05 m protruding above the sea surface. Thus, the exposed projected area was $A_a \approx 0.09 \times (0.03\text{–}0.05) = 0.0027\text{–}0.0045\ \text{m}^2$, whereas the submerged projected area was $A_w \approx 0.09 \times (0.25\text{–}0.27) = 0.0225\text{–}0.0243\ \text{m}^2$. Using $\rho_a/\rho_w \approx 1.2 \times 10^{-3}$ and $C_{d,a}/C_{d,w} \approx 1$, the estimated windage coefficient is $r_{DX} \approx 0.012\text{–}0.016$. Accordingly, $r = 0.015$ was adopted for the DX drifters.

For the DO drifter, the exposed area above the sea surface was similar to that of the DX drifter, but the submerged drag area was much larger because of the 0.30×0.30 m drogue plate positioned near 2 m depth. To avoid double-counting the two perpendicular plates, one effective projected drogue plate area was used: $A_{w,\text{drogue}} = 0.30 \times 0.30 = 0.09\ \text{m}^2$. The submerged cylindrical body contributed $A_{w,\text{body}} \approx 0.09 \times 0.26 = 0.0234\ \text{m}^2$. Thus, the total effective submerged projected area was $A_w \approx 0.0234 + 0.09 = 0.1134\ \text{m}^2$. Using $C_{d,a}/C_{d,w} \approx 1$, this gives $r_{DO} \approx 0.0053\text{–}0.0069$. The adopted value $r = 0.005$ is therefore a conservative geometry-based estimate for the DO drifters.

As an additional check, we considered published drag coefficients used in drifter drag-area calculations. McCaffrey and Koeberle (2024) used $C_D = 0.74$ for cylindrical float elements and $C_D = 1.98$ for flat-plate drogue elements. Applying these values to the DO geometry gives $r_{DO} = \left[\rho_a(0.74A_a)/\rho_w\left(0.74A_{w,\text{body}} + 1.98A_{w,\text{drogue}}\right)\right]^{1/2}$, which yields $r_{DO} \approx 0.0035\text{–}0.0045$. This value is slightly lower than, but close to, the adopted $r = 0.005$. Therefore, $r = 0.005$ does not underestimate the direct wind effect on the DO drifters; rather, it provides a physically reasonable and slightly conservative estimate. The windage coefficients used in this study were not empirically tuned to optimize trajectory skill, but were selected a priori from the drifter geometry and published drag-coefficient ranges.

Stokes drift ($\vec{u}_S$ or S) was calculated using the University of Miami Wave Model, version 1.0.1 (UMWM), over the domain 125°E-135°E, 25°N-35°N, with a horizontal resolution of 0.0083° and 22 depth levels. The model was forced with daily wind data from ECMWF/ERA5 and ETOPO1 (Hersbach et al., 2020; Amante et al., 2009) bathymetry and coastline data. The three-dimensional Stokes drift fields were determined using the following equation:

$$\overrightarrow{u_s}(z) = \int_0^{2\pi}\int_0^{\infty} \omega k^2 \frac{cosh[2k(d+z)]}{2sinh^2 kd} F(f) dk d\theta \tag{2}$$

, where ω, *k, d, z*, θ, and *F* are the angular frequency, wave number, mean water depth, the depth below the surface at which the Stokes drift is evaluated, the wave direction, and wavenumber variance spectrum, respectively (Haza et al., 2019). The computation was performed for the period from November 10, 2021, to January 30, 2022. Significant wave height and Stokes drift data were saved daily during the computation period. The Ekman transport ($\vec{u}_E$ or E) was calculated using the following equations:

$$u_E = \frac{\sqrt{2}}{\rho f d} e^{\frac{z}{d}} \left[\tau_x cos\left(\frac{z}{d} - \frac{\pi}{4}\right) - \tau_y sin\left(\frac{z}{d} - \frac{\pi}{4}\right)\right] \tag{3}$$

$$v_E = \frac{\sqrt{2}}{\rho f d} e^{\frac{z}{d}} \left[\tau_x sin\left(\frac{z}{d} - \frac{\pi}{4}\right) - \tau_y cos\left(\frac{z}{d} - \frac{\pi}{4}\right)\right] \tag{4}$$

, where the Ekman layer depth $d = \alpha|\vec{u}_{10}|/(\sin(\phi))^{0.5}$, ρ is the water density, ϕ is the latitude, $\alpha = 3.2(s)$ is an empirical scaling coefficient, and z is water depth (Rypina et al., 2021).

Furthermore, two model-derived surface velocity products were introduced for the benchmark comparison presented later in the discussion section. The first product was the GLORYS12V1 global ocean reanalysis distributed by Copernicus Marine (GLOBAL_MULTIYEAR_PHY_001_030), which provides daily mean fields at $1/12°$ horizontal resolution. The second product was the Global Ocean Forecast System (GOFS) analysis based on HYCOM/NCODA. These analysis/reanalysis velocity fields were used only as benchmark surface velocity products for comparison with the reconstructed forcing combinations. The sea surface temperature (SST) field from GLORYS12V1 was also used to describe the background thermal structure in the EJS.

2.3 The particle tracking model

The particle tracking model (PTM) used in this study treats the simulated particles as passive near-surface drifters advected by prescribed Eulerian velocity fields. The model does not explicitly represent plastic-specific processes such as fragmentation, biofouling-induced buoyancy change, settling, resuspension, or beaching. Instead, the PTM was used to evaluate the accuracy of different combinations of surface forcing components by comparing simulated particle trajectories with observed drifter trajectories. From a given horizontal velocity field, the particle displacement was estimated using a deterministic advection component and a stochastic diffusion component represented by a simple random walk scheme:

$$\vec{x}(t+\Delta t) - \vec{x}(t) = \vec{u}\Delta t + R\sqrt{2K_h \Delta t} \tag{5}$$

where $\vec{x}$ is the position vector of a Lagrangian particle, Δt is the time step in the PTM, set to 1800 s in this study, R is a random number drawn from a normal distribution at each time step, and K_h is the horizontal diffusion coefficient estimated using the

Smagorinsky scheme (Irfan et al., 2024; Jalón-Rojas et al., 2019; Seo et al., 2020). The stochastic term was included to account for unresolved subgrid-scale dispersion that is not represented by the prescribed Eulerian velocity fields.

The total drift velocity, $\vec{u}$, was determined by a linear combination of the physical processes described in Sect. 2.2:

$$\vec{u} = \vec{u}_G + \vec{u}_S + \vec{u}_E + \vec{u}_W \tag{6}$$

where $\vec{u}_G$, $\vec{u}_S$, $\vec{u}_E$, and $\vec{u}_W$ ($= r\vec{u}_{10}$) represent the geostrophic current (G), Stokes drift (S), Ekman current (E), and windage (W), respectively. These forcings were obtained from the datasets described in Sect. 2.2. Thus, the primary focus of this study was to construct and evaluate data-driven Eulerian velocity combinations representing specific near-surface transport processes, including geostrophic current, Stokes drift, Ekman current, and windage. Model-derived velocity products were tested separately as benchmark comparisons. Tidal currents were neglected in this study because they are relatively weak in the EJS (Jeon et al., 2014), and our result, not shown here, confirmed that tidal forcing had a negligible effect on particle trajectories in the region. Therefore, particle motion in the PTM is governed by prescribed Eulerian velocity fields, and the stochastic diffusion term is calculated using the Smagorinsky scheme based on the same Eulerian velocity fields.

Two sets of PTM simulations were conducted using the eight forcing combinations described in Table 1: PTM-DX, representing the undrogued DX drifters, and PTM-DO, representing the drogued DO drifters. For PTM-DX, near-surface forcings were used. Specifically, the Stokes drift was sampled from the shallowest available subsurface level of the wave-model output, approximately $z = -0.1$ m, while the Ekman current was evaluated near the surface. This depth is more representative of the effective submerged depth of the DX drifter than a strict air–sea interface value, because most of the cylindrical body was submerged within the upper 0.25–0.27 m of the water column. For PTM-DO, the Stokes drift and Ekman current were sampled at an effective depth of $z = -1.5$ m. This depth was estimated from the area-weighted hydrodynamic centroid of the submerged cylindrical body and drogue. The submerged cylindrical body had a projected area of approximately $0.09 \times 0.26 = 0.0234$ m^2, with its centroid near 0.13 m depth, whereas the effective projected area of one 0.30×0.30 m drogue plate was 0.09 m^2, centered near 2.0 m depth. The resulting area-weighted centroid was approximately 1.6 m below the sea surface. Thus, $z = -1.5$ m provides a reasonable effective sampling depth for representing the combined hydrodynamic response of the surface float and the submerged drogue. To evaluate the optimal forcing combination, one particle was released from each drifter's initial location, and each simulation was run for 79 days, corresponding to the longest observed drifter track.

Table 1. Forcing-component combinations used in the particle tracking model (PTM) simulations. The columns indicate the four velocity components: u_G (geostrophic current), u_E (Ekman current), u_S (Stokes drift), and u_W (ru_{10}). Circles (○) indicate that the component was included, whereas crosses (×) indicate that it was excluded. C1 represents the geostrophic-only reference case; C2–C4 represent two-component forcing cases; C5–C7 represent three-component forcing cases; and C8 represents the four-component forcing case. These combinations were used to simulate particle trajectories for comparison with the observed DX (undrogued) and DO (drogued) drifters. For PTM-DX, near-surface forcing components were used. For PTM-DO, the Ekman current and Stokes drift were sampled at an effective depth of 1.5 m to represent the deeper hydrodynamic response of the drogued drifters.

#	u_G	u_E	u_S	u_W
C1	○	×	×	×
C2	○	○	×	×
C3	○	×	○	×
C4	○	×	×	○
C5	○	○	○	×
C6	○	○	×	○
C7	○	×	○	○
C8	○	○	○	○

2.4 Evaluation of the particle trajectory

The particle trajectories calculated from the PTM were compared with observed drifter trajectories to determine the optimal combination of forcing components representing near-surface currents. The Mean Absolute Error (MAE), and the Normalized Cumulative Lagrangian separation (NCLS) (Kim et al., 2023) were used as metric to quantify the difference between particle and drifter trajectories. The equation for the MAE is given by,

$$MAE = \frac{1}{N}\sum_{i=1}^{N}(|\Delta Lon| + |\Delta Lat|) \tag{7}$$

where ΔLon and ΔLat are the differences between longitude and latitude of the observed and predicted trajectories. N is the number of the dataset (Kim et al., 2023). The longitude and latitude differences were first converted into physical distances (km) before calculating the MAE. Lower MAE values indicate more precise forecasts and better overall performance.

The NCLS is defined as the cumulative summation of the separation distance between the particle and drifter trajectories, weighted by the length of the drifter trajectories accumulated in time, as follow:

$$NCLS = \begin{cases} 1 - \frac{s}{n} & (NCLS \leq n) \\ 0 & (NCLS > n) \end{cases} \tag{8}$$

, where s $(= \sum_{i=1}^{N} D_i / \sum_{i=1}^{N} L_{o,i})$ denotes the normalized cumulative separation and n is a dimensionless value representing the allowed threshold. This study adopted a value of n = 1, consistent with the approach used by Kim et al., (2023), Liu et al., (2011) and Liu et al., (2014). D_i is the separation distance between drifter and particle trajectories at time step I, $L_{o,i}$ is the cumulative length of the observed trajectories at time step i. Thus, MAE and NCLS are the dimensional and nondimensional metrics, respectively, that measure the cumulative error between the simulated particle and observed drifter trajectories. NCLS values closer to 1 (with a range of 0 to 1) indicate a more accurate simulation.

2.5 Lagrangian diagnostics

The dispersion of observed drifters and simulated particles was quantified using two pair-based metrics: the relative dispersion ($R^2(t)$) and the Finite-Scale Lyapunov Exponent (FSLE). The relative dispersion indicates the growth in size of the drifter cluster relative to its center of mass as given by

$$R^2(t) = \frac{1}{N}\sum_{i=1}^{N}[x_i(t) - x_{cm}(t)]^2 \tag{9}$$

, where N is the number of drifters, $x_i(t)$ is the position vector of the i-th drifter at time t, and $x_{cm}(t)$ is the position vector of the center of mass of the drifter cluster at time t (LaCasce, 2008). For the relative-dispersion analysis, only drifter pairs with an initial separation distance of less than 200 m were retained. The corresponding dispersion coefficient (K) was estimated as

$$K = \frac{1}{4}\frac{\sigma_r^2}{t} \tag{10}$$

, where σ_r^2 represents the horizontal radial variance of the drifter or particle distribution. It is calculated from the mean squared distance of the particles from the center of mass of the cloud and can be interpreted as the spreading scale of an equivalent radially symmetric distribution. Thus, σ_r^2 quantifies the radial spreading of the drifter or particle cloud and was used to estimate the horizontal dispersion coefficient (Okubo, 1971; LaCasce, 2008). Different scaling regimes of $R^2(t)$ with time indicate different dispersion processes e.g., $R^2(t) \sim t$ for diffusive dispersion, $R^2(t) \sim t^3$ for Richardson dispersion, which correspond to $K \sim L^0$ and $K \sim L^{4/3}$, respectively, where L is $3\sigma_r$ represents the size of the particle cluster.

In addition to relative dispersion, the FSLE was also calculated to characterize the dispersion process. The FSLE (λ), measures the average rate of separation of initially nearby particles over a finite distance. It is calculated by tracking pairs of particles and measuring the time it takes for their separation to grow from an initial separation distance, δ_0, to a final separation distance, δ_f:

$$\lambda = \frac{1}{\langle \Delta t \rangle} ln\left(\frac{\delta_f}{\delta_0}\right) \tag{11}$$

, where Δt is the time required for the pair separation to grow from the initial separation scale δ_0 to the final separation scale δ_f, and the angle brackets $\langle\rangle$ denote an average over all particle pairs (Aurell et al., 1996). In this study, the final separation distance was defined as $\delta_f = 2\delta_0$. Therefore, the FSLE plotted as a function of separation distance δ represents the growth rate from $\delta_0 = \delta$ to $\delta_f = 2\delta$. A larger FSLE value indicates a faster rate of separation and thus stronger strain rate. Like the relative dispersion, difference scaling regimes of FSLE with respect to separation distance δ reveal different dispersion processes: $\lambda \sim \delta^{-1}$ for ballistic dispersion ($R^2(t) \sim t^2$), $\lambda \sim \delta^{-1/2}$ for Richardson-like dispersion ($R^2(t) \sim t^3$), and $\lambda \sim \delta^{-2}$ for diffusive dispersion ($R^2(t) \sim t$) (McWilliams, 2016).

The finite-time Lyapunov exponent (FTLE) was used to identify Lagrangian transport structures in the velocity fields. The FTLE quantifies the finite-time separation rate of initially neighboring particles and is defined as

$$\sigma_T(\vec{x}_0) = \frac{1}{|T|} ln\sqrt{\lambda_{max}(C)}, \tag{12}$$

where $\vec{x}_0$ is the initial particle position vector, T is the integration time, C is the Cauchy–Green strain tensor, and $\lambda_{\max}(\mathrm{C})$ is the largest eigenvalue of C (Haller and Yuan, 2000; Shadden et al., 2005; Haller, 2015). The Cauchy–Green strain tensor is given by

$$C = \left[\nabla\vec{F}_{t_0}^{t_0+T}(\vec{x}_0)\right]^T\left[\nabla\vec{F}_{t_0}^{t_0+T}(\vec{x}_0)\right], \tag{13}$$

where $\vec{F}_{t_0}^{t_0+T}(\vec{x}_0)$ is the flow map that gives the particle position at time $t_0 + T$ from the initial position $\vec{x}_0$ at time t_0. Ridges of the FTLE field have been widely used as indicators of Lagrangian coherent structures that organize material transport and mixing (Haller and Yuan, 2000; Shadden et al., 2005; Haller, 2015). In particular, repelling FTLE ridges are associated with material lines from which neighboring particles separate, whereas attracting FTLE ridges are associated with material lines toward which neighboring particles converge (Haller, 2001; Shadden et al., 2005). A finite-time hyperbolic region can be identified near the intersection of attracting and repelling ridges, where particles converge toward the attracting manifold and subsequently diverge along the repelling manifold (Haller and Yuan, 2000; Shadden et al., 2005). Such a saddle-type Lagrangian structure represents a dynamically important transport barrier and can explain the bifurcation of drifter trajectories.

3 Results

3.1 Drifter trajectory

All analyzed drifters deployed near the Korean coast, except those that stopped transmitting before beaching, ultimately reached the Japanese mainland or nearby islands within 13 - 68 days, while eight drifters stopped before beaching after 6–79 days (Table 2). Figure 2a shows the trajectories and final positions of the undrogued DX and drogued DO drifters. Within a few days after deployment, the drifters began diverging into two distinct pathways. One group, comprising 60% of the DO drifters and 27% of the DX drifters, moved northward along the eastern coast of Korea, likely influenced by the strong East Korea Warm Current (EKWC). The other group, consisting of 40% of the DO drifters and 73% of the DX drifters, drifted eastward toward the Japanese coast, primarily driven by prevailing westerly winds. The drifter bifurcation was further examined using FTLE structures derived from the geostrophic velocity field (Fig. 2b). The signed FTLE field shows that the bifurcation occurred near 130°E, 37.4°N, where attracting and repelling FTLE ridges are closely organized. In this representation, red ridges indicate attracting Lagrangian structures, whereas blue ridges indicate repelling Lagrangian structures (Fig. 2b). The observed drifters approached this region from the south to southwest and then separated into two branches, one moving northwestward and the other moving southeastward. This behavior is consistent with a finite-time hyperbolic-type bifurcation region, where particles converge toward an attracting manifold and subsequently diverge along a repelling manifold. This region was located near 130°E, 37.4°N, corresponding to the observed divergence of the drifter trajectories. The mean speeds of the DO and DX drifters were calculated as 0.28 m/s and 0.31 m/s, respectively.

Table 2. Summary of the final fate and drifting duration of observed drifters. The table lists the number and percentage of drifters in each fate category, the corresponding drifting-duration range, and the final fate.

Final fate	Number of drifters	Day from the release (day)
Stopped before beaching	8 (24%)	6-79
Beached at the mainland coastline	19 (57%)	24-68
Beached at the Nisinoshima island	2 (6%)	13
Beached at the Okinoshima island	3 (9%)	13-25
Beached at the Sado island	1 (3%)	45

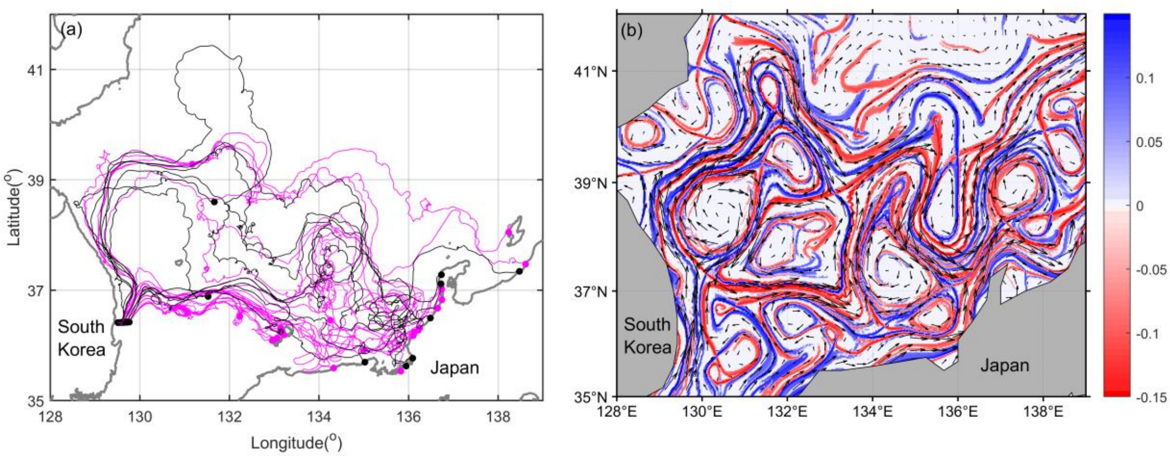

Figure 2. (**a**) Observed trajectories of undrogued DX drifters (black lines) and drogued DO drifters (magenta lines). Thick black lines indicate the initial deployment locations, and filled circles denote the final positions of drifters that remained at sea. (**b**) Signed Finite-time Lyapunov exponent (FTLE) field computed from the geostrophic velocity averaged over the first week after drifter release. Black arrows indicate the geostrophic velocity vectors. In the signed FTLE representation, blue and red ridges indicate repelling and attracting Lagrangian structures, respectively.

3.2 Drifter dispersion

The time evolution of the relative dispersion, $D^2(t)$ (Eq. 9), and the dispersion coefficient, $K(L)$ (Eq. 10), for the drifters is illustrated in Fig. 3. At very early times (t < 0.3 days) and small length scales (L < 1 km), the drifter cluster exhibited diffusive dispersion ($D^2 \sim t^1$). Beyond this initial stage, Richardson dispersion ($D^2 \sim t^3$, or equivalently, $K^2 \sim L^{4/3}$), was evident in the range of approximately 0.3 to 30 days, corresponding to length scales from L = 1 km to 100 km. During 0 < t < 3 (or L < 60 km), the DO drifters showed slightly greater dispersion than DX drifters, which was possibility attributed to the different passages determined at the hyperbolic region. The majority of DO drifters followed passage along the EKWC near the Korean coastline, where horizontal shear in the coastal current can enhance the dispersion. In contrast, the majority of DX drifters moved offshore, where the transport was dominated by spatially uniform wind in a narrow directional range, resulting in relatively weaker dispersion during the time. However, after approximately 3 days, as the DX drifters moved farther offshore, interactions with mesoscale eddies in the westerly downwind regions enhanced their dispersion, leading to super-Richardson behavior and causing their relative dispersion to exceed that of the DO drifters.

The estimated dispersion coefficients for all drifters were approximately 1, 20, and 1,000 m^2/s at scales of 1, 10, and 100 km, respectively, eventually saturating around 2,000 m^2/s in the EJS. The dispersion coefficient at the early stage was comparable to previous dye and drifter experiments in various waters, including coastal regions, inland waters, and open oceans (Okubo, 1971; Choi et al., 2020; Kim et al., 2024). For scales of 1–100 km, the growth in dispersion followed trends observed in open oceans, and the coefficient saturated when the length scale of the drifter cloud reached approximately 1/10 of the basin scale of the EJS (~2,000 km).

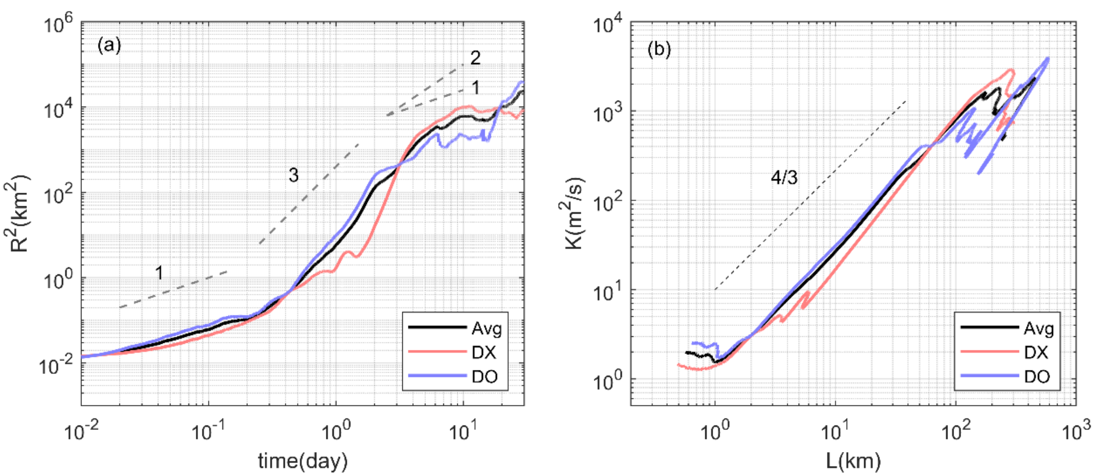

Figure 3. Relative dispersion ($R(t)^2$) (a) and dispersion coefficient ($K(L)$) (b) of the observed drifters. Panel (**a**) shows the time evolution of relative dispersion ($R(t)^2$), and panel (**b**) shows the dispersion coefficient ($K(L)$) as a function of length scale. The red line represents the undrogued (DX) drifters, the blue line represents the drogued (DO) drifters, and the black line indicates the average dispersion of all drifters (both DX and DO).

The FSLE values and trends for both DX and DO drifters were generally similar, but the FSLE values for DO drifters were slightly higher, particularly at very early times at spatial scales on the order of 10 meters and between 0.5 and 50 km. This pattern aligns with the dispersion coefficient K shown in Fig. 3b, where K is also larger for DO drifters over these scales. The difference in FSLE between DO and DX drifters is likely due to their distinct pathways delineated by the hyperbolic-type bifurcation region, consistent with observations from the relative dispersion analysis. The FSLE curves reveal distinct dynamical regimes across spatial scales. In the small-scale regime ($\delta < 0.5\ km$), DX drifters exhibit a slope close to -1, indicative of ballistic dispersion, possibly associated with well-aligned wind-induced transport. In the submeso- and mesoscale-range ($1\ km < \delta < 50\ km$), the slope for DX drifters becomes slightly gentler, and FSLE values remain lower than those of DO drifters. For DO drifters, the FSLE initially shows a steep slope near -2 at small scales ($\delta < 0.5\ km$), characteristic of a diffusive regime, then transitions to a slope of approximately -1/2 to -2/3, reflecting Richardson-like dispersion (Fig. 4). This behavior is consistent with the influence of coastal currents and mesoscale eddy interactions in the region. At larger scales (beyond ~150 km), both DX and DO drifters show a steepening of FSLE values again, corresponding to the scale of mesoscale eddies in the EJS.

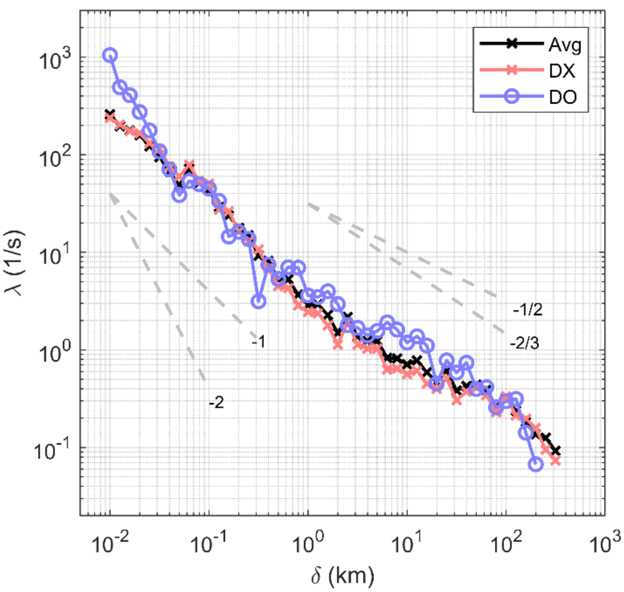

Figure 4. Finite-Size Lyapunov Exponent (FSLE), λ, as a function of separation distance, δ, for the observed drifters. The black line represents the average of all drifters, the red line represents the undrogued (DX) drifters, and the blue line represents the drogued (DO) drifters. The dashed gray lines indicate reference slopes of -2, -1, -1/2, and -2/3.

3.3 Particle trajectory

The performance of the forcing combinations detailed in Fig. 1 was evaluated by qualitatively comparing the observed drifter trajectories with simulated particle trajectories at two different depths: DX drifters were compared with PTM-DX particles driven by surface forcings (Fig. 5), while DO drifters were compared with PTM-DO particles driven by subsurface forcings at 1.5 m depth (Fig. 6). For the PTM-DX particles, increasing the number of forcing components improved the model's ability to replicate the bifurcation of drifter trajectories at the hyperbolic region, particularly when windage was included (Fig. 5f–h).

When simulations were driven solely by geostrophic currents (Fig. 5a), all particles drifted predominantly northward along the EKWC, ultimately accumulating in a mesoscale eddy centered near 132°E, 41°N. The addition of Ekman currents (Fig. 5b) did not result in significant differences. However, including Stokes drift (Fig. 5c) reduced the residence time of particles within the eddy and redirected them toward the Japanese coast. In all simulations without windage, particles remained confined along the EKWC, whereas simulations incorporating windage produced more realistic trajectories that aligned with observed DX drifter paths, which split into both coastal and offshore passages. For PTM-DO particles (Fig. 6), all forcing combinations resulted in transport along the EKWC. The variation among trajectories was less pronounced than for PTM-DX, indicating a stronger influence of the coastal current. Although none of the PTM-DO simulations captured the bifurcation at the hyperbolic-type bifurcation region, the simulation including all four components, geostrophic currents, Ekman currents, Stokes drift, and windage (Fig. 6h), most closely reproduced the observed DO drifter trajectories.

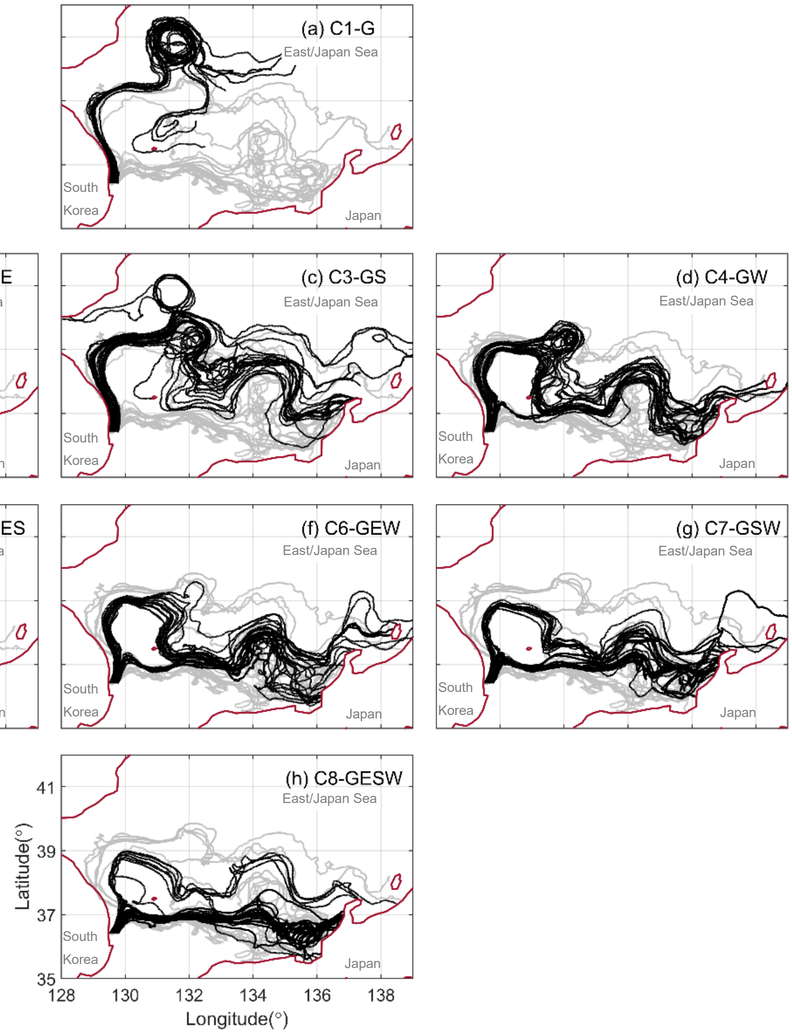

Figure 5. Particle trajectories using surface forcings (PTM-DX) simulated for 3 months. Panels (a-h) correspond to current combinations C1-C8 as described in Table 1. Black lines represent the simulated PTM-DX particle trajectories, while gray lines represent the observed DX drifter trajectories for comparison. The panels are arranged by the number of forcing components included: the first row shows single-component forcing (**a**); the second row shows two-component forcings (**b-d**); the third row shows three-component forcings (**e-g**); and the fourth row shows the four-component forcing (**h**). G, E, S, and W indicate geostrophic current, Ekman current, Stokes drift, and windage forcings, respectively.

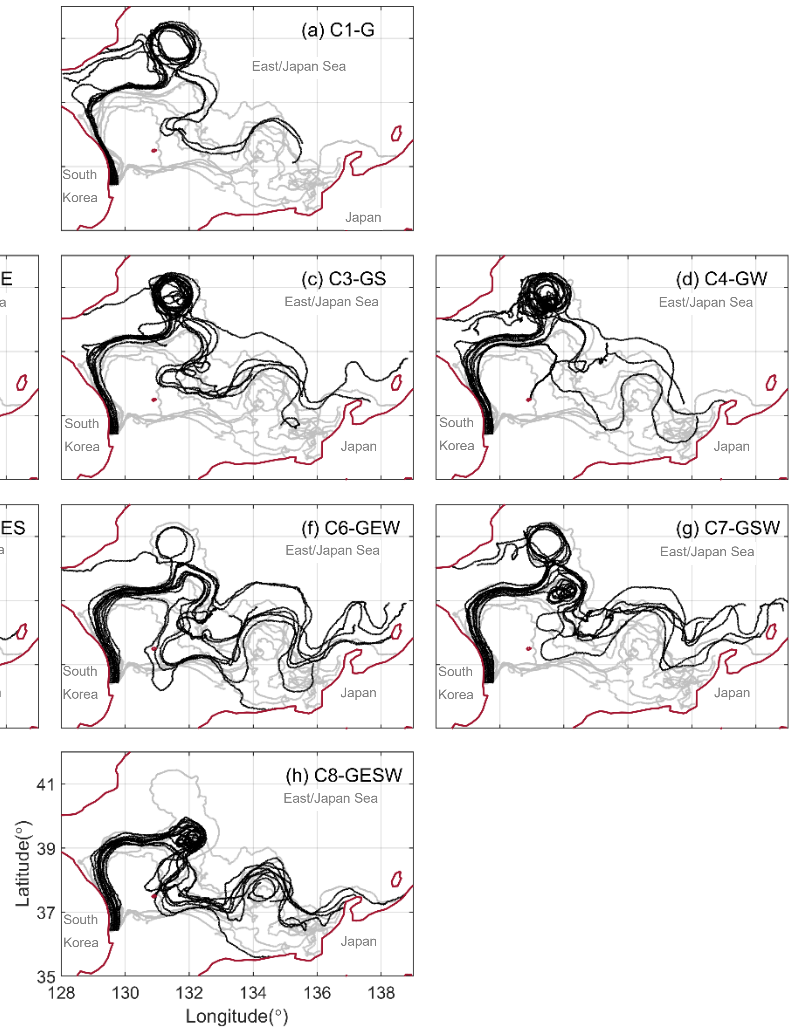

Figure 6. Particle trajectories using surface forcings (PTM-DO) simulated for 3 months. Panels (**a-h**) correspond to current combinations C1-C8 as described in Table 1. Black lines represent the simulated PTM-DO particle trajectories, while gray lines represent the observed DO drifter trajectories for comparison. The panels are arranged by the number of forcing components included: the first row shows single-component forcing (**a**); the second row shows two-component forcings (**b-d**); the third row shows three-component forcings (**e-g**); and the fourth row shows the four-component forcing (**h**). G, E, S, and W indicate geostrophic current, Ekman current, Stokes drift, and windage forcings, respectively.

3.4 Particle dispersion

Figure 7 presents the time evolution of relative dispersion, $D^2(t)$, for PTM-DX and PTM-DO particles under the eight forcing combinations (C1-C8). Overall, the two PTM sets exhibited comparable dispersion magnitudes and slopes; however, notable differences arose when windage was included. In cases where windage was applied (Fig. 7d and 7f-h), PTM-DX particles exhibited greater dispersion than PTM-DO particles, contrary to the drifter observations, which showed that DO drifters experienced higher dispersion, particularly at mesoscale distances. This discrepancy stemmed from the model's failure to reproduce the bifurcation at the hyperbolic-type bifurcation region. In the observations, both DX and DO drifters split between an offshore path and the EKWC path, albeit with different proportions: more DX drifters followed the offshore route, while more DO drifters remained along the EKWC, where coastal shear enhanced dispersion. In contrast, the simulations confined all PTM-DO particles to the EKWC path, while PTM-DX particles were distributed between both paths. Since particles restricted to the EKWC path experience weaker dispersion compared to those traversing both the EKWC and offshore routes, the PTM-DO simulations underestimated dispersion relative to PTM-DX, opposite to the pattern observed in the drifter data.

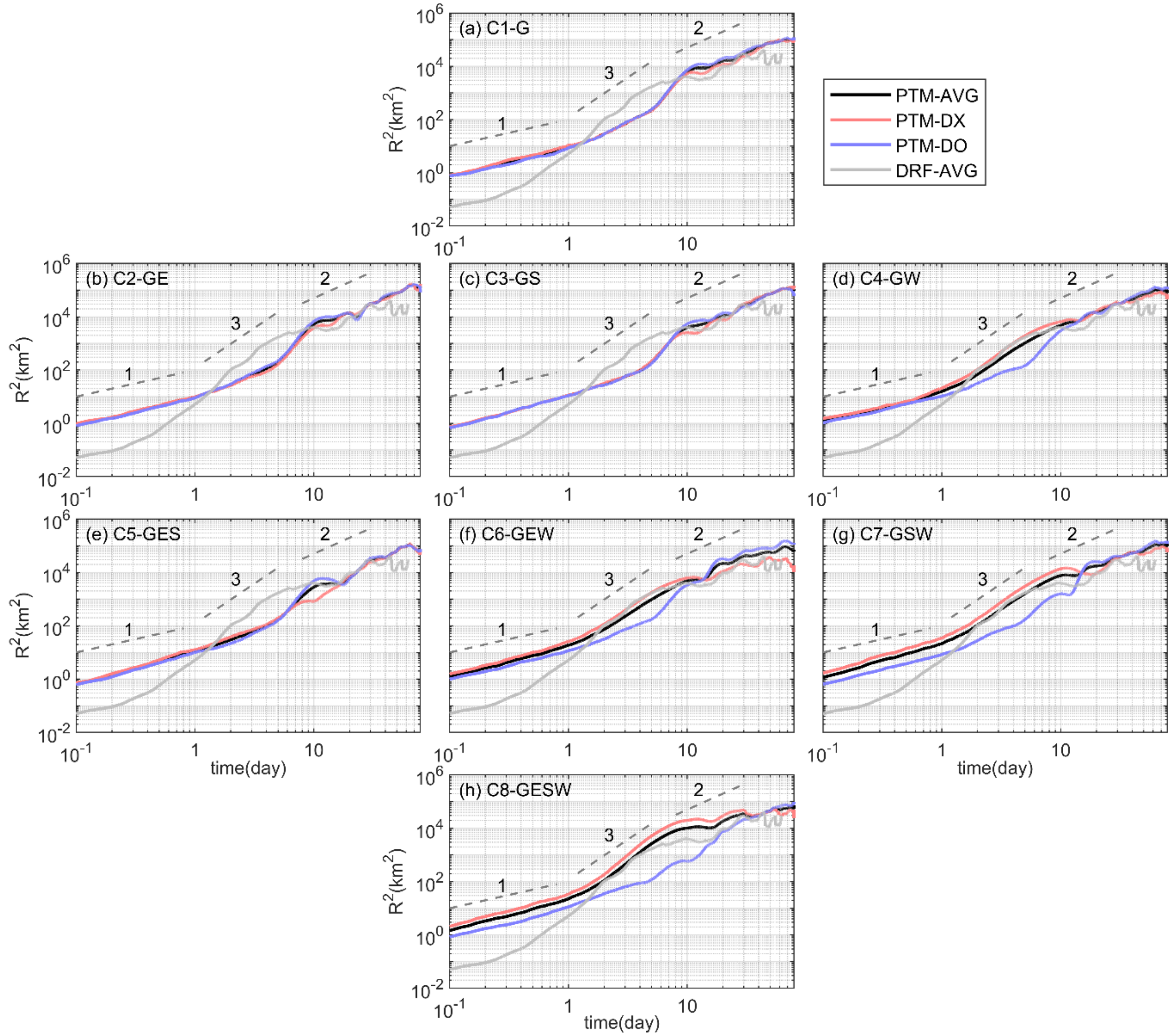

Figure 7. Relative dispersion ($R^2(t)$) of particles simulated with different forcing combinations (C1-C8) as described in Table 1, shown alongside observed drifter dispersion. Panels are arranged in the same order as in Fig. 5 and 6. Red and blue lines represent the relative dispersions for PTM-DX and PTM-DO simulations, respectively, and the gray line represents the average relative dispersion of the observed drifters for comparison. G, E, S, and W indicate geostrophic current, Ekman current, Stokes drift, and windage forcings, respectively.

Both particles and drifters exhibited a diffusive phase during the early stages; however, this phase persisted only briefly for the drifters ($t < 0.3$ days), while it extended significantly longer for the particles, up to approximately 2 days, until the average pairwise separation distance reached approximately 25 km, corresponding to the grid spacing of the velocity field used in the PTM calculations. As a result, the effective diffusivity of particle pairs separated by less than 25 km was substantially higher than that observed in the drifter data. This discrepancy arises from the Smagorinsky scheme, which applies a constant diffusion coefficient within each 25 km grid cell, leading to artificially enhanced diffusion at very early times in all PTM simulations. The domain-averaged horizontal diffusion coefficient during the drifter observation period (November 2021 to February 2022), computed using the Smagorinsky parameterization, was approximately 87.3 m^2/s. This value is consistent with the empirical, scale-dependent horizontal diffusivity described by Okubo (83.7 m^2/s), given by $K = 0.0103L^{1.15}$, where K is in cm^2/s and L is the spatial scale in cm. In this context, L is taken as $3\sigma_r$, or equivalently $3\Delta x$, with Δx = 25 km representing the grid spacing of the velocity field used in the PTM simulations.

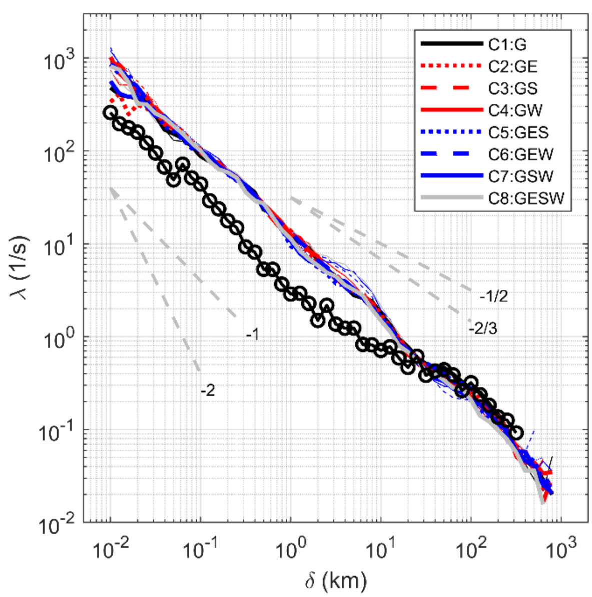

Figure 8. Finite-Size Lyapunov Exponent (FSLE), λ, as a function of separation distance, δ, for the simulated particles and observed drifters. The black line with circles represents the FSLE averaged for all observed drifters. Other colored lines show FSLEs for simulated particles from different forcing combinations (C1-C8, as listed in Table 1). Thinner lines indicate PTM-DX simulations, and thicker lines indicate PTM-DO simulations. The variation in FSLE values between different forcing combinations and between PTM-DX and PTM-DO were small.

The FSLE (λ) for the particle simulations (C1-C8) showed only minor differences among the various forcing combinations (Fig. 8). FSLE values from simulated particles and observed drifters became comparable at spatial scales greater than approximately 25 km, which aligns closely with the spatial grid size used for the current data in the simulations. At scales smaller than approximately 25 km, the FSLEs of the simulated particles were roughly three times greater than those observed from real drifters. This disparity at smaller scales occurs because particles in simulations are initially confined within grid cells, influenced significantly by numerical diffusion inherent in the Smagorinsky scheme. At these early times and small scales, the FSLE slopes for the drifters and particles are approximately -1, indicative of a ballistic dispersion regime. At intermediate spatial scales between about 25 km and 200 km, the FSLE curves for the simulated particles exhibit a slope closer to -1/2, signifying a local dispersion regime. Beyond roughly 200 km, the FSLE slopes steepen, approaching a slope of about -5/4, particularly evident in simulations where many particles eventually reach the coastline.

3.5 Data-driven optimal forcing combinations

The performance of the different data-driven forcing combinations was evaluated using the mean absolute error (MAE; Eq. 7) and the normalized cumulative Lagrangian separation skill score (NCLS; Eq. 8). The MAE values at selected time steps are summarized in Table 3, whereas the NCLS results are presented as temporal variations in Fig. 9 rather than in a separate table. Together, these two metrics were used to evaluate both the magnitude of trajectory error and the temporal consistency of model skill. The values in parentheses in Table 3 indicate the ratio of each MAE to the lowest MAE at the corresponding time step; therefore, values closer to 1 indicate better relative performance.

Table 3. MAE values for undrogued particles (PTM-DX) and drogued particles (PTM-DO) under 467 different forcing combinations (C1–C8) over time. Lower MAE values indicate better model 468 performance. Bolded values represent the lowest MAE for each time step. Values in 469 parentheses show the ratio of each MAE to the lowest MAE for that time step, a ratio closer to 470 1 denotes better relative performance.

		C1	C2	C3	C4	C5	C6	C7	C8
	day	u_G	u_{G+E}	u_{G+S}	u_{G+W}	u_{G+E+S}	u_{G+E+W}	u_{G+S+W}	$u_{G+E+S+W}$
PTM-DX	1	22.7 (2.1)	23.2 (2.1)	18.6 (1.7)	15.2 (1.4)	18.4 (1.7)	14.9 (1.4)	**10.8 (1.0)**	11.1 (1.0)
	5	134.5 (6.1)	107.3 (4.9)	122.7 (5.6)	90.0 (4.1)	106.1 (4.8)	57.0 (2.6)	**22.0 (1.0)**	19.3 (0.9)
	10	251.4 (10.4)	242.6 (10.1)	221.1 (9.2)	166.0 (6.9)	209.6 (8.7)	92.6 (3.8)	**24.1 (1.0)**	35.8 (1.5)
	30	475.8 (8.8)	460.7 (8.5)	308.6 (5.7)	209.0 (3.9)	265.6 (4.9)	92.0 (1.7)	**54.0 (1.0)**	91.0 (1.7)
	75	562.5 (7.6)	606.1 (8.2)	347.0 (4.7)	145.0 (2.0)	243.9 (3.3)	90.80 (1.2)	**73.8 (1.0)**	83.2 (1.1)
	avg.	289.4 (7.0)	288.0 (6.8)	203.6 (5.4)	125.0 (3.7)	168.7 (4.7)	69.5 (2.1)	**36.9 (1.0)**	48.1 (1.2)
PTM-DO	1	19.7 (1.3)	20.7 (1.3)	18.4 (1.2)	17.1 (1.1)	18 (1.2)	16.7 (1.1)	15.9 (1.0)	**15.4(1.0)**
	5	75.7 (1.4)	64.1 (1.2)	79.3 (1.4)	68.7 (1.2)	68.8 (1.2)	59.2 (1.1)	68.7 (1.2)	**55.3(1.0)**
	10	146.5 (1.4)	135.6 (1.3)	140.2 (1.3)	123.1 (1.2)	129.4 (1.2)	113.8 (1.1)	120.1 (1.1)	**107(1.0)**
	30	318.0 (2.9)	286.5 (2.6)	304.9 (2.8)	235.6 (2.1)	216.9 (2.0)	175.5 (1.6)	201.4 (1.8)	**110.7(1.0)**
	75	537.0 (2.9)	487.9 (2.6)	487.9 (2.6)	377.1 (2.0)	459.6 (2.5)	322.6 (1.7)	410.3 (2.2)	**185.2 (1.0)**

avg.	219.4 (2.0)	199.0 (1.8)	206.1 (1.9)	164.3 (1.5)	178.5 (1.6)	137.6 (1.3)	163.3 (1.5)	**94.7 (1.0)**

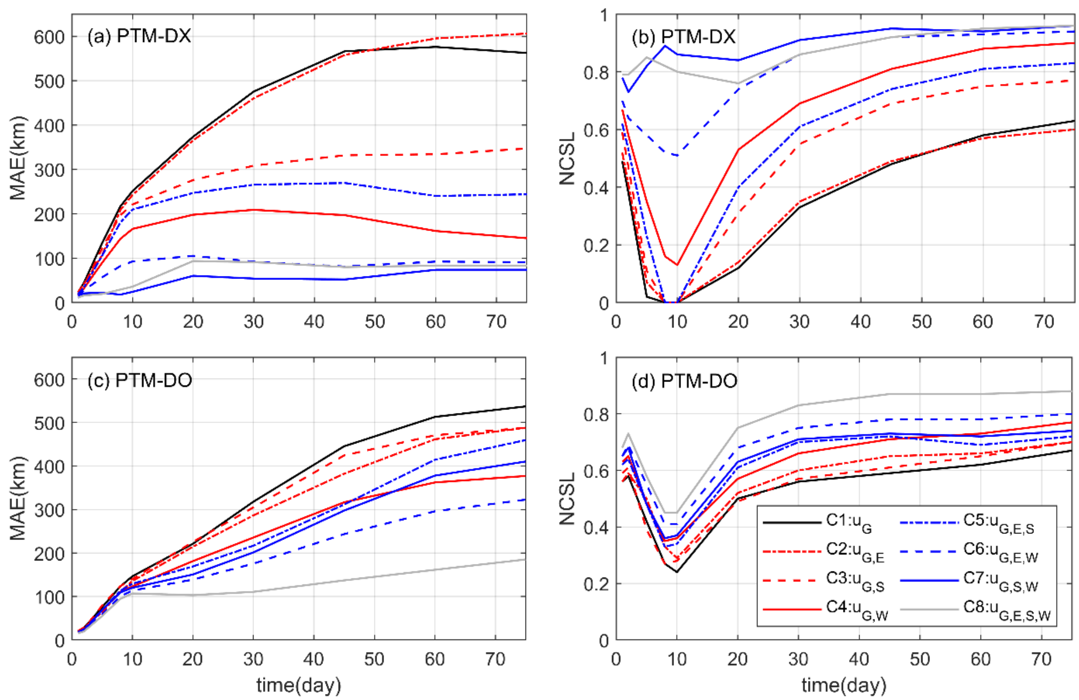

Figure 9. Temporal evolution of MAE for PTM-DX simulations (**a**) and PTM-DO simulations (**c**), and temporal evolution of NCLS for PTM-DX simulations (**b**) and PTM-DO simulations (**d**) for different forcing combinations (C1-C8, as listed in Table 1).

For PTM-DX, the simulation using only the geostrophic current (C1) showed the poorest overall performance, with an average MAE of 289.4 km. Adding the Ekman current to the geostrophic current (C2) did not improve the trajectory prediction, indicating that the Ekman component alone was insufficient to reproduce the observed DX drifter pathways. In contrast, the addition of windage substantially improved model performance. Among the two-component combinations, C4, which included geostrophic current and windage, reduced the average MAE to 125.0 km. This improvement suggests that direct wind forcing played an important role in the motion of the undrogued DX drifters.

Among the three-component combinations for PTM-DX, C7, which combined geostrophic current, Stokes drift, and windage, provided the best overall performance. C7 produced the lowest average MAE of 36.9 km and showed the highest or near-highest skill over most of the simulation period. Although C8, which included all four forcing components, showed slightly better performance at day 5, its average MAE was larger than that of C7. This result indicates that adding the Ekman current to the DX simulation did not further improve the prediction and could even degrade the trajectory skill after the early separation stage. Therefore, the optimal data-driven forcing combination for PTM-DX was identified as C7, consisting of geostrophic current, Stokes drift, and windage.

To evaluate the uncertainty associated with the windage coefficient without treating it as a free tuning parameter, an additional sensitivity test was conducted for PTM-DX, because the undrogued DX drifters are most directly exposed to wind forcing. The geometry-based value, $r = 0.015$, was compared with $r = 0.005$ and $r = 0.030$, representing weaker and stronger windage effects, respectively. The optimal forcing combination changed when r was substantially modified: $r = 0.005$ favored C8, $u_g + u_e + u_s + u_w$, with $\overline{\mathrm{MAE}} = 117.3$ km, whereas $r = 0.030$ favored C4, $u_g + u_w$, with $\overline{\mathrm{MAE}} = 88.2$ km. However, the geometry-based value $r = 0.015$ produced the lowest overall error, with C7, $u_g + u_s + u_w$, giving $\overline{\mathrm{MAE}} =$ 42.9 km. These results indicate that the trajectory skill is sensitive to the windage coefficient, but they also support the use of the geometry-based value $r = 0.015$ rather than tuning r freely to minimize trajectory error.

The temporal evolution of MAE and NCLS further supports this interpretation (Fig. 9a,b). The C1 and C2 simulations exhibited rapid error growth and eventually reached MAE values of approximately 600 km. In contrast, the simulations that included windage, particularly C6, C7, and C8, maintained substantially lower MAE values. A rapid change in MAE and NCLS occurred around day 10, corresponding to the period when the particles passed near the hyperbolic-type bifurcation region off the eastern Korean coast. In this region, small differences in the early simulated trajectories can determine whether particles follow the coastal northward pathway or the offshore eastward pathway. Thus, accurately representing the early wind-driven displacement near this bifurcation region was critical for reproducing the downstream trajectories of the DX drifters.

To further examine whether the MAE-based ranking was dominated by accumulated downstream separation after the early bifurcation, we also performed a segment-based MAE analysis for the DX simulations. The observed and simulated DX trajectories were divided into 3-day segments, and the MAE was calculated independently for each segment to evaluate short-term local trajectory skill. This analysis showed that the full forcing case, $u_g + u_e + u_s + u_w$, produced the lowest segment-based error, with $\overline{\mathrm{MAE}} = 28.7 \pm 3.7$ km, followed by $u_g + u_s + u_w$, with $\overline{\mathrm{MAE}} = 31.3 \pm 8.3$ km. Thus, while the cumulative MAE identified $u_g + u_s + u_w$ as the best integrated pathway predictor for DX, the segment-based analysis indicates that $u_g + u_e + u_s + u_w$ provided the most stable short-term local trajectory skill. This confirms that the windage- and Stokes-drift-inclusive forcings were important not only for the accumulated downstream pathway, but also during the early bifurcation stage.

For PTM-DO, the differences among the forcing combinations were less pronounced than for PTM-DX, reflecting the weaker direct wind response of the drogued drifters. Nevertheless, the inclusion of additional forcing components generally improved the trajectory prediction. The geostrophic-only case (C1) produced an average MAE of 219.4 km, while C4 reduced the average MAE to 164.3 km. Among the three-component combinations, C6, which included geostrophic current, Ekman current, and windage, showed the best performance, with an average MAE of 137.6 km. This result suggests that the Ekman component was more important for the drogued DO drifters than for the undrogued DX drifters, consistent with the deeper effective sampling depth of the DO drifter.

The best overall performance for PTM-DO was obtained with C8, which included geostrophic current, Ekman current, Stokes drift, and windage. C8 produced the lowest MAE at all selected time steps and reduced the average MAE to 94.7 km. The NCLS evolution also showed that C8 consistently maintained the highest trajectory skill for the DO simulations (Fig. 9c,d). Therefore, unlike the DX case, the inclusion of all four forcing components was necessary to reproduce the observed DO drifter trajectories most accurately.

To examine whether the identified optimal forcing combinations were affected by the stochastic random-walk diffusion term, an additional ensemble-sensitivity test was conducted using 10 particles for each drifter initial location. The deterministic velocity fields were kept identical to those in the original simulations, while only the Gaussian random sequences in the diffusion term were varied. The resulting ensemble-mean MAE values differed slightly from the original single-particle results, but the main forcing rankings remained unchanged. For PTM-DX, C8 produced the lowest MAE at the early time of 5 days, whereas C7 remained the best-performing case at later times and for the average MAE. For PTM-DO, C8 remained the best-performing forcing combination. These results indicate that the stochastic diffusion term affects the exact MAE values but does not control the main conclusion regarding the optimal forcing combinations.

Overall, the optimal forcing combination differed between the two drifter types. For the undrogued DX drifters, the best performance was achieved by combining geostrophic current, Stokes drift, and windage, indicating that near-surface transport was strongly controlled by wave-induced drift and direct wind forcing. For the drogued DO drifters, the full forcing combination including Ekman current was required, suggesting that the deeper drogued drifters were more strongly influenced by subsurface wind-driven shear. These results demonstrate that the optimal PTM forcing depends on the effective sampling depth and wind exposure of the drifting object, and that a single surface-current forcing configuration may not be appropriate for all types of floating debris or drifters.

4 Discussions

4.1 Comparison with model-derived velocity products

The optimized data-driven forcing combinations were further compared with simulations driven by model-derived surface velocity products. In this comparison, the GOFS analysis based on HYCOM/NCODA and the GLORYS12V1 reanalysis distributed by Copernicus Marine were used as benchmark velocity fields. These products are referred to hereafter as HYC and CMS, respectively, to remain consistent with the notation used in Table 4. The purpose of this comparison was not to repeat the full forcing-decomposition experiment conducted for the data-driven approach, because these analysis/reanalysis products already assimilate observations and provide dynamically consistent surface velocity fields that may include both geostrophic and ageostrophic wind-driven components. Instead, the model-derived velocities were used directly, and additional direct windage and Stokes drift terms were tested to examine whether these processes improved the simulated pathways of the undrogued DX drifters.

Table 4. Table 4. MAE and NCLS values for PTM-DX simulations driven by model-derived surface velocity products, namely the GOFS analysis based on HYCOM/NCODA and the GLORYS12V1 reanalysis distributed by Copernicus Marine, with and without additional windage and Stokes drift. HYC denotes the GOFS/HYCOM analysis, and CMS denotes the GLORYS12V1 reanalysis product GLOBAL_MULTIYEAR_PHY_001_030. W1 and W2 denote windage terms corresponding to 1.5% and 3.0% of the 10-m wind speed, respectively, and ST denotes the addition of Stokes drift calculated from the wave model.

	day	CMS	CMS-W1	CMS-W2	CMS-W1-ST	HYC	HYC -W1	HYC -W2	HYC-W1-ST
MAE	1	22.0 (2.0)	14.6 (1.4)	8.1 (0.8)	5.5 (0.5)	25.2 (2.3)	14.6 (1.4)	13.4 (1.2)	15.5 (1.4)
	5	134.9 (6.1)	43.6 (2.0)	40.1 (1.8)	39.2 (1.8)	76.8 (3.5)	25.8 (1.2)	30.3 (1.4)	21.7 (1.0)
	10	237.0 (9.8)	69.0 (2.9)	64.7 (2.7)	60.0 (2.5)	174.4 (7.2)	32.1 (1.3)	61.0 (2.5)	26.5 (1.1)
	30	415.9 (7.7)	72.0 (1.3)	165.8 (3.1)	150.7 (2.8)	234.7 (4.3)	158.1 (2.9)	201.7 (3.7)	156.1 (2.9)
	75	413.6 (5.6)	126.6 (1.7)	175.7 (2.4)	163.7 (2.2)	182.7 (2.5)	195.4 (2.6)	201.7 (2.7)	163.4 (2.2)
	avg.	244.7 (6.2)	65.2 (1.9)	90.9 (2.2)	83.8 (2.3)	138.8 (4.0)	85.2 (1.9)	101.6 (2.3)	76.64 (2.1)
NCLS	1	0.52 (1.3)	0.70 (1.1)	0.84 (0.9)	0.87 (1.1)	0.52 (1.3)	0.72 (1.1)	0.74 (1.1)	0.71 (0.9)
	5	0.02 (2.0)	0.67 (1.2)	0.70 (1.1)	0.71 (0.9)	0.39 (1.5)	0.80 (1.0)	0.75 (1.1)	0.83 (1.0)
	10	0.00 (2.0)	0.62 (1.3)	0.63 (1.3)	0.64 (0.7)	0.05 (1.9)	0.82 (1.0)	0.64 (1.3)	0.85 (1.0)
	30	0.41 (1.5)	0.89 (1.0)	0.76 (1.2)	0.78 (0.9)	0.65 (1.3)	0.74 (1.2)	0.74 (1.2)	0.74 (0.8)
	75	0.72 (1.3)	0.91 (1.1)	0.94 (1.0)	0.95 (1)	0.87 (1.1)	0.92 (1.0)	0.95 (1.0)	0.95 (1.0)
	avg.	0.33 (1.6)	0.76 (1.1)	0.77 (1.1)	0.79 (0.9)	0.50 (1.4)	0.80 (1.1)	0.76 (1.1)	0.82 (0.9)

Table 4 summarizes the MAE and NCLS values for PTM-DX simulations driven by HYC and CMS, with and without additional windage and Stokes drift. In Table 4, W1 and W2 denote windage terms corresponding to 1.5% and 3.0% of the 10-m wind speed, respectively, while ST denotes the addition of Stokes drift calculated from the wave model. These percentages therefore refer to the windage coefficient, not to a scaling of Stokes drift. The values in parentheses are normalized by the performance of C7, which was the optimal data-driven forcing combination for PTM-DX.

The model-derived simulations generally showed poorer trajectory skill than the optimized data-driven forcing combination. Although the addition of windage and Stokes drift improved some HYC and CMS cases, the resulting MAE values remained larger and the NCLS values remained lower than those obtained with C7. This indicates that the poorer performance of HYC and CMS was not caused simply by the absence of direct windage or Stokes drift. Rather, it was related to differences in the local near-surface velocity structure during the early stage of the simulation, when small trajectory errors strongly affected the subsequent downstream pathway. The temporal resolution of the velocity products may also have contributed to these differences. The GLORYS12V1 reanalysis provides daily mean fields, whereas the wind-related components in the reconstructed forcing were derived from hourly ERA5 wind forcing. Therefore, high-frequency near-surface wind-driven variability may have been more strongly smoothed in the GLORYS-based simulation than in the reconstructed forcing fields. To examine this mechanism, FTLE fields were computed using one-week-averaged velocity fields from the drifter release date within the same domain used for the velocity-field comparison. Figure 10 compares the FTLE structures obtained from the data-driven velocity fields and the model-derived velocity fields. The first row shows the FTLE fields for the geostrophic current alone, the data-driven combination without windage, and the data-driven combination including windage. The second and third rows show the corresponding CMS- and HYC-based cases, respectively, with and without additional windage and Stokes drift.

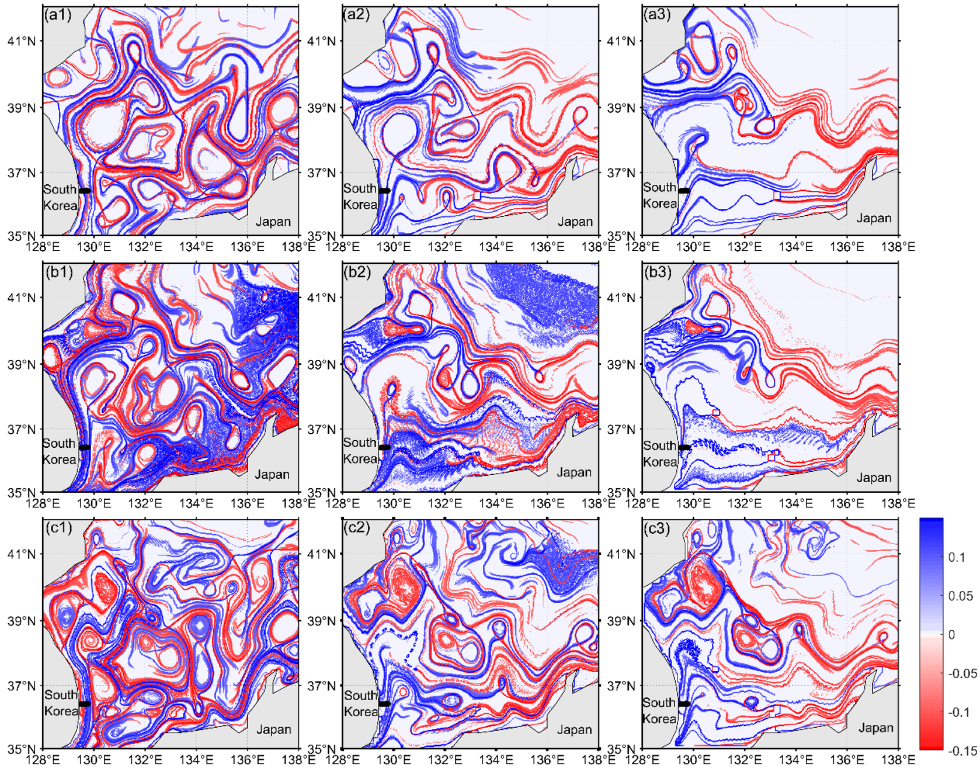

Figure 10. Finite-time Lyapunov exponent (FTLE) structures computed from one-week-averaged velocity fields. The panels show FTLE fields for (**a1**) u_g, (**a2**) $u_g + u_e + u_s$, (**a3**) $u_g + u_e + u_s + u_w$, (**b1**) CMS, (**b2**) CMS-w1, (**b3**) CMS-w1-st, (**c1**) HYC, (**c2**) HYC-w1, and (**c3**) HYC-w1-st. Here, u_g, u_e, u_s, and u_w denote geostrophic current, Ekman current, Stokes drift, and windage, respectively. CMS denotes the GLORYS reanalysis distributed by Copernicus Marine, and HYC denotes the GOFS analysis based on HYCOM.

The data-driven velocity fields showed a clear transport-separating FTLE structure near the early bifurcation region off the eastern Korean coast. In particular, the geostrophic current field and the data-driven combined velocity fields retained a ridge structure in which attracting and repelling FTLE ridges were closely aligned or intersected near the region where the observed drifter trajectories initially separated. This structure is consistent with a hyperbolic-type bifurcation region rather than a mathematically exact, stationary hyperbolic point. Because the drifters were released close to this Lagrangian transport boundary, small differences in initial position and forcing could separate the particles into different pathways: one following the coastal northward route along the East Korea Warm Current and the other moving offshore and subsequently eastward.

In contrast, the CMS- and HYC-based FTLE fields did not show a comparable hyperbolic-type ridge intersection in the same region. The model-derived FTLE structures were smoother, weaker, or spatially displaced relative to the data-driven FTLE structure. Adding windage and Stokes drift to the CMS and HYC velocity fields changed the magnitude and direction of particle advection, but it did not reconstruct the same transport-separating FTLE pattern near the release region. This explains why the model-derived simulations could not reproduce the early pathway separation as accurately as the optimized data-driven forcing combination.

The FTLE comparison therefore supports the trajectory-based evaluation in Table 5. The improved performance of the data-driven approach does not imply that the GOFS analysis or GLORYS12V1 reanalysis lack geostrophic dynamics. Both products assimilate sea-level information, but their surface velocity fields are dynamically adjusted by the model physics, data-assimilation scheme, vertical mixing, spatial resolution, and temporal averaging. Rather, the result indicates that the early drifter bifurcation was highly sensitive to the local structure of the near-surface velocity field. The data-driven geostrophic-based forcing combinations better preserved the FTLE ridge structure associated with this bifurcation region, whereas the HYC and CMS velocity fields smoothed or displaced the local transport boundary. Consequently, once the simulated particles selected an incorrect pathway during the first stage of transport, the downstream separation error increased rapidly, leading to larger MAE and lower NCLS values over the full trajectory.

Overall, the comparison with HYC and CMS confirms that the key advantage of the optimized data-driven forcing is not only the inclusion of additional windage or Stokes drift, but also the ability to reproduce the local Lagrangian transport structure controlling the early bifurcation of the drifter pathways. This finding emphasizes that accurate representation of transport-separating structures near the release region is essential for predicting the fate of near-surface floating particles in the East/Japan Sea.

4.2 Seasonal variation of atmospheric and oceanic forcings

The seasonal variation of waves and winds that potentially influence the transport of floating debris is illustrated in Fig. 11. Both significant wave height (SWH) and wind speed follow a clear seasonal pattern, increasing in the order of summer (June-August), fall (September-November), spring (March-May), and winter (December-February). During fall and winter (Fig. 11g and 11h), the EJS is subject to persistent and strong northwesterly winds, which generate significantly higher wave heights near the Japanese coastline due to fetch-limited wave development from the Korean Peninsula (Chen et al., 2002; Park et al., 2005; Ebuchi, 1999). Monthly averaged satellite-derived SWHs show a pronounced seasonal variability, with high values exceeding 2.5 m in winter and low values below 1 m in summer (Woo and Park, 2017), consistent with the seasonal averages depicted in Fig. 10. This spatial asymmetry in wave height enhances wave-driven surface transport (Stokes drift) toward the Japanese coast during winter. The mean winter SWH reaches 1.68 m, with a maximum of 2.58 m. In contrast, during summer, the mean SWH decreases to 0.55 m, with a peak of 0.82 m, and wave propagation is influenced by prevailing southerly winds, which tend to shift northward.

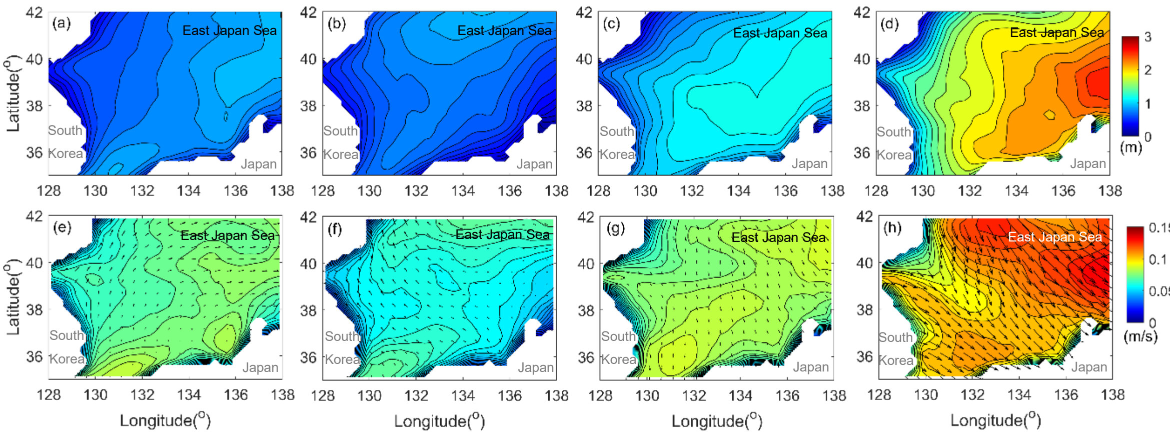

Figure 11. The mean of significant wave height (**a-d**), wind (**e-f**) in EJS for each season in 2021: (**a,e**) spring (March 01-May 30), (b,f) summer (June 01-August 30), (**c,g**) autumn (Septemper 01-November 30), and (**d,h**) winter (December 01-February 28).

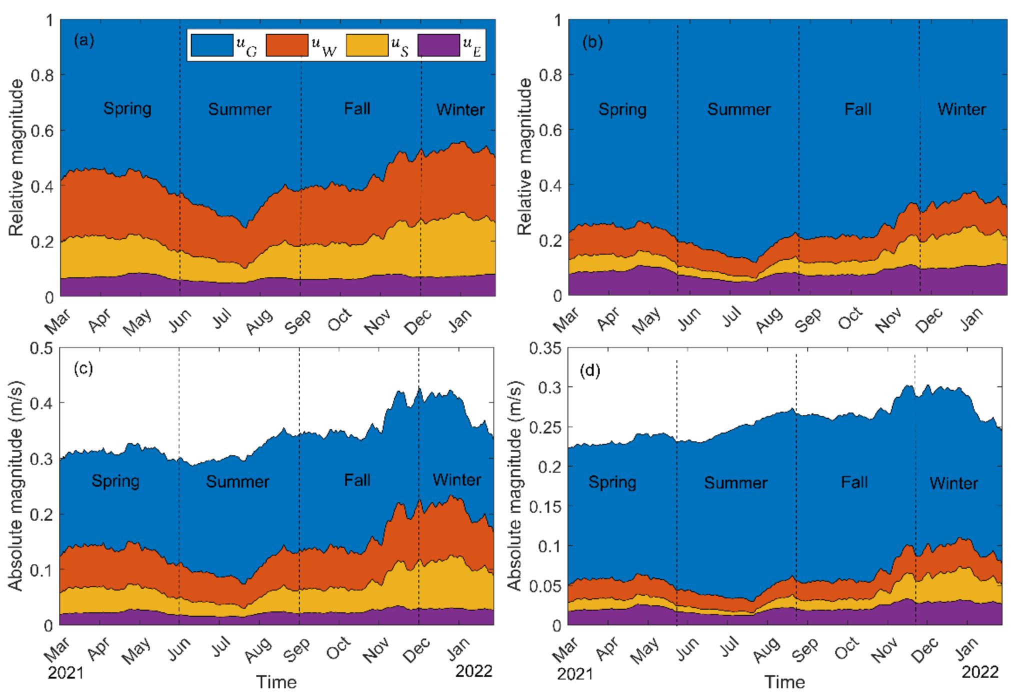

Figure 12. The relative and absolute value of the current components at the surface (**a,c**) and 1.5m- depth (**b,d**) of (u_G-geostrophic current, u_W-wind-driver current, u_S-Stoke current and u_E-Ekman current) from March 2021 to February 2022.

Like the distinct seasonal variations in wave and wind strength and direction, the direct forcings driving surface debris transport also exhibited marked seasonal variability. Figure 12 presents the absolute and relative magnitudes of the forcing components for PTM-DX (Fig. 12a, and c) and PTM-DO (Fig. 12b, and d). For PTM-DX forcings, the geostrophic current was the dominant component year-round, contributing approximately 68% of the total forcing in summer and declining to around 48 % in winter. Among the remaining components, windage and Stokes drift made comparable contributions, both substantially exceeding that of the Ekman current across all seasons. Similarly, for PTM-DO, the geostrophic current remained the primary forcing component, contributing about 83% in summer and decreasing to roughly 65% in winter. The other three components, windage, Stokes drift, and Ekman current, had similar magnitudes, particularly during winter. However, Stokes drift was generally less influential than windage and Ekman current, likely due to its more rapid exponential decay with depth (e^{-2kz}), in contrast to the slower decay of the Ekman current ($e^{-z/d}$). The estimated Ekman depth ranged from approximately 15 m in summer to 30 m in winter, substantially deeper than the depth affected by Stokes drift. Consequently, the absolute magnitude of the Ekman current contribution showed little variation between PTM-DX and PTM-DO.

The PTM results indicate that the optimal current representation for tracking DX drifters is achieved using three components: geostrophic current, Stokes drift, and windage. This combination performed slightly better than the full four-component setup, suggesting potential redundancy or overestimation when the Ekman current is included in modelling surface debris transport. In contrast, the optimal configuration for PTM-DO involved all four components, indicating that at subsurface depths, overlap among wind-driven forcings, such as windage, Stokes drift, and the Ekman current, is reduced, and their combined influence is necessary to achieve the best performance.

4.3 Seasonal variation of particle transport and dispersion

The seasonal variation of atmospheric and oceanic forcings near the air–sea interface, as described in the previous section, plays a key role in determining the fate of floating debris in the EJS. To investigate the seasonal variability in floating debris dispersion and transport driven by surface forcings, a particle tracking model was run using the optimal forcing combination for DX drifters (C7). A total of 576 particles were released at the ocean surface near the southwestern entrance to the EJS, with releases occurring every five days throughout the year (March 2021 to February 2022), and each particle was tracked for five months. Figure 13 presents streamlines based on seasonally averaged velocity fields (Fig. 13a, c, e, and g), along with the corresponding seasonal particle accumulation maps (Fig. 13b, d, f, and h), showing the relative frequency of particle presence within 5 km grid cells. The three red streamlines highlight trajectories passing through the same points along the eastern side of the subpolar front near 40°N.

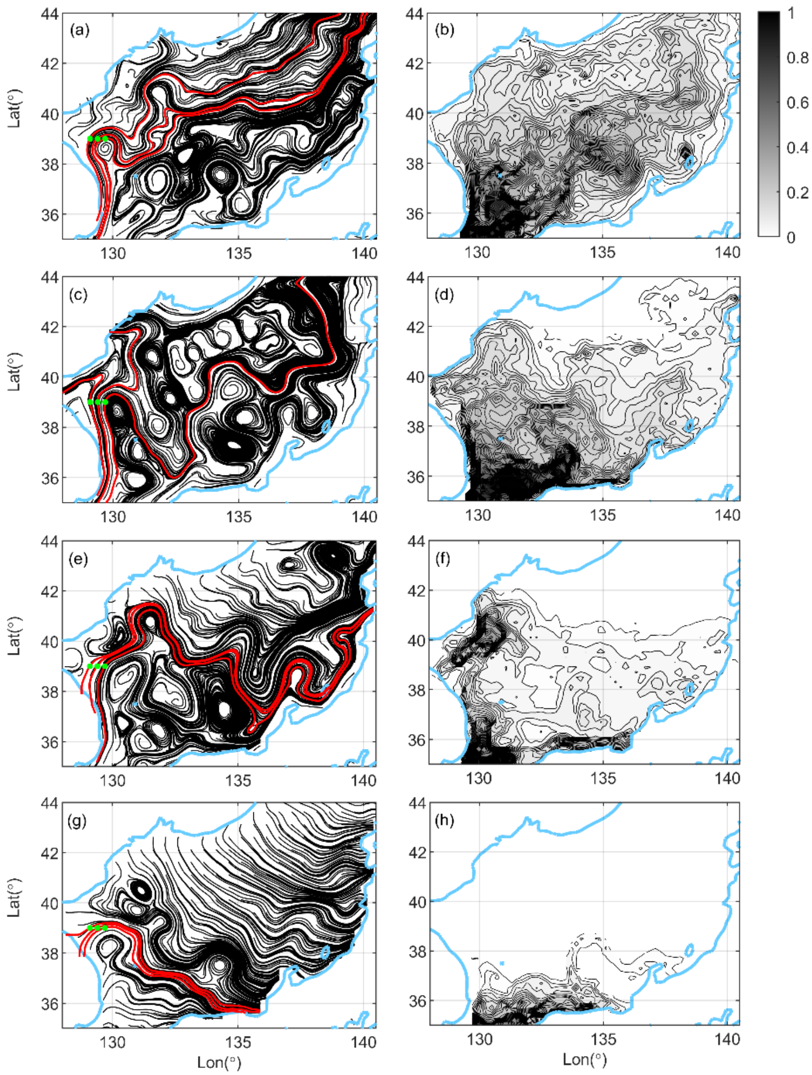

Figure 13. Seasonal streamlines and particle accumulation maps from March 2021 to February 2022, simulated using the optimal forcing combination (C7). Panels (**a, c, e, g**) show streamlines of the seasonally averaged surface current for spring (March–May), summer (June–August), autumn (September–November), and winter (December–February), respectively. Panels (**b, d, f, h**) show the corresponding seasonal particle accumulation maps. Red lines represent streamlines that pass through three fixed points marked in green. Particles were released every five days from March 2021 to February 2022 at the southwestern entrance of the EJS and tracked for five months. The accumulation maps display the relative frequency of particle occurrence, calculated as the number of particle passages through each 5 km grid cell normalized by the maximum frequency.

In spring (Fig. 12a, and b), the streamlines reveal that relatively strong winds blow northward near the Korean Peninsula and shift northeastward, especially in the northern EJS, facilitating material transport along and above the subpolar front. This wind-driven configuration results in the broadest dispersion of floating debris among all seasons. In summer (Fig. 12c, and d), the flow is characterized by eddy-like coherent patterns throughout the EJS, driven by persistent mesoscale circulations under the weakest wind conditions. A branch of the EKWC flows northward along the coast and forms a closed streamline loop in the northern coastal region. This circulation pattern suggests that particles entrained on the western side of the EKWC become trapped and accumulate along the Korean coastline. In fall (Fig. 12e, and f), streamlines originating from the northern coastline extend southeastward across the northern EJS. The red streamlines show minimal variation, indicating relatively slow northward particle movement. This is consistent with the broader, lower-concentration particle distributions observed in the accumulation map. Additionally, the streamlines near the Japanese coastline remain open, allowing debris to continue along the coast. In winter (Fig. 12g, and h), most streamlines appear nearly straight, influenced by strong and consistent west-northwesterly winds and wave propagation in the same direction. As a result, particle trajectories are largely confined to the southern EJS. Given that our drifters were released in mid-November and tracked for several months, the fall and winter transport maps (Fig. 12e, f and Fig. 12g, h) effectively represent the observed fate of drifters that eventually beached along the Japanese coastline.

The seasonal beaching locations of particles are illustrated in Fig. 14, where beaching is defined as particle contact with the coastline. In spring (Fig. 14a), the number of beached particles was the lowest among all seasons, with a substantial portion remaining offshore. This pattern corresponds with the springtime streamline plots, which show predominantly northeastward transport across the EJS and limited streamline closure near the coast. In summer (Fig. 14b), when winds were weakest, the widest spatial distribution of beaching was observed, with particles reaching both the Japanese and Korean coastlines surrounding the EJS. Fall (Fig. 14c) was characterized by concentrated beaching along the southern coasts of both Japan and Korea, with particularly pronounced accumulation along the Japanese coastline. In winter (Fig. 14d), strong northwesterly winds likely contributed to increased beaching intensity along the southern Japanese coast. These seasonal mechanisms align with previous numerical studies: Yoon et al. (2010) highlighted the dominant role of monsoonal winds and windage in driving seasonal peaks of floating debris accumulation along the Japanese coast, while Iwasaki et al. (2017) demonstrated that intensified winter wave conditions and associated Stokes drift significantly enhance the onshore transport of buoyant debris toward Japan.

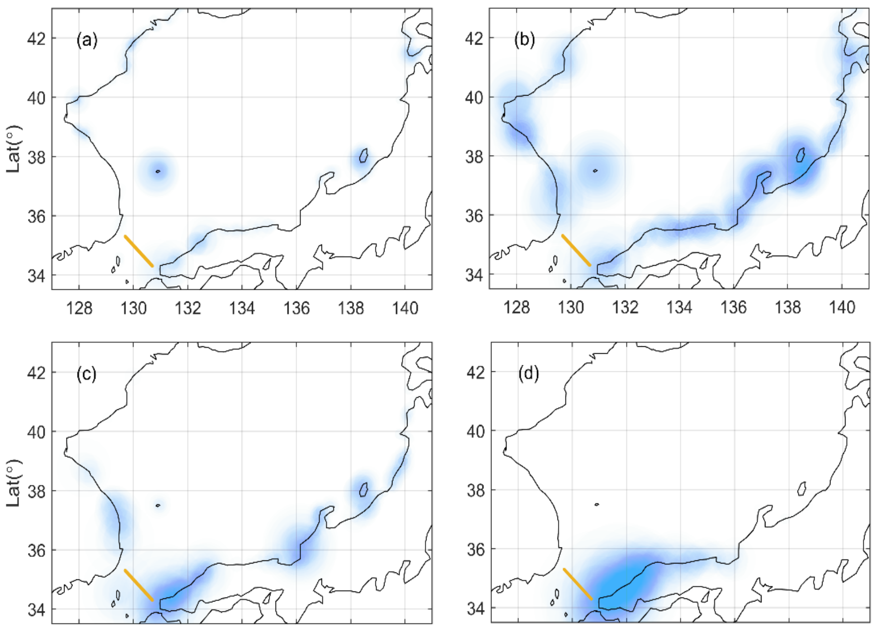

Figure 14. Spatial distribution and relative accumulation intensity of beached particles simulated using the optimal surface forcing (C7) for (a) spring (March–May), (b) summer (June–August), (c) fall (September–November), and (d) winter (December–February). The beached particle locations were determined from the same particle trajectories used in Fig. 13. Beaching is defined as the behavior of particles first contacting the coastline. The particle release location is marked by the yellow line. Color intensity along the coastline indicates the relative density of particle accumulation, with darker shades representing higher accumulation.

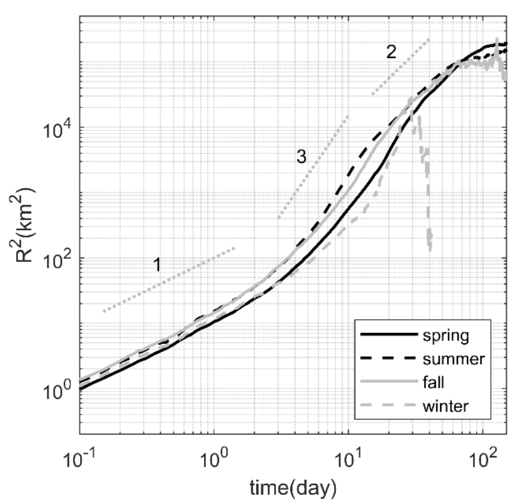

Figure 15. Seasonal variation of relative dispersion, R^2 (t), for particles (same as those used in Fig. 13, and 14) simulated using the optimal forcing combination (C7). Lines indicate relative dispersion for particles released in spring (black solid), summer (black dashed), autumn (gray solid), and winter (gray dashed).

The seasonal variation in relative dispersion can also be interpreted in terms of atmospheric and oceanic forcings (Fig. 15). In all cases, dispersion initially exhibited a brief period of slow growth, attributed to the model's constant diffusivity within grid cells, followed by a more rapid increase consistent with Richardson-like behavior, continuing until approximately 30 days after release. During this phase, particles released in winter showed the lowest relative dispersion, while those released in summer exhibited the highest. The reduced dispersion in winter likely resulted from persistent strong winds and waves that constrained particle motion, leading to concentrated beaching along the southern Japanese coast (Fig. 14d). In contrast, the enhanced dispersion in summer was attributed to weak winds, resulting in reduced wave action, Stokes drift, and Ekman currents, which allow mesoscale eddies to dominate particle transport. This pattern aligns with Fig. 14b, which shows widespread beaching along both the Korean and Japanese coastlines. Over time, relative dispersion in all seasons began to plateau roughly one month after release, as particle pair separations approach the basin scale. These results suggest that strong winds suppress the influence of mesoscale eddies by restructuring the flow into a more uniform, wind-driven (ballistic-like) velocity field, whereas weak winds allow particles to remain entrained within mesoscale eddies, thereby enhancing basin-wide dispersion, especially in marginal seas like the EJS.

5 Conclusions

This study evaluated the near-surface forcing combinations required to reproduce observed drifter trajectories in the East/Japan Sea using a passive particle tracking model driven by prescribed Eulerian velocity fields and a simple random-walk representation of unresolved diffusion. The 2021 drifter experiment revealed a clear cross-basin transport pathway from the Korean coast toward Japan, with the observed trajectories separating near a hyperbolic-type Lagrangian structure.

The comparison between observed and simulated trajectories showed that the optimal forcing combination depends on drifter type and effective sampling depth. For the undrogued DX drifters, the best performance was obtained by combining geostrophic current, Stokes drift, and windage. For the drogued DO drifters, the inclusion of all four components, geostrophic current, Ekman current, Stokes drift, and windage, provided the best agreement with observations. These results indicate that wave-induced drift and direct wind forcing are essential for surface-exposed objects, whereas Ekman current becomes more important for particles with a deeper effective sampling depth.

The optimized data-driven forcing combinations also performed better than the benchmark simulations driven by the GOFS analysis and GLORYS reanalysis in this specific experiment. The FTLE comparison suggests that the reconstructed forcing fields better represented the Lagrangian structure associated with the early drifter bifurcation. This does not imply general superiority over ocean analysis or reanalysis products, but shows that explicitly combining near-surface forcing components at physically relevant depths can improve trajectory prediction for this event.

Seasonal simulations showed that winter winds accelerate eastward transport and enhance beaching along the Japanese coast, whereas weaker summer winds allow mesoscale eddies to broaden particle dispersion and produce more spatially distributed beaching patterns. These results highlight the seasonal control of wind, waves, and mesoscale circulation on near-surface transport in the EJS.

The present PTM should be interpreted as a model of the fluid-dynamical component of near-surface particle transport, not as a complete fate model for specific macroplastic or microplastic debris. Processes such as fragmentation, biofouling- or colonization-induced buoyancy change, aggregation, degradation, vertical mixing, settling, resuspension, and detailed shoreline interaction were not explicitly included. Applications to real plastic debris would therefore require additional particle-specific terms depending on particle size, shape, density, material, buoyancy, and aging. Nevertheless, this study provides a physically constrained basis for improving debris-transport modeling in the EJS and other marginal seas.

Data availability

All datasets and models used in this study are publicly available to support transparency and reproducibility. Geostrophic currents were obtained from the Copernicus Marine Service product SEALEVEL_GLO_PHY_L4_MY_008_047 (https://data.marine.copernicus.eu/product/SEALEVEL_GLO_PHY_L4_MY_008_047/description). Wind velocity at 10 m height was sourced from the ECMWF ERA5 reanalysis provided by ECMWF (https://cds.climate.copernicus.eu/datasets/reanalysis-era5-single-levels?tab=overview). Stokes drift fields were computed using the University of Miami Wave Model (https://github.com/umwm/umwm). GOFS/HYCOM data were obtained from https://www.hycom.org/data/glby0pt08/expt-93pt0, and the GLORYS12V1 reanalysis data used for the CMS benchmark simulations were downloaded from the Copernicus Marine Service product GLOBAL_MULTIYEAR_PHY_001_030. Drifter data in the East/Japan Sea is available at https://drive.google.com/file/d/15IpunKfFTN9H7z2Ww6l_ihqniNy8Rr2M/view?usp=drive_link. All trajectory analyses, and visualizations were conducted using MATLAB R2022a.

Author contributions

JMC initiated the research idea, while HTMT developed the study design and carried out the research under the guidance and scholarly discussions with JMC and YGP. The formal analysis was performed by HTMT in collaboration with JMC. The manuscript was drafted by HTMT and subsequently reviewed and revised by JMC. All authors contributed to the conceptual development and refinement of the study.

Competing interests

The authors declare there are no conflicts of interest for this manuscript

Financial support

This research was supported by the Korea Institute of Marine Science & Technology Promotion (KIMST) funded by the Ministry of Oceans and Fisheries (20220546).

References

Amante, C., & Eakins, B. W. (2009). ETOPO1 Global Relief Model converted to PanMap layer format. *ETOPO1 Global Relief Model converted to PanMap layer format.*, *24*, 19.

Aurell, E., Boffetta, G., Crisanti, A., Paladin, G., & Vulpiani, A. (1996). Predictability in systems with many characteristic times: The case of turbulence. *Physical Review E*, *53*(3), 2337.

Bressan, A. C. (2019). The Deflection Angle of Surface Ocean Currents From the Wind Direction. *Journal of Geophysical Research: Oceans*, *124*(11), 7412–7420. doi: https://doi.org/10.1029/2019JC015454.

Callies, U., Groll, N., Horstmann, J., Kapitza, H., Klein, H., Maßmann, S., & Schwichtenberg, F. (2017). Surface drifters in the German Bight: model validation considering windage and Stokes drift. *Ocean Science*, 13(5), 799-827.

Castellari, S., Griffa, A., Özgökmen, T. M., & Poulain, P. M. (2001). Prediction of particle trajectories in the adriatic sea using Lagrangian data assimilation. *Journal of Marine Systems*, *29*(1–4), 33–50. doi: 10.1016/S0924-7963(01)00008-2.

Chen, F., Zhang, C., Brett, M. T., & Nielsen, J. M. (2020). The importance of the wind-drag coefficient parameterization for hydrodynamic modeling of a large shallow lake. *Ecological Informatics*, *59*, 101106. doi: 10.1016/j.ecoinf.2020.101106.

Chen, G., Chapron, B., Ezraty, R., Vandemark, D., 2002. A global view of swell and wind sea climate in the ocean by satellite altimeter and scatterometer. *J. Atmos. Ocean. Technol*. 19 (11), 1849–1859.

Chenillat, F., Huck, T., Maes, C., Grima, N., & Blanke, B. (2021). Fate of floating plastic debris released along the coasts in a global ocean model. *Marine Pollution Bulletin*, *165*, 112116. doi: 10.1016/j.marpolbul.2021.112116.

Choi, J., Troy, C., Hawley, N., McCormick, M., & Wells, M. (2020). Lateral dispersion of dye and drifters in the center of a very large lake. *Limnology and Oceanography*, 65(2), 336-348.

Clark, B. L., Carneiro, A. P. B., Pearmain, E. J., Rouyer, M. M., Clay, T. A., Cowger, W., Phillips, R. A., Manica, A., Hazin, C., Eriksen, M., González-Solís, J., Adams, J., Albores-Barajas, Y. V., Alfaro-Shigueto, J., Alho, M. S., Araujo, D. T., Arcos, J. M., Arnould, J. P. Y., Barbosa, N. J. P., … Dias, M. P. (2023). Global assessment of marine plastic exposure risk for oceanic birds. *Nature Communications*, *14*(1), 3665. doi: 10.1038/s41467-023-38900-z.

Cole, M., Lindeque, P., Halsband, C., & Galloway, T. S. (2011). Microplastics as contaminants in the marine environment: A review. *Marine Pollution Bulletin*, *62*(12), 2588–2597. doi: 10.1016/j.marpolbul.2011.09.025.

Cózar, A., Echevarría, F., González-Gordillo, J. I., Irigoien, X., Úbeda, B., Hernández-León, S., Palma, Á. T., Navarro, S., García-de-Lomas, J., Ruiz, A., Fernández-de-Puelles, M. L., & Duarte, C. M. (2014). Plastic debris in the open ocean.

Proceedings of the National Academy of Sciences of the United States of America, *111*(28), 10239–10244. doi: 10.1073/pnas.1314705111.

Curcic, M., Chen, S. S., & Özgökmen, T. M. (2016). Hurricane-induced ocean waves and stokes drift and their impacts on surface transport and dispersion in the Gulf of Mexico. *Geophysical Research Letters*, *43*(6), 2773-2781.

Cushman-Roisin, B., & Beckers, J. M. (2011). *Introduction to geophysical fluid dynamics: physical and numerical aspects* (Vol. 101). Academic press.

D'Asaro, E. A., Shcherbina, A. Y., Klymak, J. M., Molemaker, J., Novelli, G., Guigand, C. M., ... & Özgökmen, T. M. (2018). Ocean convergence and the dispersion of flotsam. *Proceedings of the National Academy of Sciences*, 115(6), 1162-1167.

Davis, R. E. (1985). Drifter observations of coastal surface currents during CODE: The method and descriptive view. *Journal of Geophysical Research: Oceans*, *90*(C3), 4741-4755.

de Dominicis, M., Bruciaferri, D., Gerin, R., Pinardi, N., Poulain, P.-M., Garreau, P., Zodiatis, G., Perivoliotis, L., Fazioli, L., Sorgente, R., and Manganiello, C.: A multi-model assessment of the impact of currents, waves and wind in modelling surface drifters and oil spill, *Deep Sea Research Part II*, 133, 21–38, 2016.

Dobler, D., Maes, C., Martinez, E., Rahmania, R., Gautama, B. G., Farhan, A. R., & Dounias, E. (2022). On the Fate of Floating Marine Debris Carried to the Sea through the Main Rivers of Indonesia. *Journal of Marine Science and Engineering*, *10*(8), 1009. doi: 10.3390/jmse10081009.

Ebuchi, N. (1999). Growth of wind waves with fetch in the Sea of Japan under winter monsoon investigated using data from satellite altimeters and scatterometer. *Journal of Oceanography*, *55*(5), 575-584.

Gu, J., Zhang, Y., Tuo, P., Hu, Z., Chen, S., & Hu, J. (2024). Surface floating objects moving from the Pearl River Estuary to Hainan Island: An observational and model study. *Journal of Marine Systems*, *241*. doi: 10.1016/j.jmarsys.2023.103917.

Haller, G. (2001). Lagrangian structures and the rate of strain in a partition of two-dimensional turbulence. *Physics of Fluids*, *13*(11), 3365-3385.

Haller, G. (2015). Lagrangian coherent structures. *Annual Review of Fluid Mechanics*, 47(1), 137–162. https://doi.org/10.1146/annurev-fluid-010313-141322

Haller, G., and Yuan, G. (2000). Lagrangian coherent structures and mixing in two-dimensional turbulence. *Physica D: Nonlinear Phenomena*, 147(3-4), 352–370. https://doi.org/10.1016/S0167-2789(00)00142-1

Haza, A. C., Paldor, N., Özgökmen, T. M., Curcic, M., Chen, S. S., & Jacobs, G. (2019). Wind-Based Estimations of Ocean Surface Currents From Massive Clusters of Drifters in the Gulf of Mexico. *Journal of Geophysical Research: Oceans*, *124*(8), 5844–5869. doi: 10.1029/2018JC014813.

Hersbach, H., Bell, B., Berrisford, P., Hirahara, S., Horányi, A., Muñoz-Sabater, J., ... & Thépaut, J. N. (2020). The ERA5 global reanalysis. *Quarterly journal of the royal meteorological society*, *146*(730), 1999-2049.

Hsu, P. C., Centurioni, L., Shao, H. J., Zheng, Q., Lu, C. Y., Hsu, T. W., & Tseng, R. S. (2021). Surface current variations and oceanic fronts in the southern East China Sea: Drifter experiments, coastal radar applications, and satellite observations. *Journal of Geophysical Research: Oceans*, 126(10), e2021JC017373.

Huang, G., Zhan, H., He, Q., Wei, X., & Li, B. (2021). A Lagrangian study of the near-surface intrusion of Pacific water into the South China Sea. *Acta Oceanologica Sinica*, *40*(7), 15–30. doi: 10.1007/s13131-021-1766-6.

Ichiye, T. (1984). Some problems of circulation and hydrography of the Japan Sea and the Tsushima Current. In *Elsevier oceanography series* (Vol. 39, pp. 15-54). Elsevier.

Irfan, T., Isobe, A., & Matsuura, H. (2024). A particle tracking model approach to determine the dispersal of riverine plastic debris released into the Indian Ocean. *Marine Pollution Bulletin*, *199*, 115985. doi: 10.1016/j.marpolbul.2023.115985.

Isobe, A., Hinata, H., Kako, S. I., & Yoshioka, S. (2011). Formulation of leeway-drift velocities for sea-surface drifting-objects based on a wind-wave flume experiment. *Interdisciplinary studies on environmental chemistry-marine environmental modeling and analysis. Terrapub., Tokyo*, 239-249.

Isobe, A., Uchida, K., Tokai, T., & Iwasaki, S. (2015). East Asian seas: A hot spot of pelagic microplastics. *Marine Pollution Bulletin*, *101*(2), 618–623. doi: 10.1016/j.marpolbul.2015.10.042.

Iwasaki, S., Isobe, A., Kako, S., Uchida, K., & Tokai, T. (2017). Fate of microplastics and mesoplastics carried by surface currents and wind waves: A numerical model approach in the Sea of Japan. *Marine Pollution Bulletin*, *121*(1–2), 85–96. doi: 10.1016/j.marpolbul.2017.05.057.

Jalón-Rojas, I., Wang, X. H., & Fredj, E. (2019). A 3D numerical model to Track Marine Plastic Debris (TrackMPD): Sensitivity of microplastic trajectories and fates to particle dynamical properties and physical processes. *Marine Pollution Bulletin*, *141*, 256–272. doi: 10.1016/j.marpolbul.2019.02.052.

Jeon, C., Park, J.-H., Varlamov, S. M., Yoon, J.-H., Kim, Y. H., Seo, S., Park, Y.-G., Min, H. S., Lee, J. H., & Kim, C.-H. (2014). Seasonal variation of semidiurnal internal tides in the East/Japan Sea. *Journal of Geophysical Research: Oceans*, *119*(5), 2843– 2859. doi: doi:10.1002/2014JC009864.

Kim, J. C., Yu, D. H., Sim, J. E., Son, Y. T., Bang, K. Y., & Shin, S. (2023). Validation of OpenDrift-Based Drifter Trajectory Prediction Technique for Maritime Search and Rescue. *Journal of Ocean Engineering and Technology*, *37*(4), 145–157. doi: 10.26748/KSOE.2023.018.

Kim, K., Kim, K. R., Min, D. H., Volkov, Y., Yoon, J. H., & Takematsu, M. (2001). Warming and structural changes in the East (Japan) Sea: a clue to future changes in global oceans?. *Geophysical Research Letters*, *28*(17), 3293-3296.

Kim, K., Tran, H. T. M., Song, K. M., Son, Y. B., Park, Y. G., Ryu, J. H., ... & Choi, J. M. (2024). Near-Surface Dispersion and Current Observations Using Dye, Drifters, and HF Radar in Coastal Waters. *Remote Sensing*, 16(11), 1985.

Kim, Y. R., Kang, D. W., Lee, S., Choi, K. Y., Kim, H. E., Jung, J. M., ... & Kim, C. J. (2021). Distribution and assessment of heavy metal concentrations in the East Sea-Byeong ocean dumping site, Korea. *Marine Pollution Bulletin*, *172*, 112815.

Kuroda, M., Isobe, A., Uchida, K., Tokai, T., Kitakado, T., Yoshitake, M., Miyamoto, Y., Mukai, T., Imai, K., Shimizu, K., Yagi, M., Mituhasi, T., & Habano, A. (2024). Abundance and potential sources of floating polystyrene foam macro- and microplastics around Japan. *Science of the Total Environment*, *925*(November 2023), 171421. doi: 10.1016/j.scitotenv.2024.171421.

LaCasce, J. (2008). Statistics from Lagrangian observations. *Progress in Oceanography*, *77*(1), 1-29, doi:10.1016/j.pocean.2008.02.002.

Lebreton, L. (2022). The status and fate of oceanic garbage patches. *Nature Reviews Earth & Environment*, *3*(11), 730–732. doi: https://doi.org/10.1038/s43017-022-00363-z.

Lebreton, L. C. M., Greer, S. D., & Borrero, J. C. (2012). Numerical modelling of floating debris in the world's oceans. *Marine Pollution Bulletin*, *64*(3), 653–661. doi: 10.1016/j.marpolbul.2011.10.027.

Lee, Dong Kyu, & Niiler, P. (2010). Eddies in the southwestern East/Japan Sea. *Deep-Sea Research Part I: Oceanographic Research Papers*, *57*(10), 1233–1242. doi: 10.1016/j.dsr.2010.06.002.

Liang, J. H., Liu, J., Benfield, M., Justic, D., Holstein, D., Liu, B., Hetland, R., Kobashi, D., Dong, C., & Dong, W. (2021). Including the effects of subsurface currents on buoyant particles in Lagrangian particle tracking models: Model development and its application to the study of riverborne plastics over the Louisiana/Texas shelf. *Ocean Modelling*, *167*(August), 101879. doi: 10.1016/j.ocemod.2021.101879.

Liu, Y., Weisberg, R. H., Vignudelli, S., & Mitchum, G. T. (2014). Evaluation of altimetry-derived surface current products using Lagrangian drifter trajectories in the eastern Gulf of Mexico. *Journal of Geophysical Research: Oceans*, *119*(5), 2827–2842. doi: 10.1002/2013JC009710.

Liu, Yonggang, & Weisberg, R. H. (2011). Evaluation of trajectory modeling in different dynamic regions using normalized cumulative Lagrangian separation. *Journal of Geophysical Research: Oceans*, *116*(C9). doi: 10.1029/2010JC006837.

Liubartseva, S., Coppini, G., Lecci, R., & Clementi, E. (2018). Tracking plastics in the Mediterranean: 2D Lagrangian model. *Marine Pollution Bulletin*, *129*(1), 151–162. doi: 10.1016/j.marpolbul.2018.02.019.

Lumpkin, R., Özgökmen, T., & Centurioni, L. (2017). Advances in the application of surface drifters. *Annual review of marine science*, 9, 59-81.

Mao, Y., & Heron, M. L. (2008). The influence of fetch on the response of surface currents to wind studies by HF ocean surface radar. *Journal of Physical Oceanography*, *38*(5), 1107–1121. doi: 10.1175/2007JPO3709.1.

Mariano, A. J., Kourafalou, V. H., Srinivasan, A., Kang, H., Halliwell, G. R., Ryan, E. H., & Roffer, M. (2011). On the modeling of the 2010 Gulf of Mexico Oil Spill. *Dynamics of Atmospheres and Oceans*, *52*(1–2), 322–340. doi: 10.1016/j.dynatmoce.2011.06.001.

Maximenko, N., Hafner, J., & Niiler, P. (2012). Pathways of marine debris derived from trajectories of Lagrangian drifters. *Marine Pollution Bulletin*, *65*(1–3), 51–62. doi: 10.1016/j.marpolbul.2011.04.016.

McCaffrey, L., & Koeberle, A. L. (2024). An economical open-source Lagrangian drifter design to measure deep currents in lakes. Water Resources Research, 60(10), e2024WR037429.

McWilliams, J. C. (2016). Submesoscale currents in the ocean. *Proceedings of the Royal Society A: Mathematical, Physical and Engineering Sciences*, *472*(2189), 20160117. doi: 10.1098/rspa.2016.0117.

Medina-Rubio, J., Nussbaum, M., van den Bremer, T. S., & van Sebille, E. (2026). Using surface drifters to characterise near-surface ocean dynamics in the southern North Sea: a data-driven approach. *Ocean Science*, 22(1), 49-74.

Nakakuni, M., Nishida, M., Nishibata, R., Kishimoto, K., Yamaguchi, H., Ichimi, K., Ishizuka, M., Suenaga, Y., & Tada, K. (2024). Convergence zones of coastal waters as hotspots for floating microplastic accumulation. *Marine Pollution Bulletin*, *206*(June), 116691. doi: 10.1016/j.marpolbul.2024.116691.

Niiler, P. P., & Paduan, J. D. (1996). Wind-driven motions in the northeast Pacific as measured by Lagrangian drifters. *Oceanographic Literature Review*, *7*(43), 646.

Novelli, G., Guigand, C. M., Cousin, C., Ryan, E. H., Laxague, N. J., Dai, H., ... & Özgökmen, T. M. (2017). A biodegradable surface drifter for ocean sampling on a massive scale. *Journal of Atmospheric and Oceanic Technology*, *34*(11), 2509-2532.

Okubo, A. (1971, August). Oceanic diffusion diagrams. In *Deep sea research and oceanographic abstracts* (Vol. 18, No. 8, pp. 789-802). Elsevier. https://doi.org/10.1016/0011-7471(71)90046-5.

Onink, V., Kaandorp, M. L., van Sebille, E., & Laufkötter, C. (2022). Influence of particle size and fragmentation on large-scale microplastic transport in the Mediterranean Sea. *Environmental science & technology*, *56*(22), 15528-15540. https://doi.org/10.1021/acs.est.2c03363

Onink, V., Wichmann, D., Delandmeter, P., & van Sebille, E. (2019). The Role of Ekman Currents, Geostrophy, and Stokes Drift in the Accumulation of Floating Microplastic. *Journal of Geophysical Research: Oceans*, *124*(3), 1474–1490. doi: 10.1029/2018JC014547.

Ono, J., Ohshima, K. I., Uchimoto, K., Ebuchi, N., Mitsudera, H., & Yamaguchi, H. (2013). Particle-tracking simulation for the drift/diffusion of spilled oils in the Sea of Okhotsk with a three-dimensional, high-resolution model. *Journal of Oceanography*, *69*(4), 413–428. doi: 10.1007/s10872-013-0182-8.

Park, K. A., Chung, J. Y., Kim, K., & Cornillon, P. C. (2005). Wind and bathymetric forcing of the annual sea surface temperature signal in the East (Japan) Sea. *Geophysical Research Letters*, *32*(5).

Park, Y.-G., & Seo, S. (2021). Review on Lagrangian Particle Tracking Modeling for Floating Objects around the Korean Peninsula. *KMI International Journal of Maritime Affairs and Fisheries*, *13*(2), 67–83. doi: 10.54007/ijmaf.2021.13.2.67.

Pärn, O., Davulienė, L., Moy, D. M., Vahter, K., Stips, A., & Torsvik, T. (2023). Effects of Eulerian current, Stokes drift and wind while simulating surface drifter trajectories in the Baltic Sea. *Oceanologia*, *65*(3), 453-465.

Paul, S., Nath, S., Bhattacharjee, S., & Mukherjee, S. (2024). Unveiling the effects of microplastics pollution on marine fauna. *Blue Biotechnology 2024 1:1*, *1*(1), 6. doi: 10.1186/s44315-024-00006-6.

Pinheiro, H. T., MacDonald, C., Santos, R. G., Ali, R., Bobat, A., Cresswell, B. J., Francini-Filho, R., Freitas, R., Galbraith, G. F., Musembi, P., Phelps, T. A., Quimbayo, J. P., Quiros, T. E. A. L., Shepherd, B., Stefanoudis, P. V., Talma, S., Teixeira, J. B., Woodall, L. C., & Rocha, L. A. (2023). Plastic pollution on the world's coral reefs. *Nature*, *619*(7969), 311–316. doi: 10.1038/s41586-023-06113-5.

Poje, A. C., Özgökmen, T. M., Lipphardt Jr, B. L., Haus, B. K., Ryan, E. H., Haza, A. C., ... & Mariano, A. J. (2014). Submesoscale dispersion in the vicinity of the Deepwater Horizon spill. Proceedings of the National Academy of Sciences, 111(35), 12693-12698.

Poulain, P. M., & Gerin, R. (2019). Assessment of the water-following capabilities of CODE drifters based on direct relative flow measurements. *Journal of Atmospheric and Oceanic Technology*, *36*(4), 621-633.

Poulain, P. M., Centurioni, L., & Özgökmen, T. (2022). Comparing the currents measured by CARTHE, CODE and SVP drifters as a function of wind and wave conditions in the southwestern Mediterranean Sea. *Sensors*, *22*(1), 353.

Prants, S. V., Budyansky, M. V., Ponomarev, V. I., & Uleysky, M. Y. (2011). Lagrangian study of transport and mixing in a mesoscale eddy street. *Ocean Modelling*, *38*(1–2), 114–125. doi: 10.1016/j.ocemod.2011.02.008.

Röhrs, J., Christensen, K. H., Hole, L. R., Broström, G., Drivdal, M., & Sundby, S. (2012). Observation-based evaluation of surface wave effects on currents and trajectory forecasts. *Ocean Dynamics*, *62*(10), 1519-1533.

Röhrs, J., Sutherland, G., Jeans, G., Bedington, M., Sperrevik, A. K., Dagestad, K. F., ... & LaCasce, J. H. (2023). Surface currents in operational oceanography: Key applications, mechanisms, and methods. Journal of Operational Oceanography, 16(1), 60-88.

Rypina, Irina I., Getscher, T. R., Pratt, L. J., & Mourre, B. (2021). Observing and Quantifying Ocean Flow Properties Using Drifters with Drogues at Different Depths. *Journal of Physical Oceanography*, *51*(8), 2463–2482. doi: 10.1175/JPO-D-20-0291.1.

Saeedi, M. (2024). How microplastics interact with food chain: a short overview of fate and impacts. *Journal of Food Science and Technology*, *61*(3), 403–413. doi: 10.1007/s13197-023-05720-4.

Santos de Moura, M. & Vianna, M. (2020). A new threat: assessing the main interactions between marine fish and plastic debris from a scientometric perspective. *Reviews in Fish Biology and Fisheries*, *30*(4), 623–636.

Sebille, E. van, Aliani, S., Law, K. L., Maximenko, N., Alsina, J. M., Bagaev, A., Bergmann, M., Chapron, B., Chubarenko, Cózar, I., Andrés, Delandmeter, P., Egger, M., Fox-Kemper, B., Garaba, S. P., Oddijn-Murphy, L., Hardesty, B. D., Matthew

J Hoffman17, A. I., Cleo E Jongedijk19, Mikael L A Kaandorp1 , Liliya Khatmullina6, A. A. K., … Giuseppe Suaria2 , Martin Thiel34, 35, 36, T. S. van den B. and D. W. (2020). The physical oceanography of the transport of floating marine debris. *Environmental Research Letters*, *15*(2), 023003. Retrieved from http://dx.doi.org/10.1088/1748-9326/ab6d7d.

Seo, S., Park, Y. G., & Kim, K. (2020). Tracking flood debris using satellite-derived ocean color and particle-tracking modeling. *Marine Pollution Bulletin*, *161*(PA), 111828. doi: 10.1016/j.marpolbul.2020.111828.

Shadden, S. C., Lekien, F., and Marsden, J. E. (2005). Definition and properties of Lagrangian coherent structures from finite-time Lyapunov exponents in two-dimensional aperiodic flows. *Physica D: Nonlinear Phenomena*, 212, 271–304. https://doi.org/10.1016/j.physd.2005.10.007

Sotillo, M. G., Garcia-Ladona, E., Orfila, A., Rodríguez-Rubio, P., Maraver, J. C., Conti, D., ... & Álvarez-Fanjul, E. (2016). The MEDESS-GIB database: tracking the Atlantic water inflow. *Earth System Science Data*, 8(1), 141-149.

Sotillo, M. G., Garcia-Ladona, E., Orfila, A., Rodríguez-Rubio, P., Maraver, J. C., Conti, D., ... & Álvarez-Fanjul, E. (2016). The MEDESS-GIB database: tracking the Atlantic water inflow. *Earth System Science Data*, *8*(1), 141-149.

Sudre, J., Maes, C., & Garçon, V. (2013). On the global estimates of geostrophic and Ekman surface currents. *Limnology and Oceanography: Fluids and Environments*, *3*(1), 1–20. doi: 10.1215/21573689-2071927.

Sun, Z., Hu, J., Lin, H., Chen, Z., Zhu, J., Yang, L., ... & Wu, X. (2022). Lagrangian observation of the Kuroshio current by surface drifters in 2019. *Journal of Marine Science and Engineering*, 10(8), 1027.

Takeda, H., & Isobe, A. (2024). Quantification of ocean microplastic fragmentation processes in the Sea of Japan using a combination of field observations and numerical particle tracking model experiments. *Marine Pollution Bulletin*, *208*, 117032.

Talley, L.D., D.-H. Min, V.B. Lobanov, V.A. Luchin, V.I. Ponomarev, A.N. Salyuk, A.Y Shcherbina, P.Y. Tishchenko, and I. Zhabin. 2006. Japan/East Sea water masses and their relation to the sea's circulation. *Oceanography* 19(3):32–49, https://doi.org/10.5670/oceanog.2006.42.

Tamtare, T., Dumont, D., & Chavanne, C. (2022). The Stokes drift in ocean surface drift prediction. *Journal of Operational Oceanography*, *15*(3), 156–168. doi: 10.1080/1755876X.2021.1872229.

Tekman, M. B., Walther, B. A., Peter, C., Gutow, L., & Bergmann, M. (2022). Impacts of Plastic Pollution in the Oceans on Marine Species, Biodiversity and Ecosystems Summary of a Study for Wwf By Summary of a Study for Wwf By Wwf International 2022 3 Summary. *Alfred-Wegener-Institut*. doi: 10.5281/zenodo.5898684.

Thiel, M., Luna-Jorquera, G., Álvarez-Varas, R., Gallardo, C., Hinojosa, I. A., Luna, N., Miranda-Urbina, D., Morales, N., Ory, N., Pacheco, A. S., Portflitt-Toro, M., & Zavalaga, C. (2018). Impacts of marine plastic pollution from continental coasts to subtropical gyres-fish, seabirds, and other vertebrates in the SE Pacific. *Frontiers in Marine Science*, *5*(July), 238. doi: 10.3389/fmars.2018.00238.

van der Mheen, M., Pattiaratchi, C., Cosoli, S., & Wandres, M. (2020). Depth-Dependent Correction for Wind-Driven Drift Current in Particle Tracking Applications, *Frontiers in Marine Science, 7, 305*.

Woo, H. J., & Park, K. A. (2017). Long-term trend of satellite-observed significant wave height and impact on ecosystem in the East/Japan Sea. *Deep Sea Research Part II: Topical Studies in Oceanography*, 143, 1-14.

Wu, J. (1982). Wind-stress coefficients over sea surface from breeze to hurricane. *Journal of Geophysical Research: Oceans*, *87*(C12), 9704–9706. doi: 10.1029/jc087ic12p09704.

Yoon, J. H., Kawano, S., & Igawa, S. (2010). Modeling of marine litter drift and beaching in the Japan Sea. *Marine pollution bulletin*, 60(3), 448-463.

Data-Driven Enhancement of Ocean Surface Forcing for Accurate Floating Debris Transport Modelling in the East/Japan Sea

Hong T. M. Tran[1], Young G. Park[2], Jun M. Choi[3*]

[1]Fluid Mechanics Department, Faculty of Civil Engineering, Ho Chi Minh City University of Technology, Vietnam National University Ho Chi Minh City, Ho Chi Minh City, 700000, Vietnam
[2]Ocean Circulation and Climate Research Center, Korea Institute of Ocean Science and Technology, Busan, 49111, Republic of Korea
[3]Department of Ocean Engineering, College of Environment and Marine Sciences and Technology, Pukyong National University, Busan, 48513, Republic of Korea

Correspondence to: Jun M. Choi (jmchoi@pknu.ac.kr)

Abstract. Floating debris transport in marginal seas is controlled by a combination of geostrophic currents, wind-driven currents, wave-induced drift, and direct wind forcing, but the relative importance of these processes remains difficult to quantify without in-situ trajectory observations. This study evaluates near-surface forcing combinations for particle tracking in the East/Japan Sea using 33 GPS-tracked surface drifters deployed off the Korean coast in November 2021. The drifters revealed a clear cross-basin transport pathway toward the Japanese coastline and an early bifurcation near a hyperbolic-type Lagrangian structure. We used a particle tracking model to test combinations of geostrophic current, Ekman current, Stokes drift, and windage against the observed drifter trajectories using MAE and NCLS metrics. For undrogued DX drifters, the best performance was obtained by combining geostrophic current, Stokes drift, and windage. For drogued DO drifters, which sampled a deeper effective depth, the inclusion of all four forcing components provided the best agreement with observations. The optimized forcing combinations outperformed benchmark simulations driven by the GOFS analysis and GLORYS reanalysis in this specific event, primarily because they better reproduced the Lagrangian structure associated with the early trajectory bifurcation. Seasonal simulations showed that winter winds enhance eastward transport and beaching along Japan, whereas weaker summer winds allow mesoscale eddies to broaden particle dispersion. The present framework represents the fluid-dynamical component of near-surface particle transport and does not explicitly include plastic-specific fate processes such as fragmentation, biofouling-induced buoyancy changes, aggregation, settling, or resuspension.

1 Introduction

Millions of tons of plastic debris enter the ocean annually, posing a significant threat to marine ecosystems and human health. This debris accumulates in eddies and gyres (Lebreton, 2022; Maximenko et al., 2012; Thiel et al., 2018), washes ashore on coastlines (Chenillat et al., 2021; Cole et al., 2011; Cózar et al., 2014; Dobler et al., 2022; Nakakuni et al., 2024), and fragments into smaller pieces that disperse widely over time. These fragments pose serious risks to marine life through ingestion, particularly for species with vast foraging and migration ranges (Clark et al., 2023; Santos de Moura et al., 2020). Because plastic debris can facilitate disease transmission, damage critical habitats like coral reefs (Pinheiro et al., 2023), impact human health (Paul et al., 2024), disrupt food chains (Saeedi, 2024), and alter ecosystem dynamics (Tekman et al., 2022), accurate modeling to track the trajectories, distributions, and accumulation of floating plastic debris is urgently needed.

Particle Tracking Models (PTMs) have been widely implemented to model the transport and fate of floating materials (Lebreton et al., 2012; Onink et al., 2019). Such models have also been extended to study plastic debris dispersion in rivers discharging into the Indian Ocean (Irfan et al., 2024). Within marginal seas, PTM applications include tracking floating particle trajectories influenced by subsurface currents in the Gulf of Mexico (Liang et al., 2021), modeling oil particle pathways following the Deepwater Horizon oil spill (Mariano et al., 2011), tracking plastics in the Mediterranean Sea using surface currents and Stokes drift (Liubartseva et al., 2018), predicting particle trajectories in the Adriatic Sea (Castellari et al., 2001), simulating oil spill diffusion in the Sea of Okhotsk (Ono et al., 2013), and predicting surface debris movement in the East/Japan Sea (EJS) (Iwasaki et al., 2017).

PTMs are typically driven by Eulerian surface currents, which are heavily influenced by a combination of geostrophic currents, Ekman transport, Stokes drift, and windage (Röhrs et al., 2023; Sebille et al., 2020). Geostrophic currents, resulting from the balance between the Coriolis force and horizontal pressure gradients (Sudre et al., 2013), play a fundamental role in long-term ocean circulation and influence both surface and subsurface flows globally. Wind directly affects floating objects by exerting force on their exposed surface area, known as windage, often quantified by wind drift factors ranging from 0 to 5% of the wind speed (Gu et al., 2024; Tamtare et al., 2022). Ekman transport, driven by wind stress and the Coriolis effect, generates a vertical current profile within the upper ocean layers (Bressan, 2019) and has been linked to microplastic accumulation in subtropical regions (Onink et al., 2019). Stokes drift is a wave-induced Lagrangian drift that adds to the Eulerian surface current and therefore contributes directly to the transport of floating objects (Mao and Heron, 2008; Tamtare et al., 2022). Consequently, a systematic study determining which physical processes dominate particle movement is crucial for model accuracy.

Drifter experiments are an essential tool for evaluating PTM results that simulate the transport and dispersion of floating plastic debris and the corresponding physical processes on the ocean surface. In open oceans, validation is often supported by massive datasets such as the Global Drifter Program, which maintains thousands of drifters globally (Lumpkin et al., 2017; Maximenko et al., 2012). With the exception of the massive CODE-type drifter experiment in the Gulf of Mexico (Poje et al., 2014; D'Asaro et al., 2018), drifter experiments in marginal seas are typically constrained in scale, often relying on a small number of drifters to investigate local transport features. For instance, recent studies in the North Sea used only 6 to 12 drifters to validate surface transport models (Callies et al., 2017; Medina-Rubio et al., 2026), and similar process-oriented studies in the East China Sea were conducted with as few as 4 to 29 SVP-type drifters (Hsu et al., 2021; Sun et al., 2022). Sotillo et al. (2016) compiled a CODE-type drifter dataset in the Strait of Gibraltar to validate ocean models and track contaminants. The primary role of these experiments is to validate the surface currents that directly affect the accuracy of the debris tracking model. However, many tracking model studies in marginal seas still lack validation with in-situ drift data, or employ drifter types that are not suitable for tracking floating debris. Here, we utilized 33 surface drifters deployed simultaneously, tracking currents at a depth of 0.3 m. Although this number is smaller than open-ocean campaigns, it represents one of the largest synoptic datasets conducted in a marginal sea and constitutes the largest surface drifter experiment conducted in the EJS.

We investigate transport and dispersion in the EJS using PTMs validated with drifter experiments. The EJS, a marginal sea approximately 1,000 km wide, is a recognized "hot spot" for microplastic accumulation (Isobe et al., 2015; Kuroda et al., 2024) and is often described as a "miniature ocean" due to its encapsulation of major global oceanic processes, such as deep water formation, thermohaline circulation, and mesoscale eddy activity, within a relatively small and semi-enclosed basin (e.g., Ichiye, 1984; Kim et al., 2001; Talley et al., 2006). Bordered by the Korean Peninsula, Japan, and the Russian Far East, the EJS receives a mix of natural and anthropogenic materials, including plastic debris, transported by ocean currents such as the Tsushima Warm Current, a branch of the Kuroshio Current flowing from the East China Sea, as well as by wind (Park et al., 2021). Although the transport and distribution of plastic debris in the EJS have been studied (Iwasaki et al., 2017; Kim et al., 2021; Takeda and Isobe, 2024), there remains a lack of observational data in this marginal sea to validate particle trajectories and the specific physical processes influencing near-surface particle movement in the region.

In this study, we aimed to optimize the near-surface forcings that govern floating debris transport using a PTM validated with in-situ surface drifter observations. Here, "floating debris transport" refers to the fluid-dynamical transport component represented by passive particles moving near the ocean surface rather than the complete fate of specific macroplastic or microplastic particles. A drifter experiment was conducted to trace near-surface transport and assess the accuracy of simulated particle trajectories. In the results section, we identify the optimal combinations of key surface forcing components - geostrophic currents, Stokes drift, Ekman currents, and windage - for accurately modeling floating debris transport. By incorporating these forcings into the PTM, we simulated particle trajectories and compared them with observed drifter paths. Particle-specific processes such as fragmentation, biofouling-induced buoyancy change, aggregation, settling, and resuspension were not included in the present framework. This simplification is appropriate for the present objective because the simulated transport time scale is less than three months, whereas fragmentation has been reported to act on much longer, decadal time scales and to have little influence on large-scale microplastic transport over periods shorter than three years (Onink et al., 2022). In the discussion section, we evaluate the performance of the optimized forcing combinations relative to ocean analysis/reanalysis velocity products and further apply these combinations to estimate the seasonal variability of surface transport and beaching patterns of floating debris in the EJS.

2 Materials and Methods

2.1 Drifter experiment

Custom-made cylindrical drifters (Fig. 1a) were used to observe near-surface currents by tracking their movements in the EJS. The drifters, equipped with GPS trackers, were designed to collect location data at 5-minute intervals over several months. Each drifter measured 30 cm in height and 9 cm in diameter, with the top 3–5 cm protruding above the water surface when deployed. A total of 33 drifters were deployed, consisting of 23 undrogued drifters (hereafter referred to as DX drifters) and 10 drogued drifters (hereafter referred to as DO drifters). The drogue for the DO drifters consisted of two 30 cm × 30 cm plastic plates arranged perpendicularly and positioned at a depth of 2 m. By using surface drifters with slightly different depths, we aimed to investigate near-surface transport processes relevant to floating marine debris. Drifter positions were tracked from deployment until either beaching occurred or the signal was lost. The mean, minimum, maximum, and standard deviation of drifter lifetimes were 48.05, 12.2, 79.7, and 22.4 days, respectively. The location data were interpolated at 15-minute intervals and used for subsequent analysis. The DX and DO drifters were used to sample near-surface transport, but they were expected to respond differently to wind forcing. The DX drifter had a small part exposed above the sea surface, so it could be more affected by direct wind forcing and Stokes drift (Niiler et al., 1996; Röhrs et al., 2012).

In contrast, the DO drifter included a 30 × 30 cm drogue centered near 2 m depth to increase submerged drag and reduce direct wind slippage, following the general water-following principle of drogued surface drifters such as CODE and CARTHE drifters (Davis, 1985; Novelli et al., 2017). CARTHE drifters sample the upper approximately 0.6 m with wind-induced slip less than 0.5% of the 10 m wind speed, whereas CODE drifters sample the upper meter with reported downwind slip of about 0.1% of the wind speed (Poulain and Gerin, 2019; Poulain et al., 2022). Thus, the DX and DO drifters are treated here as custom observational benchmarks with different effective depths and windage sensitivities, rather than as exact equivalents of CODE or CARTHE drifters.

We deployed the drifters across the East Korea Warm Current (EKWC) region in the EJS (Fig. 1). The circulation along the eastern Korean Peninsula is primarily influenced by the northward-flowing EKWC and the southward-flowing North Korean Cold Current (NKCC), both of which are modulated by coastal currents, mesoscale eddies, and frontal structures (Lee et al., 2010). These flow systems generate complex near-surface transport pathways as drifters interact with regional oceanographic features (Prants et al., 2011; Onink et al., 2019). The drifters were released at six deployment locations near the Korean coast, with four DX drifters and either one or two DO drifters released at each location. The deployment started on 10 November 2021 at 01:40 UTC, and the subsequent groups were released at intervals over approximately 3 h. The one-week-averaged geostrophic current and 10-m wind velocity fields after drifter release are shown in Fig. 1c, together with the initial drifter location (black line). During this period, a strong northward geostrophic current was present along the Korean coast, while the 10-m wind field was predominantly eastward to northeastward over the deployment region. The corresponding one-week-averaged sea surface temperature (SST) and sea surface height (SSH) fields are shown in Fig. 1d, indicating mesoscale variability and frontal structures in the EJS. In particular, the mesoscale eddy evident near the drifter release locations likely influenced the subsequent pathways and final fates of the drifters.

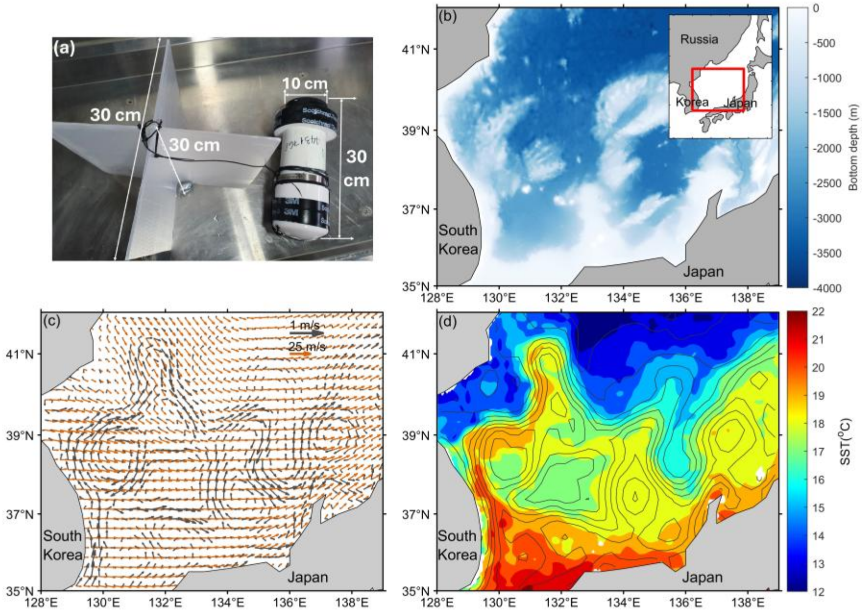

Figure 1. (a) Photograph and dimensions of the undrogued DX and drogued DO drifters. (b) Bathymetry of the East/Japan Sea, with the inset showing the surrounding geographic region. (c) Geostrophic current vectors (black) and 10-m wind velocity vectors (orange), both averaged over the first week after drifter release. The East Korea Warm Current (EKWC) is indicated in blue, and the reference vectors are shown in the upper-right corner. (d) Sea surface temperature (SST; color shading) and sea surface height (SSH; contour lines), both averaged over the first week after drifter release. Thick black lines indicate the initial drifter deployment locations.

2.2 Current data sets

Four current components were considered to be associated with the movement of drifters: geostrophic current (Sudre et al., 2013; Tamtare et al., 2022), Ekman current (Sudre et al., 2013; Huang et al., 2021), Stokes drift (Curcic et al. 2016; Iwasaki et al. 2017; Pärn et al. 2023), and windage (Gu et al., 2024). Geostrophic current ($\vec{u}_G$ or G), representing the background horizontal velocities, was obtained from the SEALEVEL_GLO_PHY_L4_MY_008_047 dataset. This dataset is a Copernicus Marine SEALEVEL Level-4 altimeter product processed by the CNES/CLS DUACS system. It combines multi-mission satellite altimeter observations, including Sentinel-6A, Sentinel-3A/B, Jason-3, SARAL/AltiKa, CryoSat-2, OSTM/Jason-2, Jason-1, TOPEX/Poseidon, Envisat, GFO, ERS-1/2, and Haiyang-2A/B. The current version of the product provides daily global ocean observations at a nominal spatial resolution of 0.125° and a temporal resolution of 1 day. For the particle-tracking calculations, the velocity fields were processed on the originally prepared computational grid with a grid spacing of approximately 0.25°, corresponding to about 25 km in the EJS. Wind velocity at 10 m above the sea surface ($\vec{u}_{10}$) was obtained from the ECMWF Reanalysis v5 (ERA5) dataset, with a spatial resolution of 1/4° and a temporal resolution of 1 hour. The wind data were converted to wind stress using the bulk formula ($\vec{\tau} = \rho_a C_d \vec{u}_{10} |\vec{u}_{10}|$), where ρ_a is the air density, and $C_d(=$

$10^{-3}(0.8 + 0.065|\vec{u}_{10}|)$) is the drag coefficient (Chen et al., 2020; Wu, 1982; Cushman-Roisin et al., 2011; Rypina et al., 2021).

The windage velocity, $\vec{u}_W$, was parameterized as $\vec{u}_W = r\vec{u}_{10}$, where r is the windage coefficient and $\mathbf{u}_{10}$ is the wind velocity at 10 m height. The coefficient r was estimated using a first-order balance between aerodynamic drag on the exposed part of the drifter and hydrodynamic drag on the submerged part:

$$r = \sqrt{\rho_a C_{d,a} A_a / \rho_w C_{d,w} A_w}, \quad (1)$$

where ρ_a and ρ_w are the densities of air and seawater, $C_{d,a}$ and $C_{d,w}$ are the drag coefficients in air and water, and A_a and A_w are the projected areas above and below the sea surface, respectively (Isobe et al., 2011). Because $C_{d,a}$ and $C_{d,w}$ were not measured directly for the custom drifters, we first assumed $C_{d,a}/C_{d,w} \approx 1$ as a geometry-based first-order approximation, consistent with previous studies (de Dominicis et al., 2016; van der Mheen et al., 2020). This assumption is appropriate for the DX drifters because the exposed and submerged parts are both cylindrical. For the DO drifters, however, the submerged flat drogue plate likely has a larger drag coefficient than the cylindrical float. Therefore, the assumption $C_{d,a}/C_{d,w} \approx 1$ should be interpreted as a conservative upper-bound estimate of windage rather than as a calibrated drag-coefficient ratio.

For the DX drifter, the cylindrical body had a diameter of 0.09 m and a height of 0.30 m, with approximately 0.03–0.05 m protruding above the sea surface. Thus, the exposed projected area was $A_a \approx 0.09 \times (0.03\text{–}0.05) = 0.0027\text{–}0.0045\ \mathrm{m}^2$, whereas the submerged projected area was $A_w \approx 0.09 \times (0.25\text{–}0.27) = 0.0225\text{–}0.0243\ \mathrm{m}^2$. Using $\rho_a/\rho_w \approx 1.2 \times 10^{-3}$ and $C_{d,a}/C_{d,w} \approx 1$, the estimated windage coefficient is $r_{DX} \approx 0.012\text{–}0.016$. Accordingly, $r = 0.015$ was adopted for the DX drifters.

For the DO drifter, the exposed area above the sea surface was similar to that of the DX drifter, but the submerged drag area was much larger because of the 0.30×0.30 m drogue plate positioned near 2 m depth. To avoid double-counting the two perpendicular plates, one effective projected drogue plate area was used: $A_{w,\mathrm{drogue}} = 0.30 \times 0.30 = 0.09\ \mathrm{m}^2$. The submerged cylindrical body contributed $A_{w,\mathrm{body}} \approx 0.09 \times 0.26 = 0.0234\ \mathrm{m}^2$. Thus, the total effective submerged projected area was $A_w \approx 0.0234 + 0.09 = 0.1134\ \mathrm{m}^2$. Using $C_{d,a}/C_{d,w} \approx 1$, this gives $r_{DO} \approx 0.0053\text{–}0.0069$. The adopted value $r = 0.005$ is therefore a conservative geometry-based estimate for the DO drifters.

As an additional check, we considered published drag coefficients used in drifter drag-area calculations. McCaffrey and Koeberle (2024) used $C_D = 0.74$ for cylindrical float elements and $C_D = 1.98$ for flat-plate drogue elements. Applying these values to the DO geometry gives $r_{DO} = \left[\rho_a(0.74A_a)/\rho_w\left(0.74A_{w,\mathrm{body}} + 1.98A_{w,\mathrm{drogue}}\right)\right]^{1/2}$, which yields $r_{DO} \approx 0.0035\text{–}0.0045$. This value is slightly lower than, but close to, the adopted $r = 0.005$. Therefore, $r = 0.005$ does not underestimate the direct wind effect on the DO drifters; rather, it provides a physically reasonable and slightly conservative estimate. The windage coefficients used in this study were not empirically tuned to optimize trajectory skill, but were selected a priori from the drifter geometry and published drag-coefficient ranges.

Stokes drift ($\vec{u}_S$ or S) was calculated using the University of Miami Wave Model, version 1.0.1 (UMWM), over the domain 125°E-135°E, 25°N-35°N, with a horizontal resolution of 0.0083° and 22 depth levels. The model was forced with daily wind data from ECMWF/ERA5 and ETOPO1 (Hersbach et al., 2020; Amante et al., 2009) bathymetry and coastline data. The three-dimensional Stokes drift fields were determined using the following equation:

$$\overrightarrow{u_s}(z) = \int_0^{2\pi}\int_0^{\infty} \omega k^2 \frac{cosh[2k(d+z)]}{2sinh^2 kd} F(f) dk d\theta \tag{2}$$

, where ω, k, d, z, θ, and F are the angular frequency, wave number, mean water depth, the depth below the surface at which the Stokes drift is evaluated, the wave direction, and wavenumber variance spectrum, respectively (Haza et al., 2019). The computation was performed for the period from November 10, 2021, to January 30, 2022. Significant wave height and Stokes drift data were saved daily during the computation period. The Ekman transport ($\vec{u}_E$ or E) was calculated using the following equations:

$$u_E = \frac{\sqrt{2}}{\rho f d} e^{\frac{z}{d}} \left[\tau_x cos\left(\frac{z}{d} - \frac{\pi}{4}\right) - \tau_y sin\left(\frac{z}{d} - \frac{\pi}{4}\right)\right] \tag{3}$$

$$v_E = \frac{\sqrt{2}}{\rho f d} e^{\frac{z}{d}} \left[\tau_x sin\left(\frac{z}{d} - \frac{\pi}{4}\right) - \tau_y cos\left(\frac{z}{d} - \frac{\pi}{4}\right)\right] \tag{4}$$

, where the Ekman layer depth $d = \alpha|\vec{u}_{10}|/(\sin(\phi))^{0.5}$, ρ is the water density, ϕ is the latitude, $\alpha = 3.2(s)$ is an empirical scaling coefficient, and z is water depth (Rypina et al., 2021).

Furthermore, two model-derived surface velocity products were introduced for the benchmark comparison presented later in the discussion section. The first product was the GLORYS12V1 global ocean reanalysis distributed by Copernicus Marine (GLOBAL_MULTIYEAR_PHY_001_030), which provides daily mean fields at $1/12°$ horizontal resolution. The second product was the Global Ocean Forecast System (GOFS) analysis based on HYCOM/NCODA. These analysis/reanalysis velocity fields were used only as benchmark surface velocity products for comparison with the reconstructed forcing combinations. The sea surface temperature (SST) field from GLORYS12V1 was also used to describe the background thermal structure in the EJS.

2.3 The particle tracking model

The particle tracking model (PTM) used in this study treats the simulated particles as passive near-surface drifters advected by prescribed Eulerian velocity fields. The model does not explicitly represent plastic-specific processes such as fragmentation, biofouling-induced buoyancy change, settling, resuspension, or beaching. Instead, the PTM was used to evaluate the accuracy of different combinations of surface forcing components by comparing simulated particle trajectories with observed drifter trajectories. From a given horizontal velocity field, the particle displacement was estimated using a deterministic advection component and a stochastic diffusion component represented by a simple random walk scheme:

$$\vec{x}(t+\Delta t) - \vec{x}(t) = \vec{u}\Delta t + R\sqrt{2K_h\Delta t} \tag{5}$$

where $\vec{x}$ is the position vector of a Lagrangian particle, Δt is the time step in the PTM, set to 1800 s in this study, R is a random number drawn from a normal distribution at each time step, and K_h is the horizontal diffusion coefficient estimated using the

Smagorinsky scheme (Irfan et al., 2024; Jalón-Rojas et al., 2019; Seo et al., 2020). The stochastic term was included to account for unresolved subgrid-scale dispersion that is not represented by the prescribed Eulerian velocity fields.

The total drift velocity, $\vec{u}$, was determined by a linear combination of the physical processes described in Sect. 2.2:

$$\vec{u} = \vec{u}_G + \vec{u}_S + \vec{u}_E + \vec{u}_W \tag{6}$$

where $\vec{u}_G$, $\vec{u}_S$, $\vec{u}_E$, and $\vec{u}_W$ ($= r\vec{u}_{10}$) represent the geostrophic current (G), Stokes drift (S), Ekman current (E), and windage (W), respectively. These forcings were obtained from the datasets described in Sect. 2.2. Thus, the primary focus of this study was to construct and evaluate data-driven Eulerian velocity combinations representing specific near-surface transport processes, including geostrophic current, Stokes drift, Ekman current, and windage. Model-derived velocity products were tested separately as benchmark comparisons. Tidal currents were neglected in this study because they are relatively weak in the EJS (Jeon et al., 2014), and our result, not shown here, confirmed that tidal forcing had a negligible effect on particle trajectories in the region. Therefore, particle motion in the PTM is governed by prescribed Eulerian velocity fields, and the stochastic diffusion term is calculated using the Smagorinsky scheme based on the same Eulerian velocity fields.

Two sets of PTM simulations were conducted using the eight forcing combinations described in Table 1: PTM-DX, representing the undrogued DX drifters, and PTM-DO, representing the drogued DO drifters. For PTM-DX, near-surface forcings were used. Specifically, the Stokes drift was sampled from the shallowest available subsurface level of the wave-model output, approximately $z = -0.1$ m, while the Ekman current was evaluated near the surface. This depth is more representative of the effective submerged depth of the DX drifter than a strict air–sea interface value, because most of the cylindrical body was submerged within the upper 0.25–0.27 m of the water column. For PTM-DO, the Stokes drift and Ekman current were sampled at an effective depth of $z = -1.5$ m. This depth was estimated from the area-weighted hydrodynamic centroid of the submerged cylindrical body and drogue. The submerged cylindrical body had a projected area of approximately $0.09 \times 0.26 = 0.0234$ m^2, with its centroid near 0.13 m depth, whereas the effective projected area of one 0.30×0.30 m drogue plate was 0.09 m^2, centered near 2.0 m depth. The resulting area-weighted centroid was approximately 1.6 m below the sea surface. Thus, $z = -1.5$ m provides a reasonable effective sampling depth for representing the combined hydrodynamic response of the surface float and the submerged drogue. To evaluate the optimal forcing combination, one particle was released from each drifter's initial location, and each simulation was run for 79 days, corresponding to the longest observed drifter track.

Table 1. Forcing-component combinations used in the particle tracking model (PTM) simulations. The columns indicate the four velocity components: u_G (geostrophic current), u_E (Ekman current), u_S (Stokes drift), and u_W (ru_{10}). Circles (○) indicate that the component was included, whereas crosses (×) indicate that it was excluded. C1 represents the geostrophic-only reference case; C2–C4 represent two-component forcing cases; C5–C7 represent three-component forcing cases; and C8 represents the four-component forcing case. These combinations were used to simulate particle trajectories for comparison with the observed DX (undrogued) and DO (drogued) drifters. For PTM-DX, near-surface forcing components were used. For PTM-DO, the Ekman current and Stokes drift were sampled at an effective depth of 1.5 m to represent the deeper hydrodynamic response of the drogued drifters.

#	u_G	u_E	u_S	u_W
C1	○	×	×	×
C2	○	○	×	×
C3	○	×	○	×
C4	○	×	×	○
C5	○	○	○	×
C6	○	○	×	○
C7	○	×	○	○
C8	○	○	○	○

2.4 Evaluation of the particle trajectory

The particle trajectories calculated from the PTM were compared with observed drifter trajectories to determine the optimal combination of forcing components representing near-surface currents. The Mean Absolute Error (MAE), and the Normalized Cumulative Lagrangian separation (NCLS) (Kim et al., 2023) were used as metric to quantify the difference between particle and drifter trajectories. The equation for the MAE is given by,

$$MAE = \frac{1}{N}\sum_{i=1}^{N}(|\Delta Lon| + |\Delta Lat|) \tag{7}$$

where ΔLon and ΔLat are the differences between longitude and latitude of the observed and predicted trajectories. N is the number of the dataset (Kim et al., 2023). The longitude and latitude differences were first converted into physical distances (km) before calculating the MAE. Lower MAE values indicate more precise forecasts and better overall performance.

The NCLS is defined as the cumulative summation of the separation distance between the particle and drifter trajectories, weighted by the length of the drifter trajectories accumulated in time, as follow:

$$NCLS = \begin{cases} 1 - \frac{s}{n} & (NCLS \leq n) \\ 0 & (NCLS > n) \end{cases} \tag{8}$$

, where s $(= \sum_{i=1}^{N} D_i / \sum_{i=1}^{N} L_{o,i})$ denotes the normalized cumulative separation and n is a dimensionless value representing the allowed threshold. This study adopted a value of n = 1, consistent with the approach used by Kim et al., (2023), Liu et al., (2011) and Liu et al., (2014). D_i is the separation distance between drifter and particle trajectories at time step I, $L_{o,i}$ is the cumulative length of the observed trajectories at time step i. Thus, MAE and NCLS are the dimensional and nondimensional metrics, respectively, that measure the cumulative error between the simulated particle and observed drifter trajectories. NCLS values closer to 1 (with a range of 0 to 1) indicate a more accurate simulation.

2.5 Lagrangian diagnostics

The dispersion of observed drifters and simulated particles was quantified using two pair-based metrics: the relative dispersion ($R^2(t)$) and the Finite-Scale Lyapunov Exponent (FSLE). The relative dispersion indicates the growth in size of the drifter cluster relative to its center of mass as given by

$$R^2(t) = \frac{1}{N}\sum_{i=1}^{N}[x_i(t) - x_{cm}(t)]^2 \tag{9}$$

, where N is the number of drifters, $x_i(t)$ is the position vector of the i-th drifter at time t, and $x_{cm}(t)$ is the position vector of the center of mass of the drifter cluster at time t (LaCasce, 2008). For the relative-dispersion analysis, only drifter pairs with an initial separation distance of less than 200 m were retained. The corresponding dispersion coefficient (K) was estimated as

$$K = \frac{1}{4}\frac{\sigma_r^2}{t} \tag{10}$$

, where σ_r^2 represents the horizontal radial variance of the drifter or particle distribution. It is calculated from the mean squared distance of the particles from the center of mass of the cloud and can be interpreted as the spreading scale of an equivalent radially symmetric distribution. Thus, σ_r^2 quantifies the radial spreading of the drifter or particle cloud and was used to estimate the horizontal dispersion coefficient (Okubo, 1971; LaCasce, 2008). Different scaling regimes of $R^2(t)$ with time indicate different dispersion processes e.g., $R^2(t) \sim t$ for diffusive dispersion, $R^2(t) \sim t^3$ for Richardson dispersion, which correspond to $K \sim L^0$ and $K \sim L^{4/3}$, respectively, where L is $3\sigma_r$ represents the size of the particle cluster.

In addition to relative dispersion, the FSLE was also calculated to characterize the dispersion process. The FSLE (λ), measures the average rate of separation of initially nearby particles over a finite distance. It is calculated by tracking pairs of particles and measuring the time it takes for their separation to grow from an initial separation distance, δ_0, to a final separation distance, δ_f:

$$\lambda = \frac{1}{\langle \Delta t \rangle} ln\left(\frac{\delta_f}{\delta_0}\right) \tag{11}$$

, where Δt is the time required for the pair separation to grow from the initial separation scale δ_0 to the final separation scale δ_f, and the angle brackets $\langle\rangle$ denote an average over all particle pairs (Aurell et al., 1996). In this study, the final separation distance was defined as $\delta_f = 2\delta_0$. Therefore, the FSLE plotted as a function of separation distance δ represents the growth rate from $\delta_0 = \delta$ to $\delta_f = 2\delta$. A larger FSLE value indicates a faster rate of separation and thus stronger strain rate. Like the relative dispersion, difference scaling regimes of FSLE with respect to separation distance δ reveal different dispersion processes: $\lambda \sim \delta^{-1}$ for ballistic dispersion ($R^2(t) \sim t^2$), $\lambda \sim \delta^{-1/2}$ for Richardson-like dispersion ($R^2(t) \sim t^3$), and $\lambda \sim \delta^{-2}$ for diffusive dispersion ($R^2(t) \sim t$) (McWilliams, 2016).

The finite-time Lyapunov exponent (FTLE) was used to identify Lagrangian transport structures in the velocity fields. The FTLE quantifies the finite-time separation rate of initially neighboring particles and is defined as

$$\sigma_T(\vec{x}_0) = \frac{1}{|T|} ln\sqrt{\lambda_{max}(C)}, \tag{12}$$

where $\vec{x}_0$ is the initial particle position vector, T is the integration time, C is the Cauchy–Green strain tensor, and $\lambda_{\max}(\mathrm{C})$ is the largest eigenvalue of C (Haller and Yuan, 2000; Shadden et al., 2005; Haller, 2015). The Cauchy–Green strain tensor is given by

$$C = \left[\nabla\vec{F}_{t_0}^{t_0+T}(\vec{x}_0)\right]^T\left[\nabla\vec{F}_{t_0}^{t_0+T}(\vec{x}_0)\right], \tag{13}$$

where $\vec{F}_{t_0}^{t_0+T}(\vec{x}_0)$ is the flow map that gives the particle position at time $t_0 + T$ from the initial position $\vec{x}_0$ at time t_0. Ridges of the FTLE field have been widely used as indicators of Lagrangian coherent structures that organize material transport and mixing (Haller and Yuan, 2000; Shadden et al., 2005; Haller, 2015). In particular, repelling FTLE ridges are associated with material lines from which neighboring particles separate, whereas attracting FTLE ridges are associated with material lines toward which neighboring particles converge (Haller, 2001; Shadden et al., 2005). A finite-time hyperbolic region can be identified near the intersection of attracting and repelling ridges, where particles converge toward the attracting manifold and subsequently diverge along the repelling manifold (Haller and Yuan, 2000; Shadden et al., 2005). Such a saddle-type Lagrangian structure represents a dynamically important transport barrier and can explain the bifurcation of drifter trajectories.

3 Results

3.1 Drifter trajectory

All analyzed drifters deployed near the Korean coast, except those that stopped transmitting before beaching, ultimately reached the Japanese mainland or nearby islands within 13 - 68 days, while eight drifters stopped before beaching after 6–79 days (Table 2). Figure 2a shows the trajectories and final positions of the undrogued DX and drogued DO drifters. Within a few days after deployment, the drifters began diverging into two distinct pathways. One group, comprising 60% of the DO drifters and 27% of the DX drifters, moved northward along the eastern coast of Korea, likely influenced by the strong East Korea Warm Current (EKWC). The other group, consisting of 40% of the DO drifters and 73% of the DX drifters, drifted eastward toward the Japanese coast, primarily driven by prevailing westerly winds. The drifter bifurcation was further examined using FTLE structures derived from the geostrophic velocity field (Fig. 2b). The signed FTLE field shows that the bifurcation occurred near 130°E, 37.4°N, where attracting and repelling FTLE ridges are closely organized. In this representation, red ridges indicate attracting Lagrangian structures, whereas blue ridges indicate repelling Lagrangian structures (Fig. 2b). The observed drifters approached this region from the south to southwest and then separated into two branches, one moving northwestward and the other moving southeastward. This behavior is consistent with a finite-time hyperbolic-type bifurcation region, where particles converge toward an attracting manifold and subsequently diverge along a repelling manifold. This region was located near 130°E, 37.4°N, corresponding to the observed divergence of the drifter trajectories. The mean speeds of the DO and DX drifters were calculated as 0.28 m/s and 0.31 m/s, respectively.

Table 2. Summary of the final fate and drifting duration of observed drifters. The table lists the number and percentage of drifters in each fate category, the corresponding drifting-duration range, and the final fate.

Final fate	Number of drifters	Day from the release (day)
Stopped before beaching	8 (24%)	6-79
Beached at the mainland coastline	19 (57%)	24-68
Beached at the Nisinoshima island	2 (6%)	13
Beached at the Okinoshima island	3 (9%)	13-25
Beached at the Sado island	1 (3%)	45

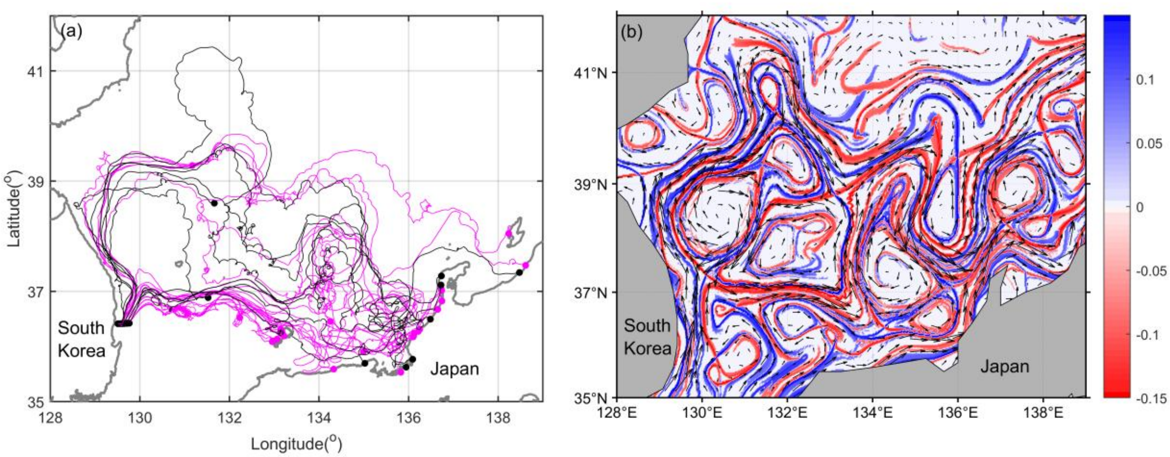

Figure 2. (**a**) Observed trajectories of undrogued DX drifters (black lines) and drogued DO drifters (magenta lines). Thick black lines indicate the initial deployment locations, and filled circles denote the final positions of drifters that remained at sea. (**b**) Signed Finite-time Lyapunov exponent (FTLE) field computed from the geostrophic velocity averaged over the first week after drifter release. Black arrows indicate the geostrophic velocity vectors. In the signed FTLE representation, blue and red ridges indicate repelling and attracting Lagrangian structures, respectively.

3.2 Drifter dispersion

The time evolution of the relative dispersion, $D^2(t)$ (Eq. 9), and the dispersion coefficient, $K(L)$ (Eq. 10), for the drifters is illustrated in Fig. 3. At very early times (t < 0.3 days) and small length scales ($L < 1\ km$), the drifter cluster exhibited diffusive dispersion ($D^2 \sim t^1$). Beyond this initial stage, Richardson dispersion ($D^2 \sim t^3$, or equivalently, $K^2 \sim L^{4/3}$), was evident in the range of approximately 0.3 to 30 days, corresponding to length scales from $L = 1\ km$ to $100\ km$. During $0 < t < 3$ (or $L < 60\ km$), the DO drifters showed slightly greater dispersion than DX drifters, which was possibility attributed to the different passages determined at the hyperbolic region. The majority of DO drifters followed passage along the EKWC near the Korean coastline, where horizontal shear in the coastal current can enhance the dispersion. In contrast, the majority of DX drifters moved offshore, where the transport was dominated by spatially uniform wind in a narrow directional range, resulting in relatively weaker dispersion during the time. However, after approximately 3 days, as the DX drifters moved farther offshore, interactions with mesoscale eddies in the westerly downwind regions enhanced their dispersion, leading to super-Richardson behavior and causing their relative dispersion to exceed that of the DO drifters.

The estimated dispersion coefficients for all drifters were approximately 1, 20, and 1,000 m^2/s at scales of 1, 10, and 100 km, respectively, eventually saturating around 2,000 m^2/s in the EJS. The dispersion coefficient at the early stage was comparable to previous dye and drifter experiments in various waters, including coastal regions, inland waters, and open oceans (Okubo, 1971; Choi et al., 2020; Kim et al., 2024). For scales of 1–100 km, the growth in dispersion followed trends observed in open oceans, and the coefficient saturated when the length scale of the drifter cloud reached approximately 1/10 of the basin scale of the EJS (~2,000 km).

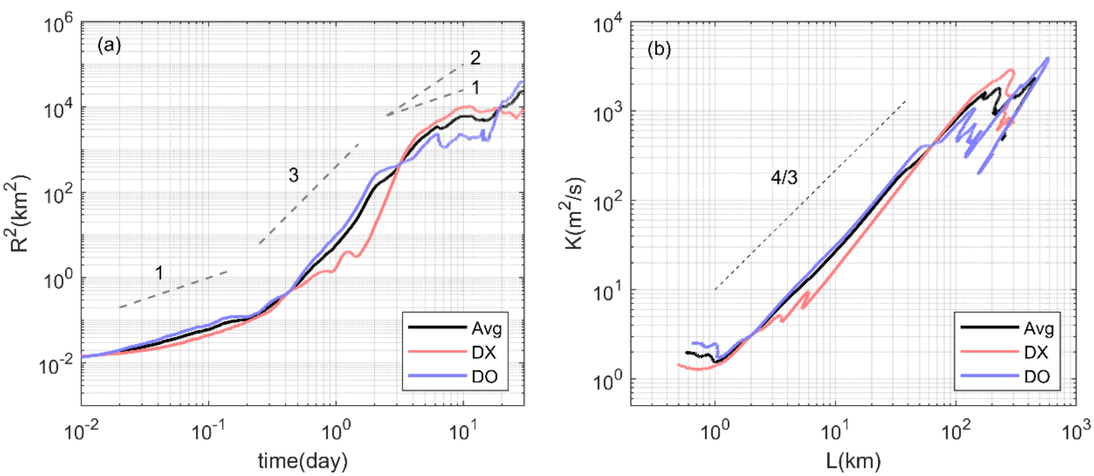

Figure 3. Relative dispersion ($R(t)^2$) (a) and dispersion coefficient ($K(L)$) (b) of the observed drifters. Panel (**a**) shows the time evolution of relative dispersion ($R(t)^2$), and panel (**b**) shows the dispersion coefficient ($K(L)$) as a function of length scale. The red line represents the undrogued (DX) drifters, the blue line represents the drogued (DO) drifters, and the black line indicates the average dispersion of all drifters (both DX and DO).

The FSLE values and trends for both DX and DO drifters were generally similar, but the FSLE values for DO drifters were slightly higher, particularly at very early times at spatial scales on the order of 10 meters and between 0.5 and 50 km. This pattern aligns with the dispersion coefficient K shown in Fig. 3b, where K is also larger for DO drifters over these scales. The difference in FSLE between DO and DX drifters is likely due to their distinct pathways delineated by the hyperbolic-type bifurcation region, consistent with observations from the relative dispersion analysis. The FSLE curves reveal distinct dynamical regimes across spatial scales. In the small-scale regime ($\delta < 0.5\ km$), DX drifters exhibit a slope close to -1, indicative of ballistic dispersion, possibly associated with well-aligned wind-induced transport. In the submeso- and mesoscale-range ($1\ km < \delta < 50\ km$), the slope for DX drifters becomes slightly gentler, and FSLE values remain lower than those of DO drifters. For DO drifters, the FSLE initially shows a steep slope near -2 at small scales ($\delta < 0.5\ km$), characteristic of a diffusive regime, then transitions to a slope of approximately -1/2 to -2/3, reflecting Richardson-like dispersion (Fig. 4). This behavior is consistent with the influence of coastal currents and mesoscale eddy interactions in the region. At larger scales (beyond ~150 km), both DX and DO drifters show a steepening of FSLE values again, corresponding to the scale of mesoscale eddies in the EJS.

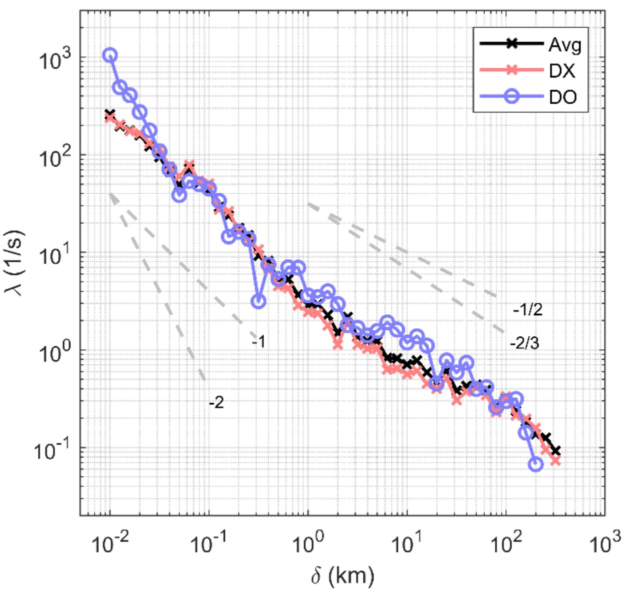

Figure 4. Finite-Size Lyapunov Exponent (FSLE), λ, as a function of separation distance, δ, for the observed drifters. The black line represents the average of all drifters, the red line represents the undrogued (DX) drifters, and the blue line represents the drogued (DO) drifters. The dashed gray lines indicate reference slopes of -2, -1, -1/2, and -2/3.

3.3 Particle trajectory

The performance of the forcing combinations detailed in Fig. 1 was evaluated by qualitatively comparing the observed drifter trajectories with simulated particle trajectories at two different depths: DX drifters were compared with PTM-DX particles driven by surface forcings (Fig. 5), while DO drifters were compared with PTM-DO particles driven by subsurface forcings at 1.5 m depth (Fig. 6). For the PTM-DX particles, increasing the number of forcing components improved the model's ability to replicate the bifurcation of drifter trajectories at the hyperbolic region, particularly when windage was included (Fig. 5f–h).

When simulations were driven solely by geostrophic currents (Fig. 5a), all particles drifted predominantly northward along the EKWC, ultimately accumulating in a mesoscale eddy centered near 132°E, 41°N. The addition of Ekman currents (Fig. 5b) did not result in significant differences. However, including Stokes drift (Fig. 5c) reduced the residence time of particles within the eddy and redirected them toward the Japanese coast. In all simulations without windage, particles remained confined along the EKWC, whereas simulations incorporating windage produced more realistic trajectories that aligned with observed DX drifter paths, which split into both coastal and offshore passages. For PTM-DO particles (Fig. 6), all forcing combinations resulted in transport along the EKWC. The variation among trajectories was less pronounced than for PTM-DX, indicating a stronger influence of the coastal current. Although none of the PTM-DO simulations captured the bifurcation at the hyperbolic-type bifurcation region, the simulation including all four components, geostrophic currents, Ekman currents, Stokes drift, and windage (Fig. 6h), most closely reproduced the observed DO drifter trajectories.

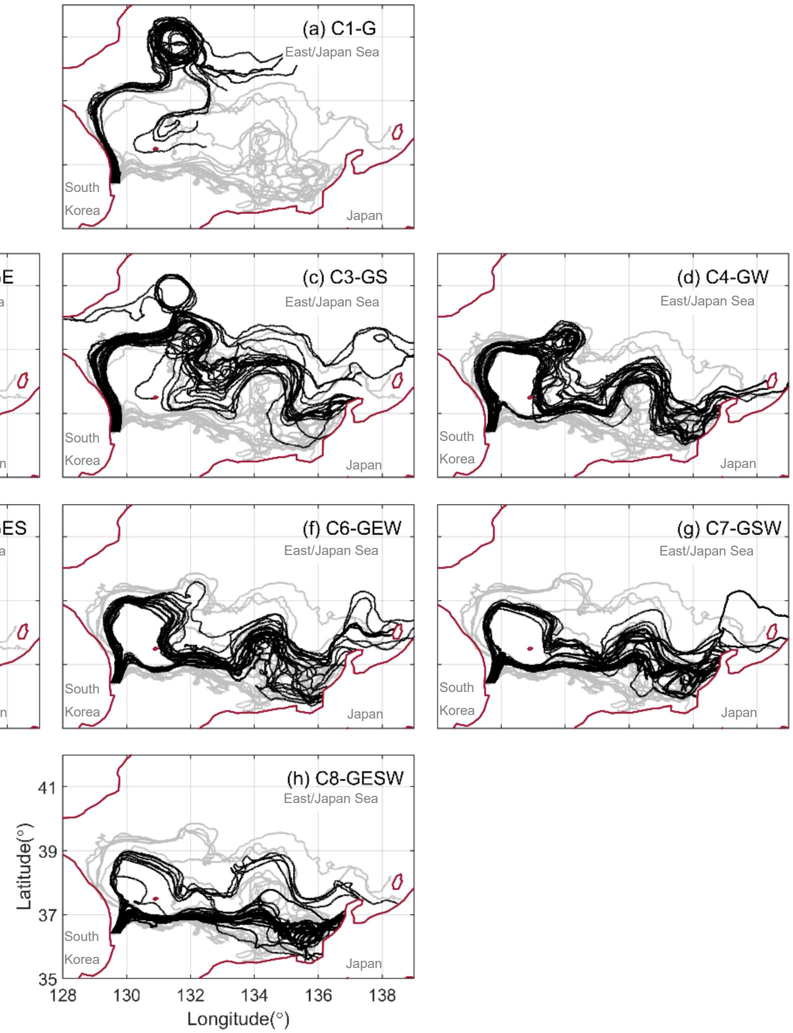

Figure 5. Particle trajectories using surface forcings (PTM-DX) simulated for 3 months. Panels (a-h) correspond to current combinations C1-C8 as described in Table 1. Black lines represent the simulated PTM-DX particle trajectories, while gray lines represent the observed DX drifter trajectories for comparison. The panels are arranged by the number of forcing components included: the first row shows single-component forcing (**a**); the second row shows two-component forcings (**b-d**); the third row shows three-component forcings (**e-g**); and the fourth row shows the four-component forcing (**h**). G, E, S, and W indicate geostrophic current, Ekman current, Stokes drift, and windage forcings, respectively.

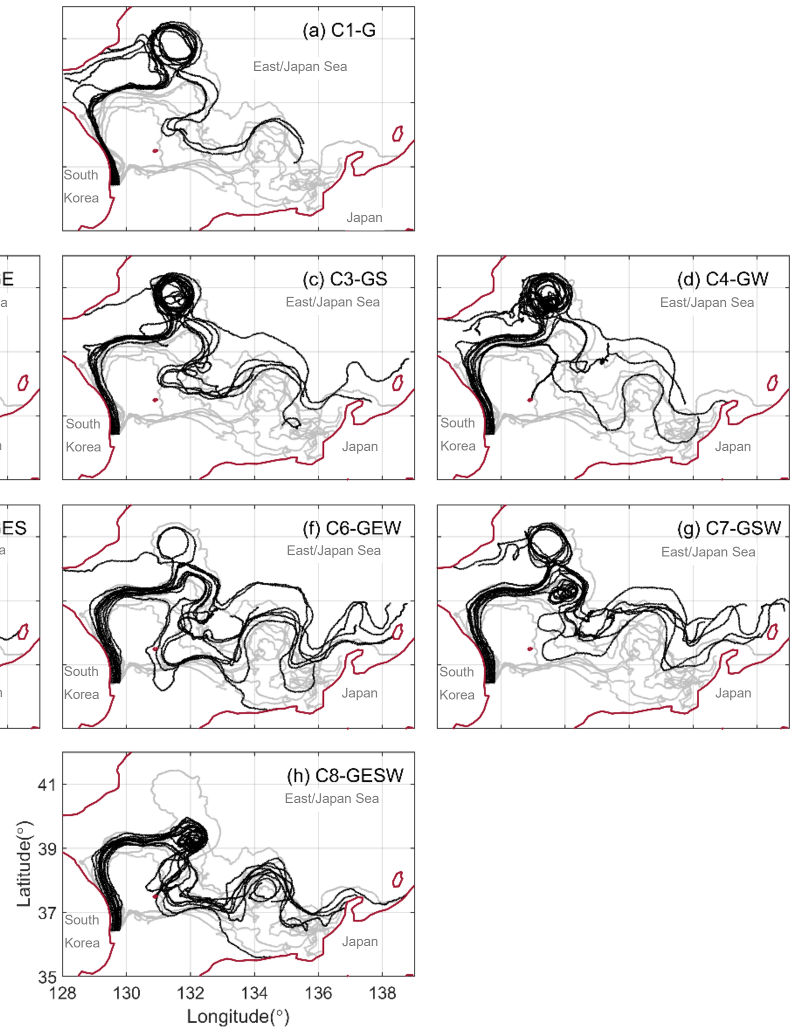

Figure 6. Particle trajectories using surface forcings (PTM-DO) simulated for 3 months. Panels (**a-h**) correspond to current combinations C1-C8 as described in Table 1. Black lines represent the simulated PTM-DO particle trajectories, while gray lines represent the observed DO drifter trajectories for comparison. The panels are arranged by the number of forcing components included: the first row shows single-component forcing (**a**); the second row shows two-component forcings (**b-d**); the third row shows three-component forcings (**e-g**); and the fourth row shows the four-component forcing (**h**). G, E, S, and W indicate geostrophic current, Ekman current, Stokes drift, and windage forcings, respectively.

3.4 Particle dispersion

Figure 7 presents the time evolution of relative dispersion, $D^2(t)$, for PTM-DX and PTM-DO particles under the eight forcing combinations (C1-C8). Overall, the two PTM sets exhibited comparable dispersion magnitudes and slopes; however, notable differences arose when windage was included. In cases where windage was applied (Fig. 7d and 7f-h), PTM-DX particles exhibited greater dispersion than PTM-DO particles, contrary to the drifter observations, which showed that DO drifters experienced higher dispersion, particularly at mesoscale distances. This discrepancy stemmed from the model's failure to reproduce the bifurcation at the hyperbolic-type bifurcation region. In the observations, both DX and DO drifters split between an offshore path and the EKWC path, albeit with different proportions: more DX drifters followed the offshore route, while more DO drifters remained along the EKWC, where coastal shear enhanced dispersion. In contrast, the simulations confined all PTM-DO particles to the EKWC path, while PTM-DX particles were distributed between both paths. Since particles restricted to the EKWC path experience weaker dispersion compared to those traversing both the EKWC and offshore routes, the PTM-DO simulations underestimated dispersion relative to PTM-DX, opposite to the pattern observed in the drifter data.

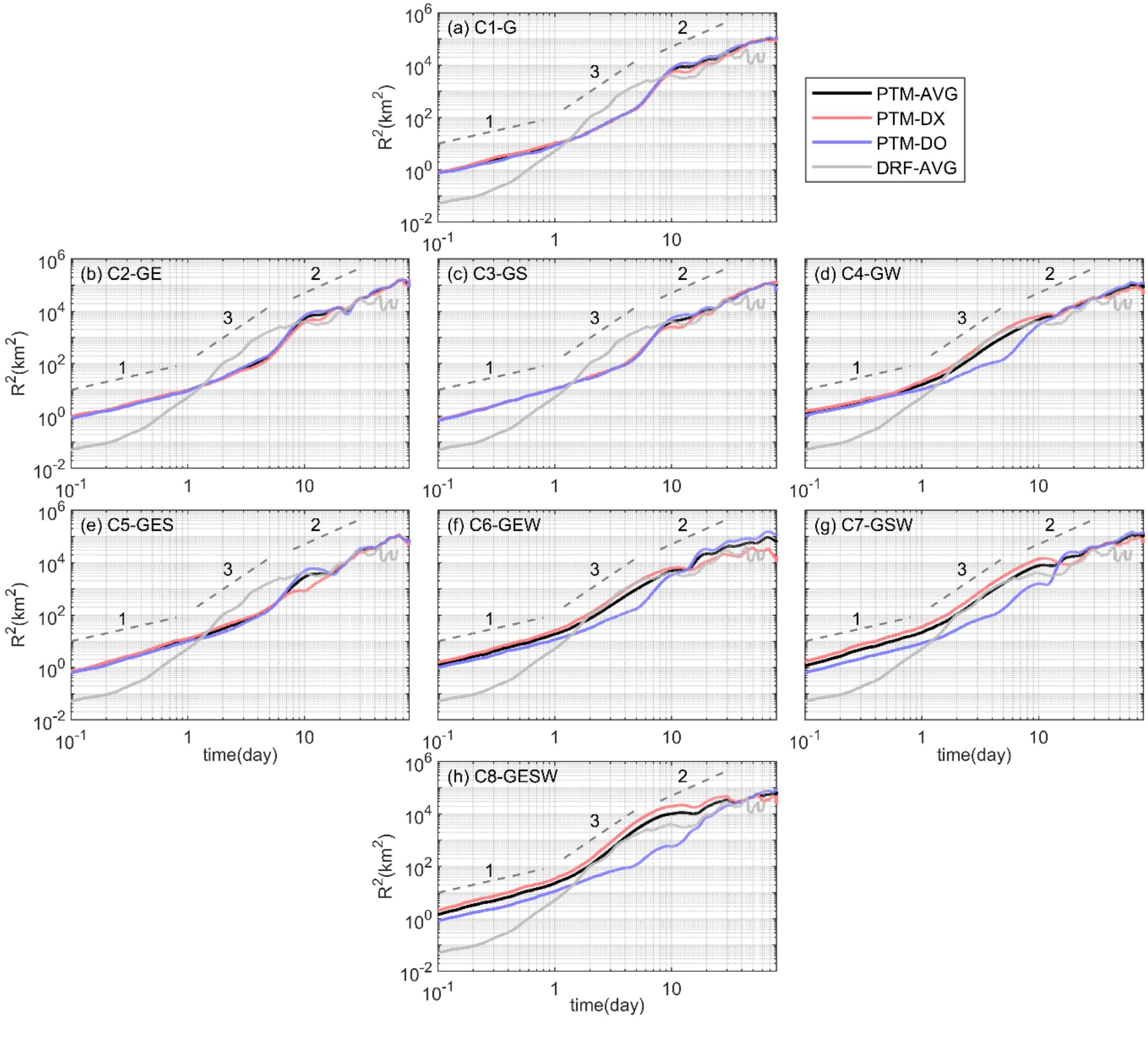

Figure 7. Relative dispersion ($R^2(t)$) of particles simulated with different forcing combinations (C1-C8) as described in Table 1, shown alongside observed drifter dispersion. Panels are arranged in the same order as in Fig. 5 and 6. Red and blue lines represent the relative dispersions for PTM-DX and PTM-DO simulations, respectively, and the gray line represents the average relative dispersion of the observed drifters for comparison. G, E, S, and W indicate geostrophic current, Ekman current, Stokes drift, and windage forcings, respectively.

Both particles and drifters exhibited a diffusive phase during the early stages; however, this phase persisted only briefly for the drifters ($t < 0.3$ days), while it extended significantly longer for the particles, up to approximately 2 days, until the average pairwise separation distance reached approximately 25 km, corresponding to the grid spacing of the velocity field used in the PTM calculations. As a result, the effective diffusivity of particle pairs separated by less than 25 km was substantially higher than that observed in the drifter data. This discrepancy arises from the Smagorinsky scheme, which applies a constant diffusion coefficient within each 25 km grid cell, leading to artificially enhanced diffusion at very early times in all PTM simulations. The domain-averaged horizontal diffusion coefficient during the drifter observation period (November 2021 to February 2022), computed using the Smagorinsky parameterization, was approximately 87.3 m^2/s. This value is consistent with the empirical, scale-dependent horizontal diffusivity described by Okubo (83.7 m^2/s), given by $K = 0.0103L^{1.15}$, where K is in cm^2/s and L is the spatial scale in cm. In this context, L is taken as $3\sigma_r$, or equivalently $3\Delta x$, with $\Delta x = 25$ km representing the grid spacing of the velocity field used in the PTM simulations.

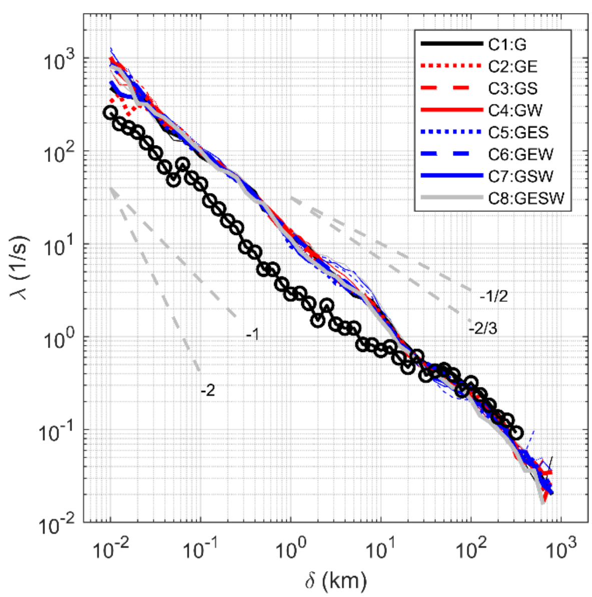

Figure 8. Finite-Size Lyapunov Exponent (FSLE), λ, as a function of separation distance, δ, for the simulated particles and observed drifters. The black line with circles represents the FSLE averaged for all observed drifters. Other colored lines show FSLEs for simulated particles from different forcing combinations (C1-C8, as listed in Table 1). Thinner lines indicate PTM-DX simulations, and thicker lines indicate PTM-DO simulations. The variation in FSLE values between different forcing combinations and between PTM-DX and PTM-DO were small.

The FSLE (λ) for the particle simulations (C1-C8) showed only minor differences among the various forcing combinations (Fig. 8). FSLE values from simulated particles and observed drifters became comparable at spatial scales greater than approximately 25 km, which aligns closely with the spatial grid size used for the current data in the simulations. At scales smaller than approximately 25 km, the FSLEs of the simulated particles were roughly three times greater than those observed from real drifters. This disparity at smaller scales occurs because particles in simulations are initially confined within grid cells, influenced significantly by numerical diffusion inherent in the Smagorinsky scheme. At these early times and small scales, the FSLE slopes for the drifters and particles are approximately -1, indicative of a ballistic dispersion regime. At intermediate spatial scales between about 25 km and 200 km, the FSLE curves for the simulated particles exhibit a slope closer to -1/2, signifying a local dispersion regime. Beyond roughly 200 km, the FSLE slopes steepen, approaching a slope of about -5/4, particularly evident in simulations where many particles eventually reach the coastline.

3.5 Data-driven optimal forcing combinations

The performance of the different data-driven forcing combinations was evaluated using the mean absolute error (MAE; Eq. 7) and the normalized cumulative Lagrangian separation skill score (NCLS; Eq. 8). The MAE values at selected time steps are summarized in Table 3, whereas the NCLS results are presented as temporal variations in Fig. 9 rather than in a separate table. Together, these two metrics were used to evaluate both the magnitude of trajectory error and the temporal consistency of model skill. The values in parentheses in Table 3 indicate the ratio of each MAE to the lowest MAE at the corresponding time step; therefore, values closer to 1 indicate better relative performance.

Table 3. MAE values for undrogued particles (PTM-DX) and drogued particles (PTM-DO) under different forcing combinations (C1–C8) over time. Lower MAE values indicate better model performance. Bolded values represent the lowest MAE for each time step. Values in parentheses show the ratio of each MAE to the lowest MAE for that time step, a ratio closer to 1 denotes better relative performance.

		C1	C2	C3	C4	C5	C6	C7	C8
	day	u_G	u_{G+E}	u_{G+S}	u_{G+W}	u_{G+E+S}	u_{G+E+W}	u_{G+S+W}	$u_{G+E+S+W}$
	1	22.7 (2.1)	23.2 (2.1)	18.6 (1.7)	15.2 (1.4)	18.4 (1.7)	14.9 (1.4)	**10.8 (1.0)**	11.1 (1.0)
	5	134.5 (6.1)	107.3 (4.9)	122.7 (5.6)	90.0 (4.1)	106.1 (4.8)	57.0 (2.6)	**22.0 (1.0)**	19.3 (0.9)
PTM-DX	10	251.4 (10.4)	242.6 (10.1)	221.1 (9.2)	166.0 (6.9)	209.6 (8.7)	92.6 (3.8)	**24.1 (1.0)**	35.8 (1.5)
	30	475.8 (8.8)	460.7 (8.5)	308.6 (5.7)	209.0 (3.9)	265.6 (4.9)	92.0 (1.7)	**54.0 (1.0)**	91.0 (1.7)
	75	562.5 (7.6)	606.1 (8.2)	347.0 (4.7)	145.0 (2.0)	243.9 (3.3)	90.80 (1.2)	**73.8 (1.0)**	83.2 (1.1)
	avg.	289.4 (7.0)	288.0 (6.8)	203.6 (5.4)	125.0 (3.7)	168.7 (4.7)	69.5 (2.1)	**36.9 (1.0)**	48.1 (1.2)
	1	19.7 (1.3)	20.7 (1.3)	18.4 (1.2)	17.1 (1.1)	18 (1.2)	16.7 (1.1)	15.9 (1.0)	**15.4(1.0)**
	5	75.7 (1.4)	64.1 (1.2)	79.3 (1.4)	68.7 (1.2)	68.8 (1.2)	59.2 (1.1)	68.7 (1.2)	**55.3(1.0)**
PTM-DO	10	146.5 (1.4)	135.6 (1.3)	140.2 (1.3)	123.1 (1.2)	129.4 (1.2)	113.8 (1.1)	120.1 (1.1)	**107(1.0)**
	30	318.0 (2.9)	286.5 (2.6)	304.9 (2.8)	235.6 (2.1)	216.9 (2.0)	175.5 (1.6)	201.4 (1.8)	**110.7(1.0)**
	75	537.0 (2.9)	487.9 (2.6)	487.9 (2.6)	377.1 (2.0)	459.6 (2.5)	322.6 (1.7)	410.3 (2.2)	**185.2 (1.0)**

avg.	219.4 (2.0)	199.0 (1.8)	206.1 (1.9)	164.3 (1.5)	178.5 (1.6)	137.6 (1.3)	163.3 (1.5)	**94.7 (1.0)**

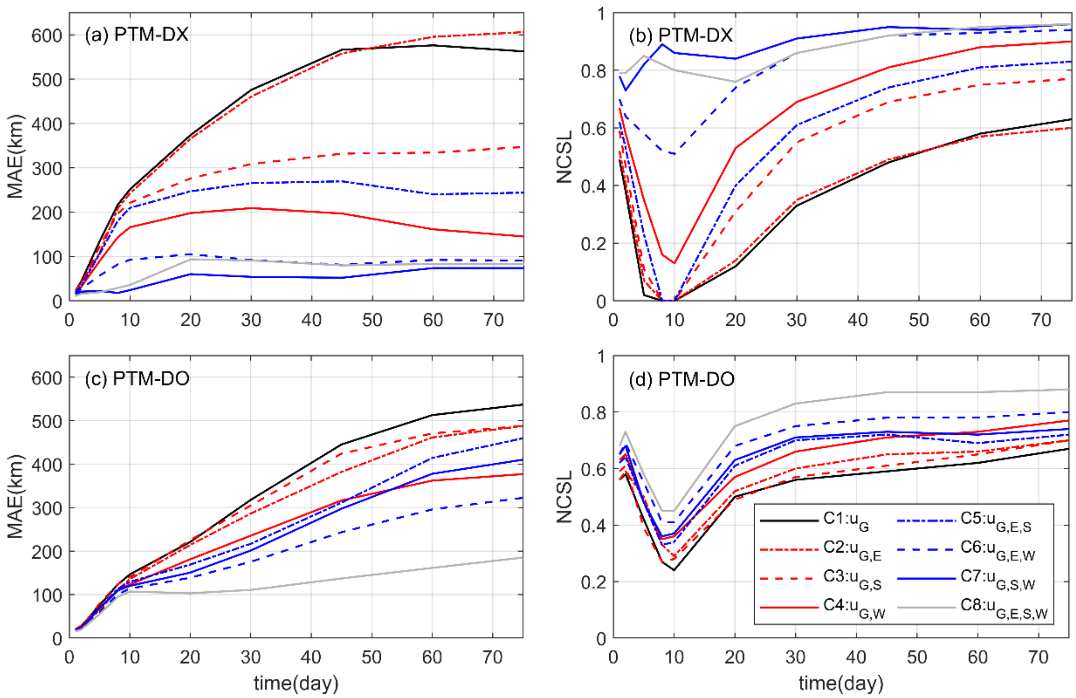

Figure 9. Temporal evolution of MAE for PTM-DX simulations (**a**) and PTM-DO simulations (**c**), and temporal evolution of NCLS for PTM-DX simulations (**b**) and PTM-DO simulations (**d**) for different forcing combinations (C1-C8, as listed in Table 1).

For PTM-DX, the simulation using only the geostrophic current (C1) showed the poorest overall performance, with an average MAE of 289.4 km. Adding the Ekman current to the geostrophic current (C2) did not improve the trajectory prediction, indicating that the Ekman component alone was insufficient to reproduce the observed DX drifter pathways. In contrast, the addition of windage substantially improved model performance. Among the two-component combinations, C4, which included geostrophic current and windage, reduced the average MAE to 125.0 km. This improvement suggests that direct wind forcing played an important role in the motion of the undrogued DX drifters.

Among the three-component combinations for PTM-DX, C7, which combined geostrophic current, Stokes drift, and windage, provided the best overall performance. C7 produced the lowest average MAE of 36.9 km and showed the highest or near-highest skill over most of the simulation period. Although C8, which included all four forcing components, showed slightly better performance at day 5, its average MAE was larger than that of C7. This result indicates that adding the Ekman current to the DX simulation did not further improve the prediction and could even degrade the trajectory skill after the early separation stage. Therefore, the optimal data-driven forcing combination for PTM-DX was identified as C7, consisting of geostrophic current, Stokes drift, and windage.

To evaluate the uncertainty associated with the windage coefficient without treating it as a free tuning parameter, an additional sensitivity test was conducted for PTM-DX, because the undrogued DX drifters are most directly exposed to wind forcing. The geometry-based value, $r = 0.015$, was compared with $r = 0.005$ and $r = 0.030$, representing weaker and stronger windage effects, respectively. The optimal forcing combination changed when r was substantially modified: $r = 0.005$ favored C8, $u_g + u_e + u_s + u_w$, with $\overline{\mathrm{MAE}} = 117.3$ km, whereas $r = 0.030$ favored C4, $u_g + u_w$, with $\overline{\mathrm{MAE}} = 88.2$ km. However, the geometry-based value $r = 0.015$ produced the lowest overall error, with C7, $u_g + u_s + u_w$, giving $\overline{\mathrm{MAE}} = 42.9$ km. These results indicate that the trajectory skill is sensitive to the windage coefficient, but they also support the use of the geometry-based value $r = 0.015$ rather than tuning r freely to minimize trajectory error.

The temporal evolution of MAE and NCLS further supports this interpretation (Fig. 9a,b). The C1 and C2 simulations exhibited rapid error growth and eventually reached MAE values of approximately 600 km. In contrast, the simulations that included windage, particularly C6, C7, and C8, maintained substantially lower MAE values. A rapid change in MAE and NCLS occurred around day 10, corresponding to the period when the particles passed near the hyperbolic-type bifurcation region off the eastern Korean coast. In this region, small differences in the early simulated trajectories can determine whether particles follow the coastal northward pathway or the offshore eastward pathway. Thus, accurately representing the early wind-driven displacement near this bifurcation region was critical for reproducing the downstream trajectories of the DX drifters.

To further examine whether the MAE-based ranking was dominated by accumulated downstream separation after the early bifurcation, we also performed a segment-based MAE analysis for the DX simulations. The observed and simulated DX trajectories were divided into 3-day segments, and the MAE was calculated independently for each segment to evaluate short-term local trajectory skill. This analysis showed that the full forcing case, $u_g + u_e + u_s + u_w$, produced the lowest segment-based error, with $\overline{\mathrm{MAE}} = 28.7 \pm 3.7$ km, followed by $u_g + u_s + u_w$, with $\overline{\mathrm{MAE}} = 31.3 \pm 8.3$ km. Thus, while the cumulative MAE identified $u_g + u_s + u_w$ as the best integrated pathway predictor for DX, the segment-based analysis indicates that $u_g + u_e + u_s + u_w$ provided the most stable short-term local trajectory skill. This confirms that the windage- and Stokes-drift-inclusive forcings were important not only for the accumulated downstream pathway, but also during the early bifurcation stage.

For PTM-DO, the differences among the forcing combinations were less pronounced than for PTM-DX, reflecting the weaker direct wind response of the drogued drifters. Nevertheless, the inclusion of additional forcing components generally improved the trajectory prediction. The geostrophic-only case (C1) produced an average MAE of 219.4 km, while C4 reduced the average MAE to 164.3 km. Among the three-component combinations, C6, which included geostrophic current, Ekman current, and windage, showed the best performance, with an average MAE of 137.6 km. This result suggests that the Ekman component was more important for the drogued DO drifters than for the undrogued DX drifters, consistent with the deeper effective sampling depth of the DO drifter.

The best overall performance for PTM-DO was obtained with C8, which included geostrophic current, Ekman current, Stokes drift, and windage. C8 produced the lowest MAE at all selected time steps and reduced the average MAE to 94.7 km. The NCLS evolution also showed that C8 consistently maintained the highest trajectory skill for the DO simulations (Fig. 9c,d). Therefore, unlike the DX case, the inclusion of all four forcing components was necessary to reproduce the observed DO drifter trajectories most accurately.

To examine whether the identified optimal forcing combinations were affected by the stochastic random-walk diffusion term, an additional ensemble-sensitivity test was conducted using 10 particles for each drifter initial location. The deterministic velocity fields were kept identical to those in the original simulations, while only the Gaussian random sequences in the diffusion term were varied. The resulting ensemble-mean MAE values differed slightly from the original single-particle results, but the main forcing rankings remained unchanged. For PTM-DX, C8 produced the lowest MAE at the early time of 5 days, whereas C7 remained the best-performing case at later times and for the average MAE. For PTM-DO, C8 remained the best-performing forcing combination. These results indicate that the stochastic diffusion term affects the exact MAE values but does not control the main conclusion regarding the optimal forcing combinations.

Overall, the optimal forcing combination differed between the two drifter types. For the undrogued DX drifters, the best performance was achieved by combining geostrophic current, Stokes drift, and windage, indicating that near-surface transport was strongly controlled by wave-induced drift and direct wind forcing. For the drogued DO drifters, the full forcing combination including Ekman current was required, suggesting that the deeper drogued drifters were more strongly influenced by subsurface wind-driven shear. These results demonstrate that the optimal PTM forcing depends on the effective sampling depth and wind exposure of the drifting object, and that a single surface-current forcing configuration may not be appropriate for all types of floating debris or drifters.

4 Discussions

4.1 Comparison with model-derived velocity products

The optimized data-driven forcing combinations were further compared with simulations driven by model-derived surface velocity products. In this comparison, the GOFS analysis based on HYCOM/NCODA and the GLORYS12V1 reanalysis distributed by Copernicus Marine were used as benchmark velocity fields. These products are referred to hereafter as HYC and CMS, respectively, to remain consistent with the notation used in Table 4. The purpose of this comparison was not to repeat the full forcing-decomposition experiment conducted for the data-driven approach, because these analysis/reanalysis products already assimilate observations and provide dynamically consistent surface velocity fields that may include both geostrophic and ageostrophic wind-driven components. Instead, the model-derived velocities were used directly, and additional direct windage and Stokes drift terms were tested to examine whether these processes improved the simulated pathways of the undrogued DX drifters.

Table 4. Table 4. MAE and NCLS values for PTM-DX simulations driven by model-derived surface velocity products, namely the GOFS analysis based on HYCOM/NCODA and the GLORYS12V1 reanalysis distributed by Copernicus Marine, with and without additional windage and Stokes drift. HYC denotes the GOFS/HYCOM analysis, and CMS denotes the GLORYS12V1 reanalysis product GLOBAL_MULTIYEAR_PHY_001_030. W1 and W2 denote windage terms corresponding to 1.5% and 3.0% of the 10-m wind speed, respectively, and ST denotes the addition of Stokes drift calculated from the wave model.

	day	CMS	CMS-W1	CMS-W2	CMS-W1-ST	HYC	HYC -W1	HYC -W2	HYC-W1-ST
MAE	1	22.0 (2.0)	14.6 (1.4)	8.1 (0.8)	5.5 (0.5)	25.2 (2.3)	14.6 (1.4)	13.4 (1.2)	15.5 (1.4)
	5	134.9 (6.1)	43.6 (2.0)	40.1 (1.8)	39.2 (1.8)	76.8 (3.5)	25.8 (1.2)	30.3 (1.4)	21.7 (1.0)
	10	237.0 (9.8)	69.0 (2.9)	64.7 (2.7)	60.0 (2.5)	174.4 (7.2)	32.1 (1.3)	61.0 (2.5)	26.5 (1.1)
	30	415.9 (7.7)	72.0 (1.3)	165.8 (3.1)	150.7 (2.8)	234.7 (4.3)	158.1 (2.9)	201.7 (3.7)	156.1 (2.9)
	75	413.6 (5.6)	126.6 (1.7)	175.7 (2.4)	163.7 (2.2)	182.7 (2.5)	195.4 (2.6)	201.7 (2.7)	163.4 (2.2)
	avg.	244.7 (6.2)	65.2 (1.9)	90.9 (2.2)	83.8 (2.3)	138.8 (4.0)	85.2 (1.9)	101.6 (2.3)	76.64 (2.1)
NCLS	1	0.52 (1.3)	0.70 (1.1)	0.84 (0.9)	0.87 (1.1)	0.52 (1.3)	0.72 (1.1)	0.74 (1.1)	0.71 (0.9)
	5	0.02 (2.0)	0.67 (1.2)	0.70 (1.1)	0.71 (0.9)	0.39 (1.5)	0.80 (1.0)	0.75 (1.1)	0.83 (1.0)
	10	0.00 (2.0)	0.62 (1.3)	0.63 (1.3)	0.64 (0.7)	0.05 (1.9)	0.82 (1.0)	0.64 (1.3)	0.85 (1.0)
	30	0.41 (1.5)	0.89 (1.0)	0.76 (1.2)	0.78 (0.9)	0.65 (1.3)	0.74 (1.2)	0.74 (1.2)	0.74 (0.8)
	75	0.72 (1.3)	0.91 (1.1)	0.94 (1.0)	0.95 (1)	0.87 (1.1)	0.92 (1.0)	0.95 (1.0)	0.95 (1.0)
	avg.	0.33 (1.6)	0.76 (1.1)	0.77 (1.1)	0.79 (0.9)	0.50 (1.4)	0.80 (1.1)	0.76 (1.1)	0.82 (0.9)

Table 4 summarizes the MAE and NCLS values for PTM-DX simulations driven by HYC and CMS, with and without additional windage and Stokes drift. In Table 4, W1 and W2 denote windage terms corresponding to 1.5% and 3.0% of the 10-m wind speed, respectively, while ST denotes the addition of Stokes drift calculated from the wave model. These percentages therefore refer to the windage coefficient, not to a scaling of Stokes drift. The values in parentheses are normalized by the performance of C7, which was the optimal data-driven forcing combination for PTM-DX.

The model-derived simulations generally showed poorer trajectory skill than the optimized data-driven forcing combination. Although the addition of windage and Stokes drift improved some HYC and CMS cases, the resulting MAE values remained larger and the NCLS values remained lower than those obtained with C7. This indicates that the poorer performance of HYC and CMS was not caused simply by the absence of direct windage or Stokes drift. Rather, it was related to differences in the local near-surface velocity structure during the early stage of the simulation, when small trajectory errors strongly affected the subsequent downstream pathway. The temporal resolution of the velocity products may also have contributed to these differences. The GLORYS12V1 reanalysis provides daily mean fields, whereas the wind-related components in the reconstructed forcing were derived from hourly ERA5 wind forcing. Therefore, high-frequency near-surface wind-driven variability may have been more strongly smoothed in the GLORYS-based simulation than in the reconstructed forcing fields. To examine this mechanism, FTLE fields were computed using one-week-averaged velocity fields from the drifter release date within the same domain used for the velocity-field comparison. Figure 10 compares the FTLE structures obtained from the data-driven velocity fields and the model-derived velocity fields. The first row shows the FTLE fields for the geostrophic current alone, the data-driven combination without windage, and the data-driven combination including windage. The second and third rows show the corresponding CMS- and HYC-based cases, respectively, with and without additional windage and Stokes drift.

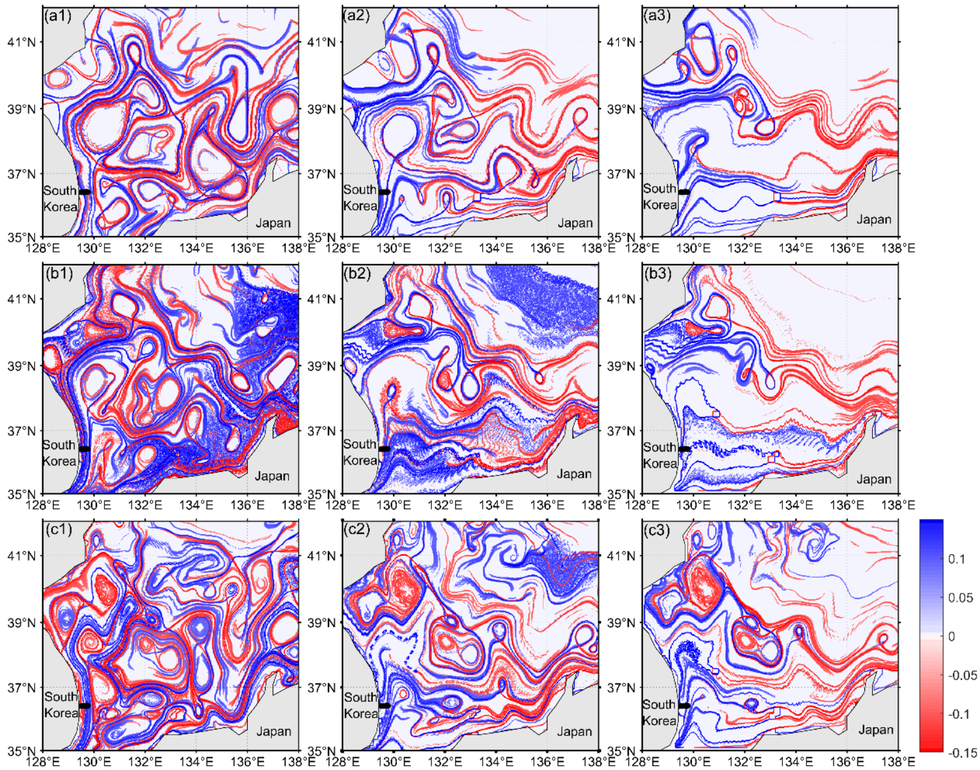

Figure 10. Finite-time Lyapunov exponent (FTLE) structures computed from one-week-averaged velocity fields. The panels show FTLE fields for (**a1**) u_g, (**a2**) $u_g + u_e + u_s$, (**a3**) $u_g + u_e + u_s + u_w$, (**b1**) CMS, (**b2**) CMS-w1, (**b3**) CMS-w1-st, (**c1**) HYC, (**c2**) HYC-w1, and (**c3**) HYC-w1-st. Here, u_g, u_e, u_s, and u_w denote geostrophic current, Ekman current, Stokes drift, and windage, respectively. CMS denotes the GLORYS reanalysis distributed by Copernicus Marine, and HYC denotes the GOFS analysis based on HYCOM.

The data-driven velocity fields showed a clear transport-separating FTLE structure near the early bifurcation region off the eastern Korean coast. In particular, the geostrophic current field and the data-driven combined velocity fields retained a ridge structure in which attracting and repelling FTLE ridges were closely aligned or intersected near the region where the observed drifter trajectories initially separated. This structure is consistent with a hyperbolic-type bifurcation region rather than a mathematically exact, stationary hyperbolic point. Because the drifters were released close to this Lagrangian transport boundary, small differences in initial position and forcing could separate the particles into different pathways: one following the coastal northward route along the East Korea Warm Current and the other moving offshore and subsequently eastward.

In contrast, the CMS- and HYC-based FTLE fields did not show a comparable hyperbolic-type ridge intersection in the same region. The model-derived FTLE structures were smoother, weaker, or spatially displaced relative to the data-driven FTLE structure. Adding windage and Stokes drift to the CMS and HYC velocity fields changed the magnitude and direction of particle advection, but it did not reconstruct the same transport-separating FTLE pattern near the release region. This explains why the model-derived simulations could not reproduce the early pathway separation as accurately as the optimized data-driven forcing combination.

The FTLE comparison therefore supports the trajectory-based evaluation in Table 5. The improved performance of the data-driven approach does not imply that the GOFS analysis or GLORYS12V1 reanalysis lack geostrophic dynamics. Both products assimilate sea-level information, but their surface velocity fields are dynamically adjusted by the model physics, data-assimilation scheme, vertical mixing, spatial resolution, and temporal averaging. Rather, the result indicates that the early drifter bifurcation was highly sensitive to the local structure of the near-surface velocity field. The data-driven geostrophic-based forcing combinations better preserved the FTLE ridge structure associated with this bifurcation region, whereas the HYC and CMS velocity fields smoothed or displaced the local transport boundary. Consequently, once the simulated particles selected an incorrect pathway during the first stage of transport, the downstream separation error increased rapidly, leading to larger MAE and lower NCLS values over the full trajectory.

Overall, the comparison with HYC and CMS confirms that the key advantage of the optimized data-driven forcing is not only the inclusion of additional windage or Stokes drift, but also the ability to reproduce the local Lagrangian transport structure controlling the early bifurcation of the drifter pathways. This finding emphasizes that accurate representation of transport-separating structures near the release region is essential for predicting the fate of near-surface floating particles in the East/Japan Sea.

4.2 Seasonal variation of atmospheric and oceanic forcings

The seasonal variation of waves and winds that potentially influence the transport of floating debris is illustrated in Fig. 11. Both significant wave height (SWH) and wind speed follow a clear seasonal pattern, increasing in the order of summer (June-August), fall (September-November), spring (March-May), and winter (December-February). During fall and winter (Fig. 11g and 11h), the EJS is subject to persistent and strong northwesterly winds, which generate significantly higher wave heights near the Japanese coastline due to fetch-limited wave development from the Korean Peninsula (Chen et al., 2002; Park et al., 2005; Ebuchi, 1999). Monthly averaged satellite-derived SWHs show a pronounced seasonal variability, with high values exceeding 2.5 m in winter and low values below 1 m in summer (Woo and Park, 2017), consistent with the seasonal averages depicted in Fig. 10. This spatial asymmetry in wave height enhances wave-driven surface transport (Stokes drift) toward the Japanese coast during winter. The mean winter SWH reaches 1.68 m, with a maximum of 2.58 m. In contrast, during summer, the mean SWH decreases to 0.55 m, with a peak of 0.82 m, and wave propagation is influenced by prevailing southerly winds, which tend to shift northward.

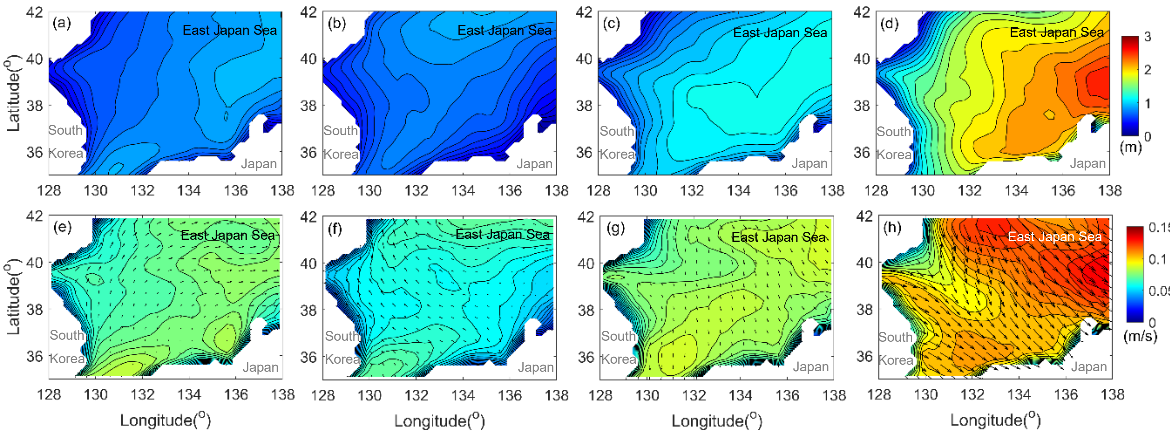

Figure 11. The mean of significant wave height (**a-d**), wind (**e-f**) in EJS for each season in 2021: (**a,e**) spring (March 01-May 30), (b,f) summer (June 01-August 30), (**c,g**) autumn (Septemper 01-November 30), and (**d,h**) winter (December 01-February 28).

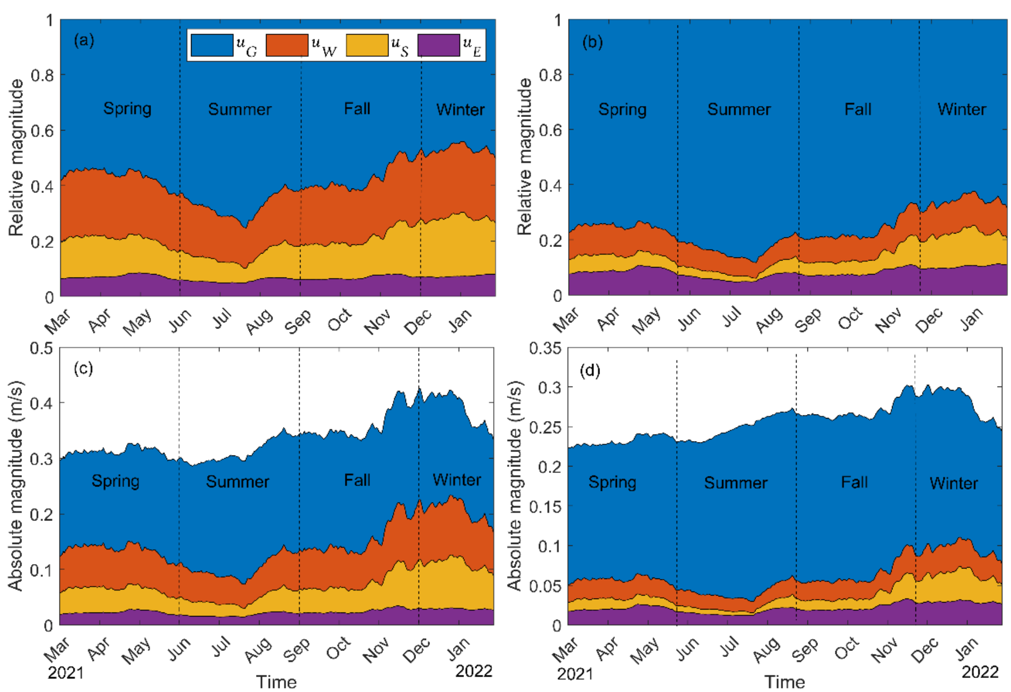

Figure 12. The relative and absolute value of the current components at the surface (**a,c**) and 1.5m- depth (**b,d**) of (u_G-geostrophic current, u_w-wind-driver current, u_s-Stoke current and u_E-Ekman current) from March 2021 to February 2022.

Like the distinct seasonal variations in wave and wind strength and direction, the direct forcings driving surface debris transport also exhibited marked seasonal variability. Figure 12 presents the absolute and relative magnitudes of the forcing components for PTM-DX (Fig. 12a, and c) and PTM-DO (Fig. 12b, and d). For PTM-DX forcings, the geostrophic current was the dominant component year-round, contributing approximately 68% of the total forcing in summer and declining to around 48 % in winter. Among the remaining components, windage and Stokes drift made comparable contributions, both substantially exceeding that of the Ekman current across all seasons. Similarly, for PTM-DO, the geostrophic current remained the primary forcing component, contributing about 83% in summer and decreasing to roughly 65% in winter. The other three components, windage, Stokes drift, and Ekman current, had similar magnitudes, particularly during winter. However, Stokes drift was generally less influential than windage and Ekman current, likely due to its more rapid exponential decay with depth (e^{-2kz}), in contrast to the slower decay of the Ekman current ($e^{-z/d}$). The estimated Ekman depth ranged from approximately 15 m in summer to 30 m in winter, substantially deeper than the depth affected by Stokes drift. Consequently, the absolute magnitude of the Ekman current contribution showed little variation between PTM-DX and PTM-DO.

The PTM results indicate that the optimal current representation for tracking DX drifters is achieved using three components: geostrophic current, Stokes drift, and windage. This combination performed slightly better than the full four-component setup, suggesting potential redundancy or overestimation when the Ekman current is included in modelling surface debris transport. In contrast, the optimal configuration for PTM-DO involved all four components, indicating that at subsurface depths, overlap among wind-driven forcings, such as windage, Stokes drift, and the Ekman current, is reduced, and their combined influence is necessary to achieve the best performance.

4.3 Seasonal variation of particle transport and dispersion

The seasonal variation of atmospheric and oceanic forcings near the air–sea interface, as described in the previous section, plays a key role in determining the fate of floating debris in the EJS. To investigate the seasonal variability in floating debris dispersion and transport driven by surface forcings, a particle tracking model was run using the optimal forcing combination for DX drifters (C7). A total of 576 particles were released at the ocean surface near the southwestern entrance to the EJS, with releases occurring every five days throughout the year (March 2021 to February 2022), and each particle was tracked for five months. Figure 13 presents streamlines based on seasonally averaged velocity fields (Fig. 13a, c, e, and g), along with the corresponding seasonal particle accumulation maps (Fig. 13b, d, f, and h), showing the relative frequency of particle presence within 5 km grid cells. The three red streamlines highlight trajectories passing through the same points along the eastern side of the subpolar front near 40°N.

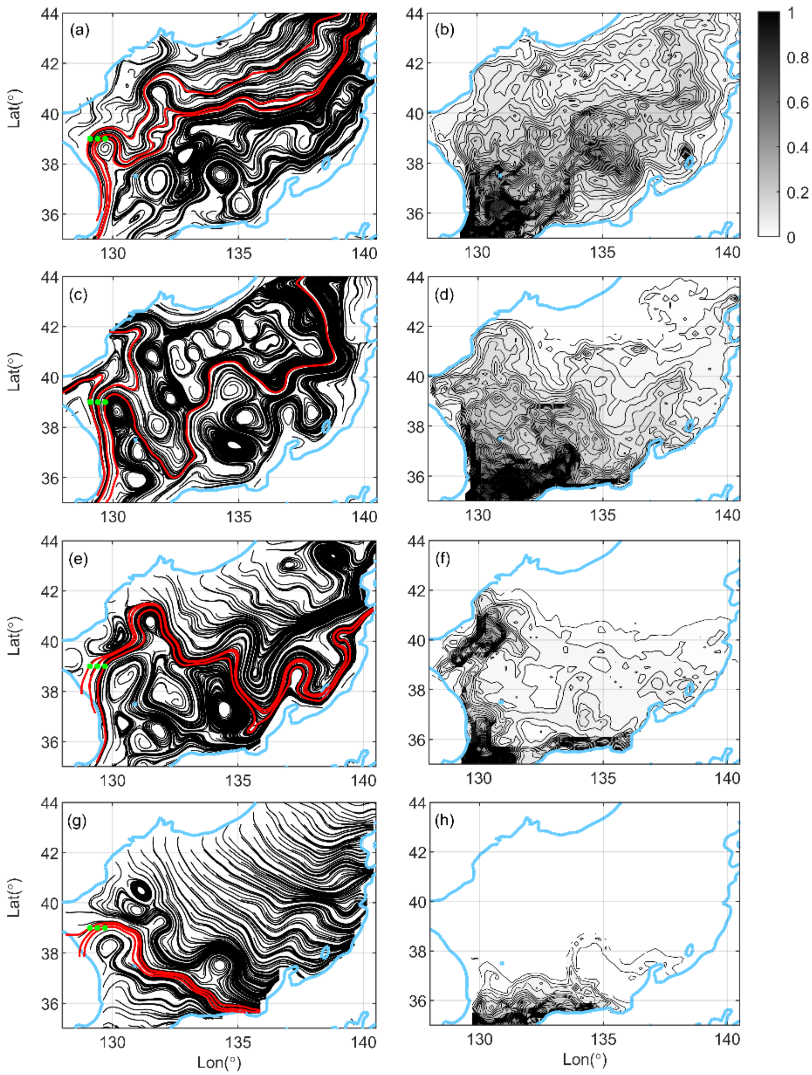

Figure 13. Seasonal streamlines and particle accumulation maps from March 2021 to February 2022, simulated using the optimal forcing combination (C7). Panels (**a, c, e, g**) show streamlines of the seasonally averaged surface current for spring (March–May), summer (June–August), autumn (September–November), and winter (December–February), respectively. Panels (**b, d, f, h**) show the corresponding seasonal particle accumulation maps. Red lines represent streamlines that pass through three fixed points marked in green. Particles were released every five days from March 2021 to February 2022 at the southwestern entrance of the EJS and tracked for five months. The accumulation maps display the relative frequency of particle occurrence, calculated as the number of particle passages through each 5 km grid cell normalized by the maximum frequency.

In spring (Fig. 12a, and b), the streamlines reveal that relatively strong winds blow northward near the Korean Peninsula and shift northeastward, especially in the northern EJS, facilitating material transport along and above the subpolar front. This wind-driven configuration results in the broadest dispersion of floating debris among all seasons. In summer (Fig. 12c, and d), the flow is characterized by eddy-like coherent patterns throughout the EJS, driven by persistent mesoscale circulations under the weakest wind conditions. A branch of the EKWC flows northward along the coast and forms a closed streamline loop in the northern coastal region. This circulation pattern suggests that particles entrained on the western side of the EKWC become trapped and accumulate along the Korean coastline. In fall (Fig. 12e, and f), streamlines originating from the northern coastline extend southeastward across the northern EJS. The red streamlines show minimal variation, indicating relatively slow northward particle movement. This is consistent with the broader, lower-concentration particle distributions observed in the accumulation map. Additionally, the streamlines near the Japanese coastline remain open, allowing debris to continue along the coast. In winter (Fig. 12g, and h), most streamlines appear nearly straight, influenced by strong and consistent west-northwesterly winds and wave propagation in the same direction. As a result, particle trajectories are largely confined to the southern EJS. Given that our drifters were released in mid-November and tracked for several months, the fall and winter transport maps (Fig. 12e, f and Fig. 12g, h) effectively represent the observed fate of drifters that eventually beached along the Japanese coastline.

The seasonal beaching locations of particles are illustrated in Fig. 14, where beaching is defined as particle contact with the coastline. In spring (Fig. 14a), the number of beached particles was the lowest among all seasons, with a substantial portion remaining offshore. This pattern corresponds with the springtime streamline plots, which show predominantly northeastward transport across the EJS and limited streamline closure near the coast. In summer (Fig. 14b), when winds were weakest, the widest spatial distribution of beaching was observed, with particles reaching both the Japanese and Korean coastlines surrounding the EJS. Fall (Fig. 14c) was characterized by concentrated beaching along the southern coasts of both Japan and Korea, with particularly pronounced accumulation along the Japanese coastline. In winter (Fig. 14d), strong northwesterly winds likely contributed to increased beaching intensity along the southern Japanese coast. These seasonal mechanisms align with previous numerical studies: Yoon et al. (2010) highlighted the dominant role of monsoonal winds and windage in driving seasonal peaks of floating debris accumulation along the Japanese coast, while Iwasaki et al. (2017) demonstrated that intensified winter wave conditions and associated Stokes drift significantly enhance the onshore transport of buoyant debris toward Japan.

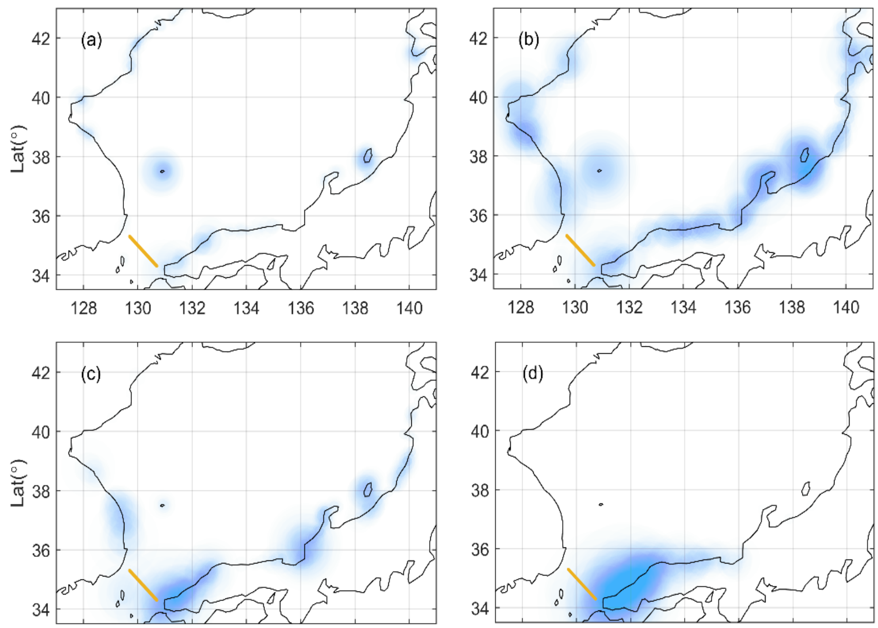

Figure 14. Spatial distribution and relative accumulation intensity of beached particles simulated using the optimal surface forcing (C7) for (a) spring (March–May), (b) summer (June–August), (c) fall (September–November), and (d) winter (December–February). The beached particle locations were determined from the same particle trajectories used in Fig. 13. Beaching is defined as the behavior of particles first contacting the coastline. The particle release location is marked by the yellow line. Color intensity along the coastline indicates the relative density of particle accumulation, with darker shades representing higher accumulation.

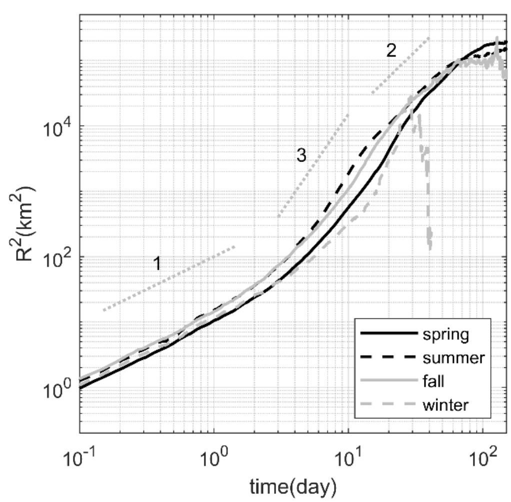

Figure 15. Seasonal variation of relative dispersion, R^2 (t), for particles (same as those used in Fig. 13, and 14) simulated using the optimal forcing combination (C7). Lines indicate relative dispersion for particles released in spring (black solid), summer (black dashed), autumn (gray solid), and winter (gray dashed).

The seasonal variation in relative dispersion can also be interpreted in terms of atmospheric and oceanic forcings (Fig. 15). In all cases, dispersion initially exhibited a brief period of slow growth, attributed to the model's constant diffusivity within grid cells, followed by a more rapid increase consistent with Richardson-like behavior, continuing until approximately 30 days after release. During this phase, particles released in winter showed the lowest relative dispersion, while those released in summer exhibited the highest. The reduced dispersion in winter likely resulted from persistent strong winds and waves that constrained particle motion, leading to concentrated beaching along the southern Japanese coast (Fig. 14d). In contrast, the enhanced dispersion in summer was attributed to weak winds, resulting in reduced wave action, Stokes drift, and Ekman currents, which allow mesoscale eddies to dominate particle transport. This pattern aligns with Fig. 14b, which shows widespread beaching along both the Korean and Japanese coastlines. Over time, relative dispersion in all seasons began to plateau roughly one month after release, as particle pair separations approach the basin scale. These results suggest that strong winds suppress the influence of mesoscale eddies by restructuring the flow into a more uniform, wind-driven (ballistic-like) velocity field, whereas weak winds allow particles to remain entrained within mesoscale eddies, thereby enhancing basin-wide dispersion, especially in marginal seas like the EJS.

5 Conclusions

This study evaluated the near-surface forcing combinations required to reproduce observed drifter trajectories in the East/Japan Sea using a passive particle tracking model driven by prescribed Eulerian velocity fields and a simple random-walk representation of unresolved diffusion. The 2021 drifter experiment revealed a clear cross-basin transport pathway from the Korean coast toward Japan, with the observed trajectories separating near a hyperbolic-type Lagrangian structure.

The comparison between observed and simulated trajectories showed that the optimal forcing combination depends on drifter type and effective sampling depth. For the undrogued DX drifters, the best performance was obtained by combining geostrophic current, Stokes drift, and windage. For the drogued DO drifters, the inclusion of all four components, geostrophic current, Ekman current, Stokes drift, and windage, provided the best agreement with observations. These results indicate that wave-induced drift and direct wind forcing are essential for surface-exposed objects, whereas Ekman current becomes more important for particles with a deeper effective sampling depth.

The optimized data-driven forcing combinations also performed better than the benchmark simulations driven by the GOFS analysis and GLORYS reanalysis in this specific experiment. The FTLE comparison suggests that the reconstructed forcing fields better represented the Lagrangian structure associated with the early drifter bifurcation. This does not imply general superiority over ocean analysis or reanalysis products, but shows that explicitly combining near-surface forcing components at physically relevant depths can improve trajectory prediction for this event.

Seasonal simulations showed that winter winds accelerate eastward transport and enhance beaching along the Japanese coast, whereas weaker summer winds allow mesoscale eddies to broaden particle dispersion and produce more spatially distributed beaching patterns. These results highlight the seasonal control of wind, waves, and mesoscale circulation on near-surface transport in the EJS.

The present PTM should be interpreted as a model of the fluid-dynamical component of near-surface particle transport, not as a complete fate model for specific macroplastic or microplastic debris. Processes such as fragmentation, biofouling- or colonization-induced buoyancy change, aggregation, degradation, vertical mixing, settling, resuspension, and detailed shoreline interaction were not explicitly included. Applications to real plastic debris would therefore require additional particle-specific terms depending on particle size, shape, density, material, buoyancy, and aging. Nevertheless, this study provides a physically constrained basis for improving debris-transport modeling in the EJS and other marginal seas.

Data availability

All datasets and models used in this study are publicly available to support transparency and reproducibility. Geostrophic currents were obtained from the Copernicus Marine Service product SEALEVEL_GLO_PHY_L4_MY_008_047 (https://data.marine.copernicus.eu/product/SEALEVEL_GLO_PHY_L4_MY_008_047/description). Wind velocity at 10 m height was sourced from the ECMWF ERA5 reanalysis provided by ECMWF (https://cds.climate.copernicus.eu/datasets/reanalysis-era5-single-levels?tab=overview). Stokes drift fields were computed using the University of Miami Wave Model (https://github.com/umwm/umwm). GOFS/HYCOM data were obtained from https://www.hycom.org/data/glby0pt08/expt-93pt0, and the GLORYS12V1 reanalysis data used for the CMS benchmark simulations were downloaded from the Copernicus Marine Service product GLOBAL_MULTIYEAR_PHY_001_030. Drifter data in the East/Japan Sea is available at https://drive.google.com/file/d/15IpunKfFTN9H7z2Ww6l_ihqniNy8Rr2M/view?usp=drive_link. All trajectory analyses, and visualizations were conducted using MATLAB R2022a.

Author contributions

JMC initiated the research idea, while HTMT developed the study design and carried out the research under the guidance and scholarly discussions with JMC and YGP. The formal analysis was performed by HTMT in collaboration with JMC. The manuscript was drafted by HTMT and subsequently reviewed and revised by JMC. All authors contributed to the conceptual development and refinement of the study.

Competing interests

The authors declare there are no conflicts of interest for this manuscript

Financial support

This research was supported by the Korea Institute of Marine Science & Technology Promotion (KIMST) funded by the Ministry of Oceans and Fisheries (20220546).

References

Amante, C., & Eakins, B. W. (2009). ETOPO1 Global Relief Model converted to PanMap layer format. *ETOPO1 Global Relief Model converted to PanMap layer format.*, *24*, 19.

Aurell, E., Boffetta, G., Crisanti, A., Paladin, G., & Vulpiani, A. (1996). Predictability in systems with many characteristic times: The case of turbulence. *Physical Review E*, *53*(3), 2337.

Bressan, A. C. (2019). The Deflection Angle of Surface Ocean Currents From the Wind Direction. *Journal of Geophysical Research: Oceans*, *124*(11), 7412–7420. doi: https://doi.org/10.1029/2019JC015454.

Callies, U., Groll, N., Horstmann, J., Kapitza, H., Klein, H., Maßmann, S., & Schwichtenberg, F. (2017). Surface drifters in the German Bight: model validation considering windage and Stokes drift. *Ocean Science*, 13(5), 799-827.

Castellari, S., Griffa, A., Özgökmen, T. M., & Poulain, P. M. (2001). Prediction of particle trajectories in the adriatic sea using Lagrangian data assimilation. *Journal of Marine Systems*, *29*(1–4), 33–50. doi: 10.1016/S0924-7963(01)00008-2.

Chen, F., Zhang, C., Brett, M. T., & Nielsen, J. M. (2020). The importance of the wind-drag coefficient parameterization for hydrodynamic modeling of a large shallow lake. *Ecological Informatics*, *59*, 101106. doi: 10.1016/j.ecoinf.2020.101106.

Chen, G., Chapron, B., Ezraty, R., Vandemark, D., 2002. A global view of swell and wind sea climate in the ocean by satellite altimeter and scatterometer. *J. Atmos. Ocean. Technol*. 19 (11), 1849–1859.

Chenillat, F., Huck, T., Maes, C., Grima, N., & Blanke, B. (2021). Fate of floating plastic debris released along the coasts in a global ocean model. *Marine Pollution Bulletin*, *165*, 112116. doi: 10.1016/j.marpolbul.2021.112116.

Choi, J., Troy, C., Hawley, N., McCormick, M., & Wells, M. (2020). Lateral dispersion of dye and drifters in the center of a very large lake. *Limnology and Oceanography*, 65(2), 336-348.

Clark, B. L., Carneiro, A. P. B., Pearmain, E. J., Rouyer, M. M., Clay, T. A., Cowger, W., Phillips, R. A., Manica, A., Hazin, C., Eriksen, M., González-Solís, J., Adams, J., Albores-Barajas, Y. V., Alfaro-Shigueto, J., Alho, M. S., Araujo, D. T., Arcos, J. M., Arnould, J. P. Y., Barbosa, N. J. P., … Dias, M. P. (2023). Global assessment of marine plastic exposure risk for oceanic birds. *Nature Communications*, *14*(1), 3665. doi: 10.1038/s41467-023-38900-z.

Cole, M., Lindeque, P., Halsband, C., & Galloway, T. S. (2011). Microplastics as contaminants in the marine environment: A review. *Marine Pollution Bulletin*, *62*(12), 2588–2597. doi: 10.1016/j.marpolbul.2011.09.025.

Cózar, A., Echevarría, F., González-Gordillo, J. I., Irigoien, X., Úbeda, B., Hernández-León, S., Palma, Á. T., Navarro, S., García-de-Lomas, J., Ruiz, A., Fernández-de-Puelles, M. L., & Duarte, C. M. (2014). Plastic debris in the open ocean.

Proceedings of the National Academy of Sciences of the United States of America, *111*(28), 10239–10244. doi: 10.1073/pnas.1314705111.

Curcic, M., Chen, S. S., & Özgökmen, T. M. (2016). Hurricane-induced ocean waves and stokes drift and their impacts on surface transport and dispersion in the Gulf of Mexico. *Geophysical Research Letters*, *43*(6), 2773-2781.

Cushman-Roisin, B., & Beckers, J. M. (2011). *Introduction to geophysical fluid dynamics: physical and numerical aspects* (Vol. 101). Academic press.

D'Asaro, E. A., Shcherbina, A. Y., Klymak, J. M., Molemaker, J., Novelli, G., Guigand, C. M., ... & Özgökmen, T. M. (2018). Ocean convergence and the dispersion of flotsam. *Proceedings of the National Academy of Sciences*, 115(6), 1162-1167.

Davis, R. E. (1985). Drifter observations of coastal surface currents during CODE: The method and descriptive view. *Journal of Geophysical Research: Oceans*, *90*(C3), 4741-4755.

de Dominicis, M., Bruciaferri, D., Gerin, R., Pinardi, N., Poulain, P.-M., Garreau, P., Zodiatis, G., Perivoliotis, L., Fazioli, L., Sorgente, R., and Manganiello, C.: A multi-model assessment of the impact of currents, waves and wind in modelling surface drifters and oil spill, *Deep Sea Research Part II*, 133, 21–38, 2016.

Dobler, D., Maes, C., Martinez, E., Rahmania, R., Gautama, B. G., Farhan, A. R., & Dounias, E. (2022). On the Fate of Floating Marine Debris Carried to the Sea through the Main Rivers of Indonesia. *Journal of Marine Science and Engineering*, *10*(8), 1009. doi: 10.3390/jmse10081009.

Ebuchi, N. (1999). Growth of wind waves with fetch in the Sea of Japan under winter monsoon investigated using data from satellite altimeters and scatterometer. *Journal of Oceanography*, *55*(5), 575-584.

Gu, J., Zhang, Y., Tuo, P., Hu, Z., Chen, S., & Hu, J. (2024). Surface floating objects moving from the Pearl River Estuary to Hainan Island: An observational and model study. *Journal of Marine Systems*, *241*. doi: 10.1016/j.jmarsys.2023.103917.

Haller, G. (2001). Lagrangian structures and the rate of strain in a partition of two-dimensional turbulence. *Physics of Fluids*, *13*(11), 3365-3385.

Haller, G. (2015). Lagrangian coherent structures. *Annual Review of Fluid Mechanics*, 47(1), 137–162. https://doi.org/10.1146/annurev-fluid-010313-141322

Haller, G., and Yuan, G. (2000). Lagrangian coherent structures and mixing in two-dimensional turbulence. *Physica D: Nonlinear Phenomena*, 147(3-4), 352–370. https://doi.org/10.1016/S0167-2789(00)00142-1

Haza, A. C., Paldor, N., Özgökmen, T. M., Curcic, M., Chen, S. S., & Jacobs, G. (2019). Wind-Based Estimations of Ocean Surface Currents From Massive Clusters of Drifters in the Gulf of Mexico. *Journal of Geophysical Research: Oceans*, *124*(8), 5844–5869. doi: 10.1029/2018JC014813.

Hersbach, H., Bell, B., Berrisford, P., Hirahara, S., Horányi, A., Muñoz-Sabater, J., ... & Thépaut, J. N. (2020). The ERA5 global reanalysis. *Quarterly journal of the royal meteorological society*, *146*(730), 1999-2049.

Hsu, P. C., Centurioni, L., Shao, H. J., Zheng, Q., Lu, C. Y., Hsu, T. W., & Tseng, R. S. (2021). Surface current variations and oceanic fronts in the southern East China Sea: Drifter experiments, coastal radar applications, and satellite observations. *Journal of Geophysical Research: Oceans*, 126(10), e2021JC017373.

Huang, G., Zhan, H., He, Q., Wei, X., & Li, B. (2021). A Lagrangian study of the near-surface intrusion of Pacific water into the South China Sea. *Acta Oceanologica Sinica*, *40*(7), 15–30. doi: 10.1007/s13131-021-1766-6.

Ichiye, T. (1984). Some problems of circulation and hydrography of the Japan Sea and the Tsushima Current. In *Elsevier oceanography series* (Vol. 39, pp. 15-54). Elsevier.

Irfan, T., Isobe, A., & Matsuura, H. (2024). A particle tracking model approach to determine the dispersal of riverine plastic debris released into the Indian Ocean. *Marine Pollution Bulletin*, *199*, 115985. doi: 10.1016/j.marpolbul.2023.115985.

Isobe, A., Hinata, H., Kako, S. I., & Yoshioka, S. (2011). Formulation of leeway-drift velocities for sea-surface drifting-objects based on a wind-wave flume experiment. *Interdisciplinary studies on environmental chemistry-marine environmental modeling and analysis. Terrapub., Tokyo*, 239-249.

Isobe, A., Uchida, K., Tokai, T., & Iwasaki, S. (2015). East Asian seas: A hot spot of pelagic microplastics. *Marine Pollution Bulletin*, *101*(2), 618–623. doi: 10.1016/j.marpolbul.2015.10.042.

Iwasaki, S., Isobe, A., Kako, S., Uchida, K., & Tokai, T. (2017). Fate of microplastics and mesoplastics carried by surface currents and wind waves: A numerical model approach in the Sea of Japan. *Marine Pollution Bulletin*, *121*(1–2), 85–96. doi: 10.1016/j.marpolbul.2017.05.057.

Jalón-Rojas, I., Wang, X. H., & Fredj, E. (2019). A 3D numerical model to Track Marine Plastic Debris (TrackMPD): Sensitivity of microplastic trajectories and fates to particle dynamical properties and physical processes. *Marine Pollution Bulletin*, *141*, 256–272. doi: 10.1016/j.marpolbul.2019.02.052.

Jeon, C., Park, J.-H., Varlamov, S. M., Yoon, J.-H., Kim, Y. H., Seo, S., Park, Y.-G., Min, H. S., Lee, J. H., & Kim, C.-H. (2014). Seasonal variation of semidiurnal internal tides in the East/Japan Sea. *Journal of Geophysical Research: Oceans*, *119*(5), 2843– 2859. doi: doi:10.1002/2014JC009864.

Kim, J. C., Yu, D. H., Sim, J. E., Son, Y. T., Bang, K. Y., & Shin, S. (2023). Validation of OpenDrift-Based Drifter Trajectory Prediction Technique for Maritime Search and Rescue. *Journal of Ocean Engineering and Technology*, *37*(4), 145–157. doi: 10.26748/KSOE.2023.018.

Kim, K., Kim, K. R., Min, D. H., Volkov, Y., Yoon, J. H., & Takematsu, M. (2001). Warming and structural changes in the East (Japan) Sea: a clue to future changes in global oceans?. *Geophysical Research Letters*, *28*(17), 3293-3296.

Kim, K., Tran, H. T. M., Song, K. M., Son, Y. B., Park, Y. G., Ryu, J. H., ... & Choi, J. M. (2024). Near-Surface Dispersion and Current Observations Using Dye, Drifters, and HF Radar in Coastal Waters. *Remote Sensing*, 16(11), 1985.

Kim, Y. R., Kang, D. W., Lee, S., Choi, K. Y., Kim, H. E., Jung, J. M., ... & Kim, C. J. (2021). Distribution and assessment of heavy metal concentrations in the East Sea-Byeong ocean dumping site, Korea. *Marine Pollution Bulletin*, *172*, 112815.

Kuroda, M., Isobe, A., Uchida, K., Tokai, T., Kitakado, T., Yoshitake, M., Miyamoto, Y., Mukai, T., Imai, K., Shimizu, K., Yagi, M., Mituhasi, T., & Habano, A. (2024). Abundance and potential sources of floating polystyrene foam macro- and microplastics around Japan. *Science of the Total Environment*, *925*(November 2023), 171421. doi: 10.1016/j.scitotenv.2024.171421.

LaCasce, J. (2008). Statistics from Lagrangian observations. *Progress in Oceanography*, *77*(1), 1-29, doi:10.1016/j.pocean.2008.02.002.

Lebreton, L. (2022). The status and fate of oceanic garbage patches. *Nature Reviews Earth & Environment*, *3*(11), 730–732. doi: https://doi.org/10.1038/s43017-022-00363-z.

Lebreton, L. C. M., Greer, S. D., & Borrero, J. C. (2012). Numerical modelling of floating debris in the world's oceans. *Marine Pollution Bulletin*, *64*(3), 653–661. doi: 10.1016/j.marpolbul.2011.10.027.

Lee, Dong Kyu, & Niiler, P. (2010). Eddies in the southwestern East/Japan Sea. *Deep-Sea Research Part I: Oceanographic Research Papers*, *57*(10), 1233–1242. doi: 10.1016/j.dsr.2010.06.002.

Liang, J. H., Liu, J., Benfield, M., Justic, D., Holstein, D., Liu, B., Hetland, R., Kobashi, D., Dong, C., & Dong, W. (2021). Including the effects of subsurface currents on buoyant particles in Lagrangian particle tracking models: Model development and its application to the study of riverborne plastics over the Louisiana/Texas shelf. *Ocean Modelling*, *167*(August), 101879. doi: 10.1016/j.ocemod.2021.101879.

Liu, Y., Weisberg, R. H., Vignudelli, S., & Mitchum, G. T. (2014). Evaluation of altimetry-derived surface current products using Lagrangian drifter trajectories in the eastern Gulf of Mexico. *Journal of Geophysical Research: Oceans*, *119*(5), 2827–2842. doi: 10.1002/2013JC009710.

Liu, Yonggang, & Weisberg, R. H. (2011). Evaluation of trajectory modeling in different dynamic regions using normalized cumulative Lagrangian separation. *Journal of Geophysical Research: Oceans*, *116*(C9). doi: 10.1029/2010JC006837.

Liubartseva, S., Coppini, G., Lecci, R., & Clementi, E. (2018). Tracking plastics in the Mediterranean: 2D Lagrangian model. *Marine Pollution Bulletin*, *129*(1), 151–162. doi: 10.1016/j.marpolbul.2018.02.019.

Lumpkin, R., Özgökmen, T., & Centurioni, L. (2017). Advances in the application of surface drifters. *Annual review of marine science*, 9, 59-81.

Mao, Y., & Heron, M. L. (2008). The influence of fetch on the response of surface currents to wind studies by HF ocean surface radar. *Journal of Physical Oceanography*, *38*(5), 1107–1121. doi: 10.1175/2007JPO3709.1.

Mariano, A. J., Kourafalou, V. H., Srinivasan, A., Kang, H., Halliwell, G. R., Ryan, E. H., & Roffer, M. (2011). On the modeling of the 2010 Gulf of Mexico Oil Spill. *Dynamics of Atmospheres and Oceans*, *52*(1–2), 322–340. doi: 10.1016/j.dynatmoce.2011.06.001.

Maximenko, N., Hafner, J., & Niiler, P. (2012). Pathways of marine debris derived from trajectories of Lagrangian drifters. *Marine Pollution Bulletin*, *65*(1–3), 51–62. doi: 10.1016/j.marpolbul.2011.04.016.

McCaffrey, L., & Koeberle, A. L. (2024). An economical open-source Lagrangian drifter design to measure deep currents in lakes. Water Resources Research, 60(10), e2024WR037429.

McWilliams, J. C. (2016). Submesoscale currents in the ocean. *Proceedings of the Royal Society A: Mathematical, Physical and Engineering Sciences*, *472*(2189), 20160117. doi: 10.1098/rspa.2016.0117.

Medina-Rubio, J., Nussbaum, M., van den Bremer, T. S., & van Sebille, E. (2026). Using surface drifters to characterise near-surface ocean dynamics in the southern North Sea: a data-driven approach. *Ocean Science*, 22(1), 49-74.

Nakakuni, M., Nishida, M., Nishibata, R., Kishimoto, K., Yamaguchi, H., Ichimi, K., Ishizuka, M., Suenaga, Y., & Tada, K. (2024). Convergence zones of coastal waters as hotspots for floating microplastic accumulation. *Marine Pollution Bulletin*, *206*(June), 116691. doi: 10.1016/j.marpolbul.2024.116691.

Niiler, P. P., & Paduan, J. D. (1996). Wind-driven motions in the northeast Pacific as measured by Lagrangian drifters. *Oceanographic Literature Review*, *7*(43), 646.

Novelli, G., Guigand, C. M., Cousin, C., Ryan, E. H., Laxague, N. J., Dai, H., ... & Özgökmen, T. M. (2017). A biodegradable surface drifter for ocean sampling on a massive scale. *Journal of Atmospheric and Oceanic Technology*, *34*(11), 2509-2532.

Okubo, A. (1971, August). Oceanic diffusion diagrams. In *Deep sea research and oceanographic abstracts* (Vol. 18, No. 8, pp. 789-802). Elsevier. https://doi.org/10.1016/0011-7471(71)90046-5.

Onink, V., Kaandorp, M. L., van Sebille, E., & Laufkötter, C. (2022). Influence of particle size and fragmentation on large-scale microplastic transport in the Mediterranean Sea. *Environmental science & technology*, *56*(22), 15528-15540. https://doi.org/10.1021/acs.est.2c03363

Onink, V., Wichmann, D., Delandmeter, P., & van Sebille, E. (2019). The Role of Ekman Currents, Geostrophy, and Stokes Drift in the Accumulation of Floating Microplastic. *Journal of Geophysical Research: Oceans*, *124*(3), 1474–1490. doi: 10.1029/2018JC014547.

Ono, J., Ohshima, K. I., Uchimoto, K., Ebuchi, N., Mitsudera, H., & Yamaguchi, H. (2013). Particle-tracking simulation for the drift/diffusion of spilled oils in the Sea of Okhotsk with a three-dimensional, high-resolution model. *Journal of Oceanography*, *69*(4), 413–428. doi: 10.1007/s10872-013-0182-8.

Park, K. A., Chung, J. Y., Kim, K., & Cornillon, P. C. (2005). Wind and bathymetric forcing of the annual sea surface temperature signal in the East (Japan) Sea. *Geophysical Research Letters*, *32*(5).

Park, Y.-G., & Seo, S. (2021). Review on Lagrangian Particle Tracking Modeling for Floating Objects around the Korean Peninsula. *KMI International Journal of Maritime Affairs and Fisheries*, *13*(2), 67–83. doi: 10.54007/ijmaf.2021.13.2.67.

Pärn, O., Davulienė, L., Moy, D. M., Vahter, K., Stips, A., & Torsvik, T. (2023). Effects of Eulerian current, Stokes drift and wind while simulating surface drifter trajectories in the Baltic Sea. *Oceanologia*, *65*(3), 453-465.

Paul, S., Nath, S., Bhattacharjee, S., & Mukherjee, S. (2024). Unveiling the effects of microplastics pollution on marine fauna. *Blue Biotechnology 2024 1:1*, *1*(1), 6. doi: 10.1186/s44315-024-00006-6.

Pinheiro, H. T., MacDonald, C., Santos, R. G., Ali, R., Bobat, A., Cresswell, B. J., Francini-Filho, R., Freitas, R., Galbraith, G. F., Musembi, P., Phelps, T. A., Quimbayo, J. P., Quiros, T. E. A. L., Shepherd, B., Stefanoudis, P. V., Talma, S., Teixeira, J. B., Woodall, L. C., & Rocha, L. A. (2023). Plastic pollution on the world's coral reefs. *Nature*, *619*(7969), 311–316. doi: 10.1038/s41586-023-06113-5.

Poje, A. C., Özgökmen, T. M., Lipphardt Jr, B. L., Haus, B. K., Ryan, E. H., Haza, A. C., ... & Mariano, A. J. (2014). Submesoscale dispersion in the vicinity of the Deepwater Horizon spill. Proceedings of the National Academy of Sciences, 111(35), 12693-12698.

Poulain, P. M., & Gerin, R. (2019). Assessment of the water-following capabilities of CODE drifters based on direct relative flow measurements. *Journal of Atmospheric and Oceanic Technology*, *36*(4), 621-633.

Poulain, P. M., Centurioni, L., & Özgökmen, T. (2022). Comparing the currents measured by CARTHE, CODE and SVP drifters as a function of wind and wave conditions in the southwestern Mediterranean Sea. *Sensors*, *22*(1), 353.

Prants, S. V., Budyansky, M. V., Ponomarev, V. I., & Uleysky, M. Y. (2011). Lagrangian study of transport and mixing in a mesoscale eddy street. *Ocean Modelling*, *38*(1–2), 114–125. doi: 10.1016/j.ocemod.2011.02.008.

Röhrs, J., Christensen, K. H., Hole, L. R., Broström, G., Drivdal, M., & Sundby, S. (2012). Observation-based evaluation of surface wave effects on currents and trajectory forecasts. *Ocean Dynamics*, *62*(10), 1519-1533.

Röhrs, J., Sutherland, G., Jeans, G., Bedington, M., Sperrevik, A. K., Dagestad, K. F., ... & LaCasce, J. H. (2023). Surface currents in operational oceanography: Key applications, mechanisms, and methods. Journal of Operational Oceanography, 16(1), 60-88.

Rypina, Irina I., Getscher, T. R., Pratt, L. J., & Mourre, B. (2021). Observing and Quantifying Ocean Flow Properties Using Drifters with Drogues at Different Depths. *Journal of Physical Oceanography*, *51*(8), 2463–2482. doi: 10.1175/JPO-D-20-0291.1.

Saeedi, M. (2024). How microplastics interact with food chain: a short overview of fate and impacts. *Journal of Food Science and Technology*, *61*(3), 403–413. doi: 10.1007/s13197-023-05720-4.

Santos de Moura, M. & Vianna, M. (2020). A new threat: assessing the main interactions between marine fish and plastic debris from a scientometric perspective. *Reviews in Fish Biology and Fisheries*, *30*(4), 623–636.

Sebille, E. van, Aliani, S., Law, K. L., Maximenko, N., Alsina, J. M., Bagaev, A., Bergmann, M., Chapron, B., Chubarenko, Cózar, I., Andrés, Delandmeter, P., Egger, M., Fox-Kemper, B., Garaba, S. P., Oddijn-Murphy, L., Hardesty, B. D., Matthew

J Hoffman17, A. I., Cleo E Jongedijk19, Mikael L A Kaandorp1 , Liliya Khatmullina6, A. A. K., … Giuseppe Suaria2 , Martin Thiel34, 35, 36, T. S. van den B. and D. W. (2020). The physical oceanography of the transport of floating marine debris. *Environmental Research Letters*, *15*(2), 023003. Retrieved from http://dx.doi.org/10.1088/1748-9326/ab6d7d.

Seo, S., Park, Y. G., & Kim, K. (2020). Tracking flood debris using satellite-derived ocean color and particle-tracking modeling. *Marine Pollution Bulletin*, *161*(PA), 111828. doi: 10.1016/j.marpolbul.2020.111828.

Shadden, S. C., Lekien, F., and Marsden, J. E. (2005). Definition and properties of Lagrangian coherent structures from finite-time Lyapunov exponents in two-dimensional aperiodic flows. *Physica D: Nonlinear Phenomena*, 212, 271–304. https://doi.org/10.1016/j.physd.2005.10.007

Sotillo, M. G., Garcia-Ladona, E., Orfila, A., Rodríguez-Rubio, P., Maraver, J. C., Conti, D., ... & Álvarez-Fanjul, E. (2016). The MEDESS-GIB database: tracking the Atlantic water inflow. *Earth System Science Data*, 8(1), 141-149.

Sotillo, M. G., Garcia-Ladona, E., Orfila, A., Rodríguez-Rubio, P., Maraver, J. C., Conti, D., ... & Álvarez-Fanjul, E. (2016). The MEDESS-GIB database: tracking the Atlantic water inflow. *Earth System Science Data*, *8*(1), 141-149.

Sudre, J., Maes, C., & Garçon, V. (2013). On the global estimates of geostrophic and Ekman surface currents. *Limnology and Oceanography: Fluids and Environments*, *3*(1), 1–20. doi: 10.1215/21573689-2071927.

Sun, Z., Hu, J., Lin, H., Chen, Z., Zhu, J., Yang, L., ... & Wu, X. (2022). Lagrangian observation of the Kuroshio current by surface drifters in 2019. *Journal of Marine Science and Engineering*, 10(8), 1027.

Takeda, H., & Isobe, A. (2024). Quantification of ocean microplastic fragmentation processes in the Sea of Japan using a combination of field observations and numerical particle tracking model experiments. *Marine Pollution Bulletin*, *208*, 117032.

Talley, L.D., D.-H. Min, V.B. Lobanov, V.A. Luchin, V.I. Ponomarev, A.N. Salyuk, A.Y Shcherbina, P.Y. Tishchenko, and I. Zhabin. 2006. Japan/East Sea water masses and their relation to the sea's circulation. *Oceanography* 19(3):32–49, https://doi.org/10.5670/oceanog.2006.42.

Tamtare, T., Dumont, D., & Chavanne, C. (2022). The Stokes drift in ocean surface drift prediction. *Journal of Operational Oceanography*, *15*(3), 156–168. doi: 10.1080/1755876X.2021.1872229.

Tekman, M. B., Walther, B. A., Peter, C., Gutow, L., & Bergmann, M. (2022). Impacts of Plastic Pollution in the Oceans on Marine Species, Biodiversity and Ecosystems Summary of a Study for Wwf By Summary of a Study for Wwf By Wwf International 2022 3 Summary. *Alfred-Wegener-Institut*. doi: 10.5281/zenodo.5898684.

Thiel, M., Luna-Jorquera, G., Álvarez-Varas, R., Gallardo, C., Hinojosa, I. A., Luna, N., Miranda-Urbina, D., Morales, N., Ory, N., Pacheco, A. S., Portflitt-Toro, M., & Zavalaga, C. (2018). Impacts of marine plastic pollution from continental coasts to subtropical gyres-fish, seabirds, and other vertebrates in the SE Pacific. *Frontiers in Marine Science*, *5*(July), 238. doi: 10.3389/fmars.2018.00238.

van der Mheen, M., Pattiaratchi, C., Cosoli, S., & Wandres, M. (2020). Depth-Dependent Correction for Wind-Driven Drift Current in Particle Tracking Applications, *Frontiers in Marine Science, 7, 305*.

Woo, H. J., & Park, K. A. (2017). Long-term trend of satellite-observed significant wave height and impact on ecosystem in the East/Japan Sea. *Deep Sea Research Part II: Topical Studies in Oceanography*, 143, 1-14.

Wu, J. (1982). Wind-stress coefficients over sea surface from breeze to hurricane. *Journal of Geophysical Research: Oceans*, *87*(C12), 9704–9706. doi: 10.1029/jc087ic12p09704.

Yoon, J. H., Kawano, S., & Igawa, S. (2010). Modeling of marine litter drift and beaching in the Japan Sea. *Marine pollution bulletin*, 60(3), 448-463.